Faint Galaxies in the Megaparsec-Scale Environments of Hyperluminous QSOs at Redshifts $2 < z < 3$

Thesis by

Ryan F. Trainor

In Partial Fulfillment of the Requirements
for the Degree of
Doctor of Philosophy

California Institute of Technology
Pasadena, California

2015
(Defended 15 August 2014)

To Elle —
Thank you for your encouragement and support;
I could not have done this without you. To
paraphrase the words of a friend of ours:
All the other girls here are stars,
You are [HS1549+1919]!

Acknowledgments

It is hard work, writing a thesis. If it were merely the innumerable taps of fingers upon the keyboard that have taxed my fingers these last few weeks, it could possibly be borne, though I suspect even then that most people would choose to avoid it and be considered wise for so choosing. Of course, however, it takes all the more doing than that, for beforehand Research must be Undertaken, data collected and plots pondered and heads scratched and inspirations received from above and all the rest of it. And meanwhile, the Student must be prodded, and fed, and housed, and entertained; he must be provided funding and a chair and a desk and be told how to access his email; she must find recreation facilities and the occassional softball on which to unleash the pent-up frustration of a thousand segmentation faults and misplaced factors of 2. And even with all of that, there can be no thesis without the previous rounds of prodding, feeding, and housing that bundle our prospective Scholar through high school and college! The telescopes that must be assembled to greet her arrival; the mountains of scientific thought on which he might build an additional mole-hill! The tax dollars! The after-school programs! Good Heavens, the diapers!

Surely, the production of even the least thesis is well beyond the strength of even the best woman or man, just as this one has been well beyond mine. Thankfully, this process has been supported and sustained by an incredible community of people. Whatever little or much the lasting worth of this thesis may be, it could not exist without them. Here are my thanks.

Leaving aside (with apologies) the past generations of humanity whose ceaseless strivings made possible the comforts and tools of the modern astronomer, the first actors in the story of this thesis are my parents. Mom and Dad, you taught me the most important lessons I know: to approach hard tasks and conversations head-on, to trust that difficult times breed wisdom and patience, and to seek to see the best, the *imago dei*, in all people (including myself) even when we are at our worst. Thank you. I could also mention how you taught me to love learning, teaching, creative expression, the wonders of nature, and many other essential aspects of life besides, but there is neither time nor space here – it would take many, many theses to do them justice, and I hope to only ever write this one. Hillary, my sister: as a child you taught me grace and patience in equal measure, my first lessons in collaboration, and you continue to inspire me to live with more discipline, more thought, more style, and more love. Thank you for these gifts.

After my immediate family, perhaps no body was more formative to me than the public school system of El Dorado County, California. Public school teachers are unaccountably maligned in times of budget shortfalls and international standardized test comparisons, but mine (and I suspect, most) have been among the noblest and best people in all of humanity. Through these great Educators, I have learned to see the richness of the world around me: books, worms, art, soccer balls, and (certainly) stars. Similarly, they taught me that knowledge is not pursued to be kept in an ivory tower but to be shared and examined by eyes large and small, that only in teaching a rule or a subject do we fully understand it, and that the flash of understanding in a pupil's eyes provides a far more addictive high than most Schedule I controlled substances. Particular thanks go to April Hood of Gold Oak Elementary for fostering my love of math, and equal thanks go to Susan Prior of Union Mine High School for encouraging me not to major in it. Mrs. Prior likewise provided my first opportunity to teach a high school class, an experience that cemented my desire to educate.

I was not truly on the road to academia, however, until Roger McWilliams dragged me to his lab in my second term at UC Irvine. Roger taught me the difference between physics from a book and physics with a homemade Langmuir probe, a vacuum pump, and a highly-magnetized Argon plasma. It was exhilirating, and it made Real Science approachable. I thank Roger for teaching me that theorists don't have a monopoly on fun and that bow ties are a timeless and elegant accessory for any occassion. Andrea Ghez advised me during my summer at UCLA and set me down the path of observational astronomy. Her enthusiasm was palpable, her encouragement was unceasing, and she was the first person to tell me that I might have a future in research. She also set off my love affair with supermassive black holes, a phrase that makes me dizzy even after years of more galaxy-focused work. I would not be completing this degree if not for Roger and Andrea.

Of course, the majority of my own work on this thesis has come in the 6 years I have spent at Caltech. Tim Morton and Vera Gluscevic welcomed me to Pasadena and became my first friends here. I am grateful for their warm hospitality, their constant invitations to concerts and athletic activities, and our conversations that ranged from burritos to metaphysics. Upon beginning coursework, I quickly became acquainted with three exceptional classmates: Swarnima Manohar, Shriharsh Tendulkar, and Dmitriy Tseliakhovich. Dmitriy is the most enterprising individual I've ever met – if I ever get to space, it will almost certainly be through knowing him. Thank you in advance, Dmitriy. Shriharsh is one of the most positive gentlemen I've ever met, and we shared many laughs from such storied sources as John Cleese, Bill Watterson, and P. G. Wodehouse. Furthermore, his astrophysical puns are truly, *ahem*, stellar. Swarnima has been my officemate for 5 of the last 6 years and my co-chair of Astronomy Outreach for nearly as long. We ran some pretty great events together, and she is responsible for almost everything I know about radio astronomy and subcontinental cooking. She, Shriharsh, and Kunal Mooley (the most excellent Bollywood dance instructor I have ever encountered) made me feel as Indian as I think any descendent of Irish-Italian immigrants has ever been privileged to feel.

I have also had some wonderful roommates here in Pasadena, and to them I owe a great debt as well. Ben Camp and I spent the last year of his bachelorhood living together, and he and his family gave me frequent solace during the stresses of my first year of graduate school. This solace usually took the form of PBR, bowling, and/or breakfast for dinner, a soul-filling trifecta guaranteed to purge the memory of even the most devilish problem set. Sam Lee and I decided to live together after that first year, and we shared many adventures over the next two years, primarily of the culinary and musical varieties. Sam's knack for obtaining unobtainable tickets would have been enough to earn my eternal gratitude, but he is also somehow one of the kindest and smartest people I know. I have missed him often since he left for the "other" coast. Matt Schenker made the bold decision to join our apartment after only a single prospective visit. A profoundly proficient athlete (from tennis to skiing to mountaineering), Matt somehow still enjoys sharing these pursuits with those less physically blessed; I admire both his spirit of adventure and his patience. Thinh Bui was assigned to our apartment by lottery, but he and I lived together for almost 5 years. Thinh works as hard as anyone I know, but he was also always willing to stop for a shared meal or to provide a ride to the airport. He teaches me not to take anything for granted, to work hard, and to keep my friends and family close. Andrew Fuenmayor and I were no longer roommates by the time I came to Caltech, but conversations with him kept me grounded throughout my studies.

Many others at Caltech gave me more help than they are likely to know. Brian Brophy and the Theater Arts at Caltech (TACIT) kept me sane when I needed to indulge in some thoroughly non-astronomical pursuits. Brian and the other leaders of that group have created something truly magical: a world where novices and old hats can together make art that is lively, breathtaking, hilarious, and never "safe." If I can find a group half so bold at each stage of my academic journey, I will be blessed indeed. In our own department, Anu Mahabal and Patrick Shopbell are true Wizards, capable (and willing) to fix all manner of technological issues from across oceans and at any time of day or night. If this is not enough evidence of their wizarding prowess, they also throw the meanest Cinco de Mayo party this side of Puebla, MX, and Patrick's homebrew is responsible for $\gtrsim$90% of the hair on my chest. Gita Patel, Gina Armas, Althea Keith, and Judy McClain are the friendliest and most competent group of administrators yet to be assembled. Without their help and advice, my time at Caltech would have been a nightmare of bureaucracy. Lynne Hillenbrand eased my transition to Pasadena with good seats at Chavez Ravine and better advice. Chris Hirata had an open door and the solution to any question I presented, always offered with a smile and many encouraging nods. He will be missed at Caltech.

Wal Sargent is missed as well. I did not know him as well or for as long as many did here, but his shrewd science, dry wit, and great stories have left a powerful legacy behind him. I do not know why he bothered to engage with a 22-year-old Liverpool fan who had never been to England, but I enjoyed our friendly rivalry, and his jibes and jests were no less incisive for being made in good fun.

Of all the students at Caltech who helped me along the way, none were so supportive as Gwen Rudie. Qualifying exams, candidacy, publishing papers, conferences, job applications, and talks: she crossed each threshold ahead of me and reached out her hand to help pull me across behind her. I don't know how, or if, I would have finished this degree without her perspective and encouragement. She and her husband Andrew Newman are as kind and generous as they are phenomenal scientists, and it has been a joy to share grad school, conferences, observing runs, and even wedding months with them – I look forward to many years of our continued collaboration and fellowship. I have not been half the mentor to Allison Strom that Gwen has been to me, but she clearly has the wit and skill to succeed without my help. We shared some excellent times on multiple continents, and I admire her maturity, her attention to detail, and her sublime cocktails. I was a similarly poor mentor, I fear, to Trevor David and Michael Eastwood,[1] but they are such easy-going fellows that I'm sure they will forgive me. I've enjoyed my time spent with them both as colleagues and as friends.

All of this brings me to Chuck. I came to Caltech to work with Charles C. Steidel in large part because of his scientific reputation and the success of his students. I was amazed to find a most approachable and humble Giant. I will not waste words praising his scientific prowess and superhuman intuition; the MacArthur and Gruber Foundations have already provided ample documentation of these truths, and Chuck would hate to read it in any case. What I learned from Chuck is that good science speaks for itself and that projects worth doing are worth doing well. I greatly appreciate both the freedom he offered me and the guiding questions that kept me on track. Being a part of the MOSFIRE project, in particular, was a phenomenal experience. In the midst of his extraordinary scientific success and productivity, I especially respect his commitment to spend the vast majority of his evenings and weekends at home with his family. Being newly married myself, I think this balance might be the most important lesson he can teach me.

We are almost done now; there are two people left for me to thank and then these Acknowledgements (which, it seems to me, read more like a self-indulgent memoir) will be concluded. William Myron Keck, the great wildcatter and oil entrepreneur, built Superior Oil Company into the USA's largest independent oil producer. In so doing, he indirectly provided me with two great gifts: funding for the W. M. Keck Observatory in Mauna Kea, and a job for an immigrant Dutchman who would eventually become the grandfather of my wife. Even as I seek to limit my own fossil fuel dependence, I must acknowledge that I owe this man a great debt on both counts – much of my current happiness does indeed depend on his fossil fuels.

That happiness, most of all, is Elle. She came into my life at the end of a dark time and ever since has illuminated it by her presence. Already, she has given me strength and support through all manner of trials, and I owe most of my motivation and success to her relentless love and encouragement. I'm so glad to have a lifetime to pay her back.

---

[1] Michael also brought me a refreshing drink on the hot day when I was writing this section, but I'm sure I would have thanked him anyway.

Abstract

This thesis presents detailed observational studies of the extended distributions of gas, galaxies, and dark matter around hyperluminous quasars (HLQSOs) at high redshift. Taken together, these works aim to coherently describe the relationships between these massive, accreting black holes and their environments: the nature of the regions that give rise to such massive black holes, the effect of HLQSO radiation on their surrounding galaxies and gas, and the ability of both galaxies and black holes to shed new light on the formation and evolution of the other.

Chapter 2 focuses on the continuum-color-selected galaxies drawn from the Keck Baryonic Structure Survey (KBSS, Rudie et al. 2012). The KBSS is a uniquely deep spectroscopic survey of star-forming galaxies in the same volumes of space as 15 HLQSOs at $2.5 < z < 2.9$. The three-dimensional distribution of these galaxies among themselves and the nearby HLQSOs is used to infer the extent to which these black holes are associated with overdense peaks in the dark matter and galaxy distribution as quantified by clustering statistics. In conjunction with recent dark-matter simulations, these data provide the first estimates of the host dark-matter halo masses for HLQSOs, providing new insight into the formation and evolution of the most massive black holes at high redshift.

Chapter 3 describes the first results from a new survey (KBSS-Lyα) conducted for this thesis. The KBSS-Lyα survey uses narrowband imaging to identify Lyα-emitters (LAEs) in the $\sim$Mpc regions around eight of the KBSS HLQSOs. Many of these LAEs show the effect of reprocessed HLQSO radiation in their emission through the process known as Lyα fluorescence. In Chapter 3, these fluorescent LAEs are used to generate a coarse map of the average HLQSO ionizing emission on Mpc scales, thereby setting the first direct constraints of the lifetime and angular distribution of activity for a population of these uniquely luminous black holes.

Chapter 4 contains a more detailed description of the KBSS-Lyα survey itself and the detailed properties of the star-forming and fluorescent objects selected therein. Using imaging and spectroscopic data covering rest-frame UV and optical wavelengths, including spectra from the new near-infrared spectrometer MOSFIRE, we characterize this population of nascent galaxies in terms of their kinematics, enrichment, gas properties, and luminosity distribution while comparing and constrasting them with previously-studied populations of continuum-selected galaxies and LAEs far from the effects of HLQSO emission.

At the conclusion of this thesis, I briefly present future directions for the continuation of this research. In Appendix A, I provide background information on the instrumentation used in this thesis, including my own contributions to MOSFIRE.

Contents

List of Figures

List of Tables

Chapter 1

Introduction

Let us begin, as always, with the universe.

Soon[1] after the Big Bang, the universe was filled with two primary components: dark matter and gas. Gravity caused dark matter to form over-dense clumps, creating the first structures and directing gas to flow into these regions. The gas in these proto-galaxies eventually became dense enough to form the first stars, and the deaths of these stars likely created the first black holes. At this point, however, galaxy formation became much more complicated as the emergence of the first stars and black holes severely disrupted the smooth flow of gas into the nascent galaxies.

This complexity arises because the processes of turning gas into stars and accreting gas into black holes release colossal amounts of energy. Once this phase of galaxy growth begins, the inflowing gas is subjected to blasts of ionizing radiation and outflowing winds that expel gas from galaxies and can violently terminate the growth of black holes and formation of new stars. The remainder of the evolution of these galaxies remains a puzzle, but it must be determined by a complex interplay between dark matter, stars, black holes, and gas that eventually yields the array of galaxies seen in the modern-day universe.

This thesis addresses the primary participants in this interplay. The work described here uses measurements of different types of galaxies around some of the most rapidly-accreting black holes in the universe to determine the types of environments where black holes grow most effectively and the effect of these black holes on their local neighborhood. Using these bright black holes (called QSOs) as subjects of study, tracers of galaxy density, and illuminators of their surrounding galaxies and gas, this thesis provides a new and unique step forward in solving the puzzle of galaxy formation and growth.

1.1 Galaxy Formation and "Feedback"

A simple picture of galaxy formation was presented above in which gas flows into dense, bound clumps of dark matter ("dark matter halos"), eventually condensing via gravity into stars. In fact, however, most of the gas never ends up in stars at all. Galaxies are remarkably inefficient machines for converting gas into stars:

---

[1] "Soon" is a notoriously subjective term, here refering to a period of roughly 370 million years.

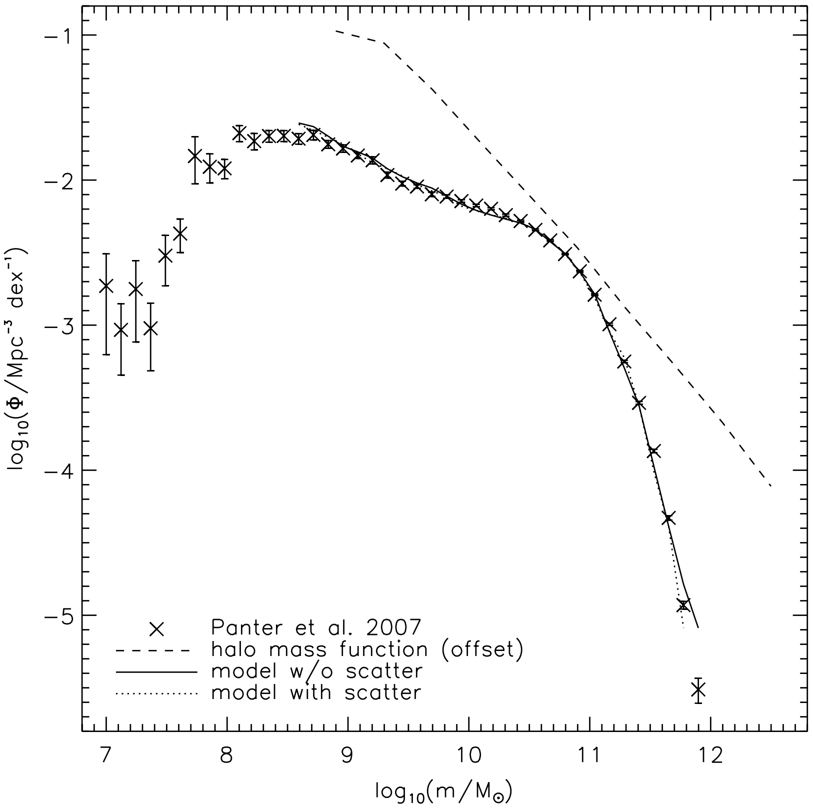

Figure 1.1: The stellar and dark-matter mass functions of galaxies. Black points are measurements of the stellar mass function from the Sloan Digital Sky Survey (SDSS) by Panter et al. (2007). The black dashed line is the mass function of dark matter halos produced by an N-body (gravity-only) dark matter simulation using the concordance ΛCDM cosmology; the curve has been scaled down by a multiplicative factor of 0.05. If all gas in galaxies was converted into stars, the two curves would be parallel, with an offset given by the universal baryon-to-dark-matter fraction (∼0.2). Instead, star formation is highly suppressed, particularly at low and high masses. Figure from Moster et al. (2010).

despite the fact that the dark matter mass, gas mass, and stellar mass of galaxies are seen to grow over cosmic time, only a small fraction of the gas coming in feeds new star-formation, regardless of galaxy age, type, or mass (e.g. Schmidt 1959; Kennicutt 1998).

This ineffiency may be parameterized as the fraction of baryonic matter (i.e. non-dark matter) that has entered a galaxy halo that is now in the form of stars. When this inefficiency is studied as a function of galaxy mass, a clear trend emerges: despite the universally-low stellar mass fractions, star formation is most efficient in halos of $M_{\mathrm{halo}} \sim 10^{12}\mathrm{M}_\odot$ from $z \sim 8$ to the present day (Moster et al. 2010; Behroozi et al. 2013), falling off sharply at higher and lower dark matter halo masses (Fig. 1.1).

Both the global suppression of star formation and the dependence on mass suggest that galaxy growth is highly regulated by one or more mass-dependent processes. These regulatory processes are described as “feedback” effects, so-called because it seems that the effects that suppress star formation seem to be driven by the very growth of galaxies themselves.

What aspect of galaxy growth could counteract the powerful gravitational pull toward cooling, conden-

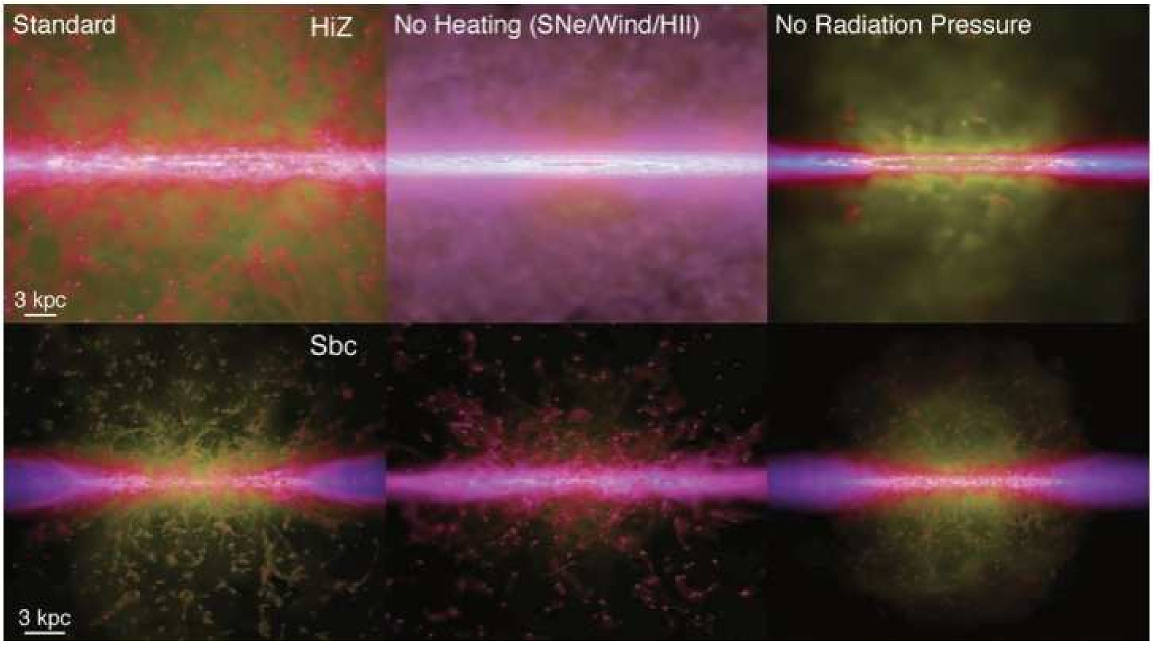

Figure 1.2: Hydrodynamical simulations of stellar feedback in galaxies by Hopkins et al.. Each row consists of edge-on simulated images of a different galaxy model, while each column displays the results of turning various stellar feedback modes on or off. The left column shows all feedback modes enabled, while the middle column shows thermal feedback via supernovae, stellar winds, and photoionization turned off. The right column shows heating turned on, but short- and long-range radiation pressure turned off. Color encodes gas temperature from $T \lesssim 1000$ K (blue) to $T \sim 10^4 - 10^5$ K (pink) to $T \gtrsim 10^6$ K (yellow). The stellar feedback modes counteract the effects of gravitational collapse by heating gas, driving material out of dense regions (creating dark bubbles in these images), and blowing hot gas out into the intergalactic medium in the form of galaxy winds. Figure from Hopkins et al. (2012), with some panels omitted for brevity.

sation, and ignition? The energy released by young stars is an obvious possibility. Young stellar populations include massive hot stars utterly unlike our peaceful Sun: in the course of their short lives, the most massive stars emit ionizing photons, stellar winds, and long-range radiation pressure, only to die in yet another blast of thermal and kinetic energy. Simulations such as Hopkins et al. (2012; see Fig. 1.2) suggest that stellar feedback involves all of these processes in degrees that may vary with stellar mass and other galaxy properties. Not only do these simulations quench and modulate star formation, but they can also produce the strong outflowing winds that are observed in nearly all samples of high-redshift galaxies. Because the scales of individual stars and star clusters driving this feedback are not resolved in galaxy simulations, however, much of the physics of these effects must be estimated and imported by hand; it remains a challenge to physically connect simulations of stellar feedback and star formation in an entirely self-consistent and physically-motivated manner.

Therefore, while simulations are making swift progress in this arena, there is still substantial mystery surrounding the interactions of galaxies with their interstellar gas, as well as the gas in the intergalactic medium (IGM) and circumgalactic medium (CGM; $r_{\rm gal} \sim 0.3 - 2$ Mpc). Of particular import is the fact that hydrodynamical galaxy simulations typically predict copious amounts of inflowing neutral Hydrogen (H I) gas along anistropic filaments (e.g. Kereš et al. 2005), a process that is argued to be necessary to produce the observed cosmic star formation and its evolution (van de Voort et al. 2011).

However, observational evidence for these "cold flows" is lacking: surveyed galaxy populations seem to be uniformly dominated by signatures of outflowing, metal-enriched gas, with little or no evidence for inflowing streams of pristine H I. Even the predictions for observables associated with cold flows remain unclear. Furthermore, there is still a gap between the hydrodynamical treatment of inflows and stellar feedback; it remains to be seen how observationally-consistent models of feedback will effect simulations of gas accretion.

On the observational side, progress must come from continued measurements of galaxies and their surrounding gas. The observable signatures of stellar feedback must be extended to a larger range of galaxy properties (including low stellar mass, continuum-faint populations) to see how these effects scale. Particular attention should be attended to populations where gas inflow might be expected to dominate over outflows, such as those where star-formation has only recently begun.

Finally, a complete understanding of galaxy feedback requires more than just the interactions of their stars and gas. At the high-mass end of the galaxy mass function (Fig. 1.1), even the most powerful stellar-feedback prescriptions seem unable to overcome the deep gravitational potential of the most massive halos. For these systems, another form of feedback has been proposed (e.g. Croton et al. 2006) that further modulates galaxy growth through the colossal power associated with accretion onto supermassive black holes (SMBHs). A description of these objects, the history of their study, and their role in galaxy formation follows below.

1.2 QSRS, QSOs, and SMBHs: A History

One hurdle to understanding the field of supermassive black hole research is the decades of nomenclature that have persisted even after the paradigms that defined them have fallen away.[2] The first detections of objects that would motivate the study of supermassive black holes occurred in the 1960's, when Allan Sandage, Maarten Schmidt, Thomas Matthews, and Jesse Greenstein (among others associated with Caltech and the nearby Mt. Wilson and Palomar Observatories) began identifying optical counterparts to radio sources of unknown origin and distance. The point-like optical sources exhibited spectra with unrecognized broad emission lines, which along with their radio emission led to the moniker "Quasi-Stellar Radio Sources" (QSRS or QSS).

In 1963, Maarten Schmidt famously[3] identified the Balmer series of Hydrogen and the Mg II λ2797 line redshifted by 16% in the spectrum of QSO 3C 273. Potential galactic sources of such redshifted emission (high radial velocity stars, strong gravitational redshift) were soon ruled out, and the existence of a population of compact, extragalactic, radio-loud sources was established. Shields (1999) suggests that the "radio"

---

[2] A fascinating review of the history of QSO science was written by Shields (1999). Much of the background given here is an all-too-brief summary of that paper.

[3] in astrophysical circles, at the very least, but see also the March 11, 1966 cover of TIME magazine.

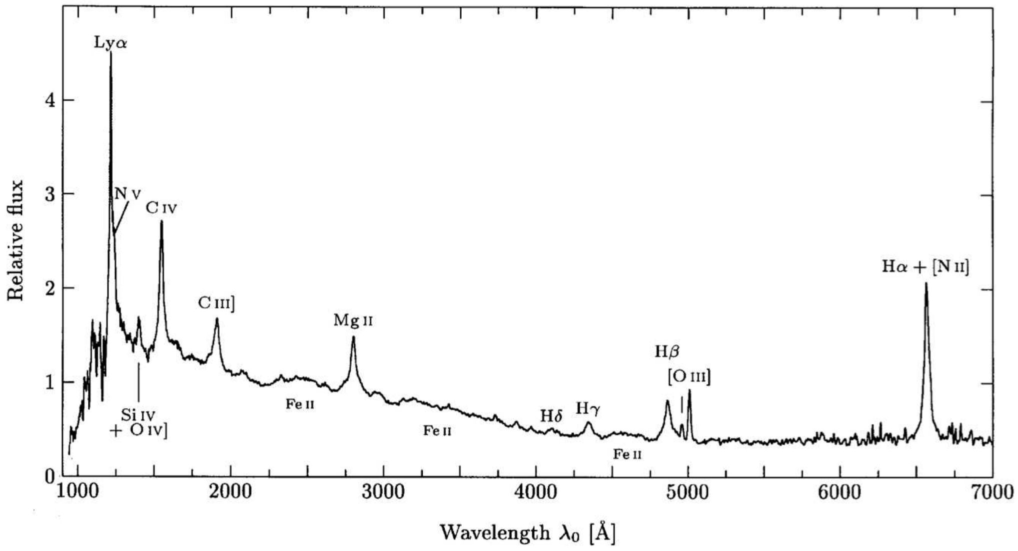

Figure 1.3: A composite spectrum of 65 QSOs and similar objects (Seyfert 1 galaxies). The spectrum is shifted to the rest frame to account for the redshift of the sources. The broad emission lines and strong UV ($\lambda \lesssim 3000$Å) continuum emission are typical of QSOs. Note in particular the strong, broad Balmer lines (Hα, Hβ, etc.) and Mg II λ2797 line seen in emission: these lines were used by Maarten Schmidt to measure the large redshift of QSO 3C 273. This first QSO redshift measurement quickly established the extragalactic origin and extreme luminosities of these "quasi-stellar" objects. Figure from Meusinger & Brunzendorf (2001).

requirement was dropped when Sandage (1965) reported a new population of extra-galactic objects without radio detections but which matched the optical properties (including strong UV continua) of QSRS; these objects were soon dubbed Quasi-Stellar Galaxies (QSGs) or Blue Stellar Objects (BSOs). By 1967 the related term Quasi-Stellar Objects (QSOs) was established enough to title a book by Geoffrey Burbidge,[4] though the name was used as early as 1964 on a leaflet from the Astronomy Society of the Pacific: *QSO's, the Brightest Things in the Universe*.[5] The title of this leaflet captures a primary feature of QSOs and their analogues: even with an over-estimated rate of Hubble expansion, the measured redshifts of these objects were quickly seen to imply huge distances and thus unprecedented absolute luminosities for compact sources.

The widespread association of QSOs and other Active Galactic Nuclei (AGN) with supermassive black holes (SMBHs) did not occur until decades later. Lynden-Bell (1969) suggested that "collapsed bodies" (i.e. black holes) at the centers of local galaxies could be the remnants of QSOs and could explain other AGN-associated phenomena. However, a broader focus on SMBHs as the engines of QSO emission awaited the development of accretion-disk theory and the determination that other compact sources of nuclear emission (star clusters, supermassive stars) would eventually form black holes as their eventual endpoint, as described

---

[4] *Quasi-stellar Objects*, Burbidge, A Series of Books in Astronomy and Astrophysics, San Francisco: W.H.Freeman, 1967

[5] This leaflet, available as a scanned digital document through the SAO/NASA Astrophysics Data System, contains a fascinating summary of a conference in December 1963 centered on the quickly-growing field of QSO research featuring the latest results from Sandage, Matthews, Schmidt, Greenstein, Margaret Burbidge, and others. The idea of massive energy being released through gravitational collapse to "within the Schwarzschild radius" is mentioned, though only in the context of a number of other "radical ideas" proposed at the conference.

in a review by Rees (1984). While the details and evolution of these powerful objects remains the focus of substantial research, SMBH accretion in the nuclei of galaxies has been the generally-accepted model for the broad range of AGN activity since that time.

Many features of QSOs identified before the SMBH paradigm remain equally relevant today. Schmidt (1965) presented the first detection of Lyα in a QSO spectrum, noting the irregular, double-peaked profile of the emission line. Matthews et al. (1964) identified overdensities of galaxies around luminous radio galaxies, another type of QSO analogue. While the study of QSOs has advanced significantly since that time, the association of scattered Lyα emission (McCarthy et al. 1987; Trainor & Steidel 2013) and galaxy overdensities (Venemans et al. 2007; Trainor & Steidel 2012) with bright AGN remain areas of active research and are a substantial part of this thesis.

1.3 QSO Environments and Galaxy Evolution

While black holes may be fascinationg objects in isolation, they have become even more compelling as it has become clear that they play a strong role in galaxy evolution as well. Observed correlations among properties of galaxies and the masses of their central black holes (e.g. Magorrian et al. 1998; Gebhardt et al. 2000; Ferrarese & Merritt 2000) suggest a strict relationship between the nuclear activity that accompanies black hole growth and the gas accretion and cooling that causes star formation. As mentioned in Sec. 1.1, models such as Croton et al. (2006) also demonstrate the potential for black hole accretion to explain the extremely low efficiency of star formation in the most massive halos. However, the mechanisms that govern these interactions remain unclear; loosely termed “AGN feedback”, they must somehow efficiently couple the energetics of AGN and star formation over orders of magnitude in spatial scale. Adding to this complex picture, SMBH-driven emission must be highly anisotropic in order to unify the vastly different categories of AGN selected at wavelengths from the radio to hard x-rays, and this anisotropy may diminish the solid angle over which AGN activity can effectively couple to galactic proto-stellar gas.

This unified model, in which AGN are obscured by dusty torii, suggests that inclination determines the observed properties of AGN to first order, but essential second-order modifications to this successful paradigm are now coming to light. The obscuration of AGN seems to be time-dependent and to correlate with galaxy properties, at least in the low-redshift universe; obscured AGN may tend to live in galaxies with extreme star-formation rates (e.g. Sanders et al. 1988), while optically-bright QSOs are more common in passive ellipticals (e.g. Dunlop et al. 2003). This correlation suggests a track in galaxy evolution whereby AGN may quench star formation as they disrupt their obscuring gas and dust (e.g. Hopkins et al. 2008), but such a model requires that AGN obscuration vary with the age of a black hole’s growth phase in addition to its inclination. Relationships persist to larger scales as well: Hickox et al. (2011) and Donoso et al. (2013) find that obscured QSOs are more biased than unobscured QSOs at $z \sim 1$, suggesting a dependence on halo mass, while radio-loud QSOs are known to inhabit overdense environments (Matthews et al. 1964; Best et al. 2005; Venemans et al. 2007). Clearly, the evolution of black holes and their ability to modulate galaxy growth depend on many factors, including the anisotropy of their emission, the lifetime of their obscured and unobscured phases, and the halo and large-scale environments that they inhabit.

As discussed in Chapters 2 and 3, this thesis places new constraints on these QSO properties by leveraging two unique surveys of faint galaxies around hyperluminous QSOs at $2.5 < z < 3$. In addition to advancing our understanding of QSO-galaxy interactions, the large number of faint galaxies (particularly low-stellar-mass Lyα emitters) in these surveys provides a unique oppportunity to study the properties of faint galaxies at high redshift, including the role of feedback and their surrounding gas in guiding their evolution. These results are discussed in Chapter 4.

Chapter 2

The Halo Masses and Galaxy Environments of Hyperluminous QSOs at $Z \simeq 2.7$ in the Keck Baryonic Structure Survey

---

This chapter was previously published as Trainor & Steidel 2012, ApJ, 752, 39.

Abstract

We present an analysis of the galaxy distribution surrounding 15 of the most luminous ($\gtrsim 10^{14}$ $L_\odot$; $M_{1450} \simeq -30$) QSOs in the sky with $z \simeq 2.7$. Our data are drawn from the Keck Baryonic Structure Survey (KBSS), which has been optimized to examine the small-scale interplay between galaxies and the intergalactic medium (IGM) during the peak of the galaxy formation era at $z \sim 2-3$. In this work, we use the positions and spectroscopic redshifts of 1558 galaxies that lie within $\sim 3'$ ($4.2h^{-1}$ comoving Mpc; cMpc) of the hyperluminous QSO (HLQSO) sightline in one of 15 independent survey fields, together with new measurements of the HLQSO systemic redshifts. By combining the spatial and redshift distributions, we measure the galaxy-HLQSO cross-correlation function, the galaxy-galaxy autocorrelation function, and the characteristic scale of galaxy overdensities surrounding the sites of exceedingly rare, extremely rapid, black hole accretion. On average, the HLQSOs lie within significant galaxy overdensities, characterized by a velocity dispersion $\sigma_v \simeq 200$ km s^{-1} and a transverse angular scale of $\sim 25''$ ($\sim$200 physical kpc). We argue that such scales are expected for small groups with $\log(M_h/M_\odot) \simeq 13$. The galaxy-HLQSO cross-correlation function has a best-fit correlation length $r_0^{GQ} = (7.3 \pm 1.3)h^{-1}$ cMpc, while the galaxy autocorrelation measured from the spectroscopic galaxy sample in the same fields has $r_0^{GG} = (6.0 \pm 0.5)h^{-1}$ cMpc. Based on a comparison with simulations evaluated at $z \sim 2.6$, these values imply that a typical galaxy lives in a host halo with $\log(M_h/M_\odot) = 11.9 \pm 0.1$, while HLQSOs inhabit host halos of $\log(M_h/M_\odot) = 12.3 \pm 0.5$. In spite of the extremely large black hole masses implied by their observed luminosities [$\log(M_{BH}/M_\odot) \gtrsim 9.7$], it appears that HLQSOs do not require environments very different from their much less luminous QSO counterparts. Evidently, the exceedingly low space density of HLQSOs ($\lesssim 10^{-9}$ cMpc^{-3}) results from a one-in-a-million event on scales $\ll 1$ Mpc, and not from being hosted by rare dark matter halos.

2.1 Introduction

The study of galaxies with supermassive black holes has become a topic of considerable interest, particularly since the discovery that properties of these black holes are strongly correlated with those of their host galaxies (e.g. Magorrian et al. 1998; Gebhardt et al. 2000; Ferrarese & Merritt 2000). The processes of supermassive black hole accretion and growth can produce spectacularly luminous QSOs, allowing their study over vast cosmological volumes ($0 < z \lesssim 7$). The details of these accretion processes, however, are concealed not only by distance, but also by our lack of knowledge concerning the duty cycle of AGN and the environments that drive and sustain their growth.

Because the brightest QSOs are extreme, ultra-luminous objects, it is often assumed that they must inhabit comparably rare environments. In particular, the rarity of these objects could arise because they require the highest mass dark matter halos, which are highly biased with respect to the overall matter distribution, or because of other, finely-tuned environmental factors that influence the availability of gas and the propensity for the black hole to accrete. As such, the masses and spatial distribution of the dark matter halos that host QSOs are of considerable interest, and detailed statistics on these quantities have become available through large-scale surveys, primarily through studies of QSO clustering using the two-point correlation function. Recent surveys have covered wide regions of the sky and large ranges of redshift, e.g., the Sloan Digital Sky Survey (SDSS; York et al. 2000; Eisenstein et al. 2011), the 2dF QSO Redshift Survey (2QZ; Croom et al. 2004), and the DEEP2 Redshift Survey (Davis et al. 2003).

Because these surveys include QSOs with a wide range of luminosities and redshifts, the QSO autocorrelation function has been frequently used to constrain QSO clustering out to high redshifts using the SDSS samples (e.g. Myers et al. 2006, 2007; Shen et al. 2007, 2010; Ross et al. 2009), 2QZ samples (e.g. Porciani et al. 2004; Porciani & Norberg 2006; Croom et al. 2005), and combined 2dF-SDSS LRG and QSO survey (2SLAQ; survey description in Croom et al. 2009, clustering results in da Ângela et al. 2008). The results of these analyses are in broad agreement that QSOs inhabit host dark matter halos of mass $\log(\mathrm{M_h/M_\odot}) \sim 12.5$ at redshifts $z \lesssim 3$. Due to the low space density of QSOs at all redshifts, these autocorrelation measurements have generally been confined to large scales, but complementary measurements have also been obtained: Hennawi et al. (2006) and Shen et al. (2010) conducted surveys for close QSO pairs; the galaxy-QSO cross-correlation function was measured by Adelberger & Steidel (2005b), in the DEEP2 survey at $z \sim 1$ by Coil et al. (2007), and in a low redshift ($z < 0.6$) SDSS QSO sample by Padmanabhan et al. (2009). These studies generally agree with the QSO autocorrelation results, and the mass scale $\log(\mathrm{M_h/M_\odot}) \sim 12.5$ seems fairly well-established for the general population of QSOs at $z \lesssim 3$.

However, studies which divide the population of QSOs into specific subsamples reveal a more complicated picture of the dependence of QSO properties on halo mass. Low-redshift studies display a possible relation between obscuration and host halo mass (Hickox et al. 2011), which may be significant at higher redshifts, where the population of obscured QSOs is relatively unconstrained. Shen et al. (2010) find that radio-loud QSOs are more strongly clustered than radio-quiet QSOs matched in redshift and optical luminosity. In addition, there is an expected dependence of QSO luminosity on host halo mass because the QSO luminosity depends on black hole mass, which in turn exhibits the aforementioned association with the mass of the host halo. In practice, however, QSO luminosities depend in detail on the availability of matter to accrete and the physical processes governing the efficiency with which this accretion occurs. Thus, it is perhaps not surprising that the clustering of QSOs shows little association with QSO luminosity in observations near $z \sim 2$ (e.g. Adelberger & Steidel 2005b; Croom et al. 2005; da Ângela et al. 2008, and in simulations by Lidz et al. 2006); however, Shen et al. (2010) detect stronger clustering among the most luminous QSOs in their sample at $z > 2.9$, and Krumpe et al. (2010) find that SDSS QSOs at $z \sim 0.25$ cluster more strongly with increasing X-ray luminosity. Finally, the survey of close QSO pairs by Hennawi et al. (2006) reveals an excess at the smallest scales, which the authors attribute to dissipative interaction events that trigger QSO activity in rich environments. In short, the properties of QSOs are related to their host halo masses in a complex manner, and it is clear that other environmental factors are at play.

In this chapter we study the environments of hyperluminous QSOs (HLQSOs; defined here by a luminosity $\log(\nu L_\nu/L_\odot) \gtrsim 14$ at a rest-frame wavelength of 1450 Å) at $2.5 \lesssim z \lesssim 3$ by measuring the magnitude and scale of overdensities in the galaxy distribution at small ($\lesssim 3'$) projected distances using data from the Keck Baryonic Structure Survey (KBSS). This approach complements existing studies in numerous ways: targeting narrow fields allows us to study the local environments of these extremely rare HLQSOs, including the galaxies at comparable redshifts that lie far below the flux limits of the typical wide-field QSO surveys. In this way we are able to constrain the properties of the relatively unexplored environments of the highest-luminosity QSOs. Focusing on the brightest QSOs should reveal whether host halo mass plays a significant role in determining QSO properties, while sensitivity to the local environment may demonstrate whether these HLQSOs are associated with the types of environments where mergers and dissipative interaction are expected to be most common.

This chapter is organized as follows: in §2.2 we discuss the observations used in this study; §2.3 describes the techniques used to construct an unbiased measure of the galaxy distribution around the HLQSOs and our estimates of the magnitude and scale of the surrounding galaxy overdensities. In §2.4, we describe and implement a method for estimating the small-scale galaxy-HLQSO correlation function and galaxy-galaxy autocorrelation function from our data along with the implied galaxy and HLQSO host halo masses. In §2.5 we present evidence that the HLQSOs inhabit group-sized virialized structures conducive to merger events; a summary is given in §2.6. Throughout this chapter, we will assume $\Omega_\mathrm{m} = 0.3$, $\Omega_\Lambda = 0.7$, and $h = H_0/(100$ km s^{-1}). We have left all comoving length scales in terms of h for ease of comparison to previous studies, but we quote physical scales, luminosities, and halo masses assuming $h = 0.7$. For further clarity, we denote comoving distance scales in units of cMpc (comoving Mpc) and physical scales as pkpc (physical kpc).

Table 2.1. HLQSO Redshifts and Corrections

QSO	NIR Spectra Source[a]	$z_{\rm new}$[b]	$z_{\rm old}$[c]	Δz	Δv (km s^{-1})
Q0100+13 (PHL957)	Keck II/NIRSPEC	2.721 ± 0.003	2.681	–0.040	–3214
HS0105+1619	P200/TSPEC	2.652 ± 0.003	2.640	–0.012	–983
Q0142–10 (UM673a)	Keck II/NIRSPEC	2.743 ± 0.003	2.731	–0.012	–943
Q0207–003 (UM402)	P200/TSPEC	2.872 ± 0.003	2.850	–0.022	–1699
Q0449–1645	P200/TSPEC	2.684 ± 0.003	2.600	–0.084	–6818
Q0821+3107 (NVSS)	P200/TSPEC	2.616 ± 0.003	2.624	+0.008	+686
Q1009+29 (CSO 38)	Keck II/NIRSPEC	2.652 ± 0.003	2.620	–0.032	–2620
SBS1217+490	P200/TSPEC	2.704 ± 0.003	2.698	–0.006	–484
HS1442+2931	P200/TSPEC	2.660 ± 0.003	2.638	–0.022	–1797
HS1549+1919	Keck II/NIRSPEC	2.843 ± 0.003	2.830	–0.013	–1011
HS1603+3820	P200/TSPEC	2.551 ± 0.003	2.510	–0.041	–3452
Q1623+268 (KP77)[d]	Keck II/NIRSPEC	2.5353 ± 0.0005	2.518	–0.018	–1489
HS1700+6416	Keck II/NIRSPEC	2.751 ± 0.003	2.736	–0.015	–1220
Q2206–199 (LBQS)	Keck II/NIRSPEC	2.573 ± 0.003	2.558	–0.015	–1255
Q2343+12 (also SDSS)	Keck II/NIRSPEC	2.573 ± 0.003	2.515	–0.058	–4854

[a] Refers to the instrument used to measure the near-IR QSO spectra and redshift. NIRSPEC is used on the Keck II telescope, while P200 is the Palomar Hale 200-inch telescope, used with the TripleSpec instrument.

[b] $z_{\rm new}$ refers to the redshift used in this analysis.

[c] $z_{\rm old}$ refers to the previous published redshift value.

[d] The redshift for Q1623+268 (KP77) is more tightly constrained because of the presence of narrow [O III] lines at the presumed systemic redshift of the QSO.

2.2 Data

The data used in this study form part of the Keck Baryonic Structure Survey (KBSS; Steidel et al. 2012), a large sample ($N_{\rm gal}$ = 2298) of high-redshift star-forming galaxies ($1.5 < z < 3.6$) close to the lines-of-sight of 15 HLQSOs at redshifts 2.5<z<2.9. Because we have observed fields of differing solid angle around each of these HLQSOs, we standardized the fields for the purposes of this study by including only those galaxies within $\delta\theta \sim 3'$ ($4.2h^{-1}$ cMpc at the HLQSO redshifts) of the line-of-sight of the HLQSO in each, an area that is well-sampled for all 15 fields. This subset of the total KBSS dataset contains 1558 galaxies and comprises the entire sample used in this chapter.

2.2.1 HLQSO Redshifts

An important prerequisite to establishing the galaxy environment of the HLQSOs is an accurate measurement of the HLQSO systemic redshifts. Redshifts for QSOs in the range $2 \lesssim z_{\rm QSO} \lesssim 3$ are typically measured from the peaks or centroids of broad emission lines of relatively high ionization species in the rest-frame far-UV (e.g., N V λ1240, C IV λ1549, Si IV λ1399, C III] λ1909). These lines are known to yield redshifts that differ significantly from systemic, and tend to be blue-shifted by several hundred to several thousand km s^{-1} (see e.g. McIntosh et al. 1999; Richards et al. 2002; Gonçalves et al. 2008). These velocity offsets also tend to increase with QSO luminosity, thus making the present sample of hyperluminous QSOs particularly susceptible to this issue. In view of the importance of precise redshifts to locate the HLQSO environments

Table 2.2. Galaxy Samples and HLQSO Properties

Field	$z_{\rm QSO}$[a]	L_{1450}[b] ($10^{13}L_\odot$)	$M_{\rm BH}$[c] ($10^{9}M_\odot$)	$N_{\rm BX}$	$N_{\rm MD}$	$N_{\rm CDM}$	$N_{\rm tot}$	N_{1500}[d]
Q0100+13	2.721	6.4	2.0	68	12	15	95	7
HS0105+1619	2.652	4.5	1.4	74	6	23	103	7
Q0142–10[e]	2.743	<6.4	<2.0	75	13	16	104	1
Q0207–003	2.872	6.1	1.9	54	12	27	93	7
Q0449–1645	2.684	4.0	1.3	68	12	31	111	9
Q0821+3107[f]	2.616	4.1	1.3	64	7	21	92	4
Q1009+29	2.652	10.9	3.4	54	19	43	116	8
SBS1217+490	2.704	5.1	1.6	67	14	11	92	3
Q1442+2931	2.660	4.9	1.5	71	25	22	118	3
HS1549+1919	2.843	14.9	4.6	54	14	39	107	23
HS1603+3820	2.551	11.0	3.4	80	15	14	109	10
Q1623–KP77[f]	2.5353	3.2	1.0	82	9	12	103	7
HS1700+6416	2.751	13.6	4.3	69	16	16	101	6
Q2206–199	2.573	4.5	1.4	78	11	20	109	0
Q2343+12	2.573	3.8	1.2	71	9	25	105	6

[a] $z_{\rm QSO}$ refers to the systemic redshift of the field defined by the HLQSO (see Table 2.1 and §2.2.1).

[b] L_{1450} refers to the estimated luminosity νL_ν near a rest-frame wavelength $\lambda_{\rm rest} \simeq 1450$, extrapolated from the g' and r' magnitudes from the SDSS (Eisenstein et al. 2011) database when available, and otherwise from our own measurements. We have assumed $h = 0.7$.

[c] $M_{\rm BH}$ is the minimum black hole mass capable of producing a QSO with luminosity L_{1450}, assuming Eddington-limited accretion (§2.4.6).

[d] $N_{1500} = {\rm N}(|\delta v| < 1500$ km s^{-1}) is the number of galaxies in the field that have spectroscopic redshifts within 1500 km s^{-1} of their corresponding HLQSO.

[e] Q0142-10 (UM673a) is known to be gravitationally lensed (Surdej et al. 1987) and has an unknown magnification; the estimated luminosity and mass are therefore upper limits.

[f] Q0821+3107 and Q1623–KP77 are the only HLQSOs in our sample with radio detections. Q0821 has a flux $f_\nu = 162$ mJy at 4830 MHz (Langston et al. 1990); KP77 has a flux $f_\nu = 6.4$ mJy at 1.4 GHz (Condon et al. 1998).

within the survey volume, we obtained near-IR spectra of the entire sample using NIRSPEC on the Keck II 10m telescope, TripleSpec on the Palomar 200-inch (5m) telescope, and in some cases, both (see Table 2.1).

Among the 15 HLQSOs in the sample, narrow forbidden lines ([O III] λ5007) were detected for only 2 of them (Q1623+268, Q2343+12), either because no such lines were present in the spectra (common at the highest luminosities), or because the HLQSO redshift was such that the strongest transitions fell in regions between the near-IR atmospheric bands. However, in all cases we were able to measure one or more hydrogen Balmer lines and the Mg II λ2798 line, which were mutually consistent and are known to be closer to the true systemic redshift than the high ionization lines in the UV (McIntosh et al. 1999; Richards et al. 2002). The redshifts obtained from the Balmer/Mg II lines (which agree well with that given by [O III] in the two cases where all were measured) were then subjected to several cross-checks, including the wavelength at the onset of the Lyman-α forest measured from the high resolution HLQSO spectra (a lower limit on the systemic redshift, but one which agrees to within $\Delta z \simeq 0.001$ of the Balmer line redshift in all but two cases); the redshift of narrow He II λ1640 in intermediate resolution optical spectra of the HLQSOs; and, in several cases, regions exhibiting narrow Lyα emission were discovered with small angular separations from the HLQSO, and we have found that such nebulae lie very close to the systemic redshift of the nearby HLQSO. In two cases (HS1603+3820 and Q1009+29) this last criterion led to a significant modification ($\Delta z \sim +0.01$, or $\sim$ 800 km s^{-1}) of the redshift suggested by the near-IR spectroscopy. We adopt a HLQSO redshift uncertainty σ_z = 270 km s^{-1} (for those HLQSOs without measured [O III] redshifts) based on the measured dispersion of the Mg II line with respect to [O III] by Richards et al. (2002); the broad agreement among our many redshift criteria suggest that this is a conservative estimate of the redshift uncertainties.

Table 2.1 summarizes the adopted redshifts for all 15 HLQSOs based on these considerations; also given (column 4; $z_{\rm old}$) is the published redshift for each and the redshift and velocity error that would result from adopting the published values ($\Delta z \equiv z_{old} - z_{new}$). As expected, all but one of the old redshifts are systematically too low (the median shift is ~ -1500 km s^{-1}, and the mean ~ -2100 km s^{-1}). Failure to account for these large velocity errors would severely compromise our measurements. As we show below, the measured $z_{\rm QSO}$ values must be quite accurate given the very tight redshift-space correlation between the HLQSOs and the spectroscopically measured, continuum-selected galaxies nearby.

2.2.2 Galaxy Redshifts

Galaxy redshifts were measured using low-resolution ($\sim$5Å), rest-frame UV spectra obtained with the LRIS multi-object spectrograph on the Keck I telescope (Oke et al. 1995; Steidel et al. 2004). Candidate galaxies were color-selected using the Lyman-break technique and were sorted as BX ($z \sim 2.2$), MD ($z \sim 2.6$), or CDM ($z \sim 3$) galaxies based on the color criteria discussed in Steidel et al. (2003) and Adelberger et al. (2004); the data collection and reduction procedures are described therein. All galaxies in the spectroscopic sample have $\mathcal{R} < 25.5$ [where $\mathcal{R} \equiv$ m$_{\rm AB}$(6830Å)], which corresponds to M$_{\rm AB}$(1700Å) $\lesssim -19.9$ at $z \sim 2.7$ (about 1 magnitude fainter than M$_*$ at this redshift; see Reddy et al. 2008). Redshifts were determined by a combination of Lyα emission or absorption and far-UV interstellar (IS) absorption. Since Lyα emission tends to be redshifted with respect to the systemic redshift of the host galaxy, and interstellar absorption tends to be blueshifted (see e.g. Shapley et al. 2003; Adelberger et al. 2003; Steidel et al. 2010), we estimate each galaxy's systemic redshift via the method proposed in Adelberger et al. (2005a) and updated by Steidel et al. (2010). In this method, the average Lyα emission and IS absorption offsets are calculated based on the redshift of the Hα nebular line (NIR spectroscopy is available for a subset of the galaxy sample), which traces ionized gas in star-forming regions of the galaxy, and is thus a more accurate estimate of the systemic redshift. Rakic et al. (2011) derive similar corrections for the same galaxy sample using the expected symmetry of IGM absorption about the systemic redshift of the galaxy.

We estimate the systemic galaxy redshifts ($z_{\rm gal}$) based on a combination of the above results. A more detailed discussion of our correction formulae can be found in Rudie et al. (2011; in prep.), but the formulae are reproduced below. For galaxies with NIR spectra (e.g. the Hα line), the NIR redshift is used with no correction. For galaxies with measured Lyα emission but without interstellar absorption, we use the following estimate:

$$z_{\rm gal} \equiv z_{\rm Ly\alpha} + \frac{\Delta v_{\rm Ly\alpha}}{c}\left(1+z_{\rm Ly\alpha}\right) , \tag{2.1}$$

where $z_{\rm Ly\alpha}$ is the redshift of the measured Lyα emission and $\Delta v_{\rm Ly\alpha} = -300$ km s^{-1} is the velocity shift needed to transform the Lyα redshift to the systemic value, $z_{\rm gal}$.

For galaxies with interstellar absorption, we use an estimate based on the absorption redshift whether or not Lyα emission is present:

$$z_{\rm gal} \equiv z_{\rm IS} + \frac{\Delta v_{\rm IS}}{c}\left(1+z_{\rm IS}\right) , \tag{2.2}$$

where $z_{\rm IS}$ is the redshift of the measured interstellar absorption and $\Delta v_{\rm Ly\alpha} = 160$ km s^{-1} is the velocity shift needed to transform the absorption redshift to the systemic value.

For galaxies with both interstellar absorption and Lyα emission, we verify that the corrected absorption redshift does not exceed the measured redshift of the Lyα line; that is, we verify that $z_{\rm IS} < z_{\rm gal} < z_{\rm Ly\alpha}$, where $z_{\rm gal}$ is calculated using Eq. 2.2 above. If this condition is not satisfied, we recompute the galaxy systemic redshift as the average of the absorption and emission redshifts:

$$z_{\rm gal} \equiv \frac{z_{\rm IS} + z_{\rm Ly\alpha}}{2} . \tag{2.3}$$

The residual redshift errors (calculated from the galaxies in the NIR sample) have a standard deviation $\sigma_{\rm v,err} = 125$ km s^{-1}, which we adopt as the uncertainty in our galaxy redshift measurements.

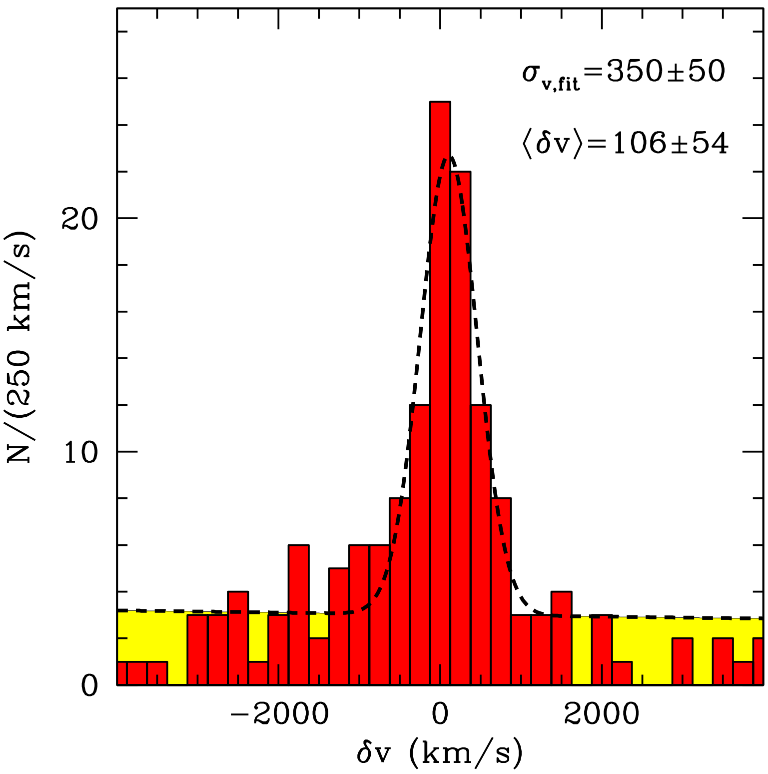

Figure 2.1: Velocity distribution of galaxies with respect to their nearest HLQSOs, stacked for all 15 HLQSO fields. The velocity δv is given by Eq. 2.4, where $\delta v = 0$ for a galaxy at the redshift of its corresponding HLQSO. The yellow shaded area corresponds to the selection function, constructed as described in §2.3.1. The dashed curve is a gaussian profile fit to the overdensity, with $\sigma_{\mathrm{v,fit}} = 350$ km s^{-1}. After removing the effect of our $\sigma_{\mathrm{v,err}} \sim 125$ km s^{-1} (270 km s^{-1}) galaxy (HLQSO) redshift errors, we estimate a peculiar velocity scale of $\sigma_{\mathrm{v,pec}} \simeq 200$ km s^{-1} for the galaxies associated with the overdensity, with an offset $\langle\delta v\rangle = 106\pm54$ km s^{-1} from the HLQSO redshifts.

2.3 Redshift Overdensity

In order to consider the positions of the galaxies relative to their corresponding HLQSOs in redshift space while accounting for the differences in the HLQSO redshifts between fields, the redshift of each galaxy was transformed into a velocity relative to its associated HLQSO. For a galaxy with index *i* in a field with index *j*, this velocity difference is given by

$$\delta v_{i,j} = \frac{c}{1+z_{\mathrm{QSO},j}}(z_{\mathrm{gal},i} - z_{\mathrm{QSO},j})\ . \tag{2.4}$$

Once transformed to units of velocity, the distributions of galaxies relative to their HLQSOs were stacked to reveal the average environment of HLQSOs in terms of the local galaxy number density (per unit velocity)—this distribution is shown in Fig. 2.1. The distribution shows a well-defined peak near $\delta v = 0$, indicating the presence of significant clustering of the galaxies around the HLQSO redshifts. We attribute the slight offset of the overdensity from the HLQSO redshifts (fit $\langle\delta v\rangle = 106\pm54$ km s^{-1}) to a residual systematic offset in our determination of the HLQSO redshifts.

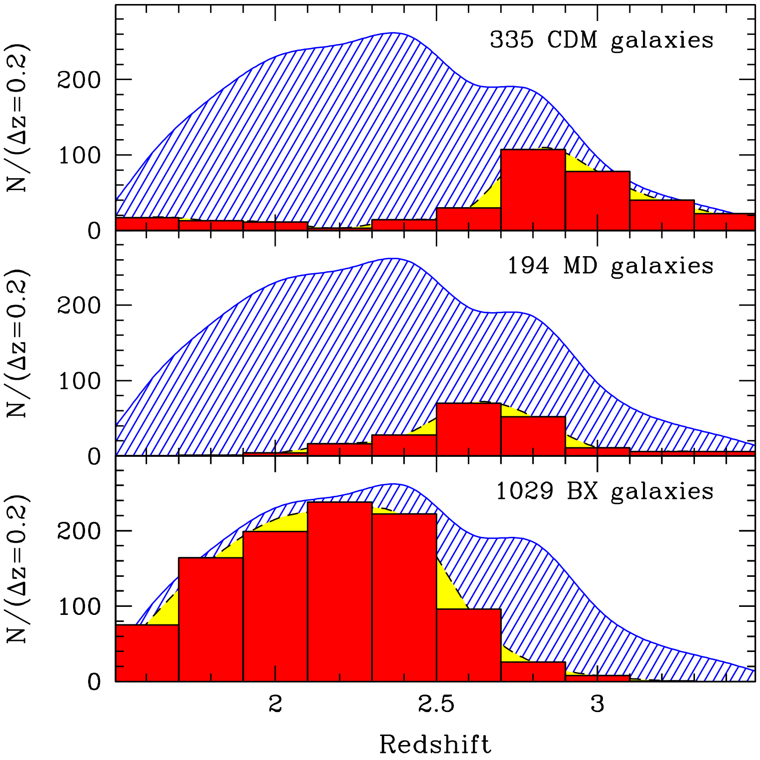

Figure 2.2: Redshift distributions for BX, MD, and CDM color-selected galaxy types. Red histograms display the measured distributions of all such galaxies in each sample, while the yellow region represents the fit spline function specific to the color-selected sample (i.e., $\mathcal{N}_{\rm BX}(z)$, $\mathcal{N}_{\rm MD}(z)$, and $\mathcal{N}_{\rm CDM}(z)$). The blue hashed region is the overall redshift selection function for all color types.

2.3.1 Building the Selection Function

Clustering measurements can be grossly misinterpreted when the relevant selection functions are not well-understood (Adelberger 2005). While the criteria for selecting galaxies for follow-up spectroscopy were identical for all 15 of the KBSS fields, small differences in image depth and seeing, as well as slight changes in the algorithms used for assigning relative weights in the process of designing slit masks, can lead to field-to-field variations in the redshift selection functions. To at least partially mitigate such variations in the redshift-space sampling between fields, we used the number of successfully observed BX, MD, and CDM galaxies in each field to estimate the form of our field-specific selection functions $\mathcal{N}_{\rm j}(z)$. These estimates of the selection functions were constructed as follows.

First, the redshift distributions of all BX, MD, and CDM galaxies in our sample were arranged in a coarse histogram with bins of width $\Delta z = 0.2$. A spline fit was then performed to estimate the smooth distribution functions of each galaxy type—the histograms and spline fits for each type are displayed in Fig. 2.2.

For each field, we built a field-specific selection function by combining these galaxy redshift distributions for each color criterion according to the number of those galaxies successfully observed in the field. Thus for a field with index j, the redshift selection function is given by Eq. 2.5:

$$\begin{aligned}\mathcal{N}_j(z) \quad = \quad & N_{\mathrm{BX,j}}\mathcal{N}_{\mathrm{BX}}(z) + \\ & N_{\mathrm{MD,j}}\mathcal{N}_{\mathrm{MD}}(z) + \\ & N_{\mathrm{CDM,j}}\mathcal{N}_{\mathrm{CDM}}(z)\ ,\end{aligned} \tag{2.5}$$

where $N_{\mathrm{BX,j}}$ corresponds to the number of BX-selected galaxies in field j, $\mathcal{N}_{\mathrm{BX}}$ is the selection function for BX-selected galaxies over all fields, and other variables are defined similarly. We then transform these redshift-space selection functions into units of velocity relative to their corresponding bright HLQSOs using Eq. 2.4. Finally, we combined this set of field-specific velocity-space selection functions (already weighted by the number of galaxies in each field) into a single stacked function:

$$\mathcal{N}(v) = \sum_{j=1}^{15} \mathcal{N}_j(v)\ . \tag{2.6}$$

The resulting selection function is fairly flat over the range $|\delta \mathrm{v}| < 20000$ km s^{-1} with a slight negative slope (yellow shading in Fig. 2.1), indicating our slight bias toward detecting objects “in front" of the HLQSO (that is, at lower redshifts) compared to galaxies slightly “behind” the HLQSO in each field. The selection function is thus a prediction for the observed distribution of galaxies in relative-velocity space in the absence of clustering.

2.3.2 Bias in Field Selection

We previously knew one KBSS field (HS1549+1919) to have a large overdensity in the galaxy distribution very close to the redshift of the central HLQSO. The variation in overdensity among fields can be estimated by N_{1500} in Table 2.2, which is the number of galaxies within 1500 km s^{-1} of the HLQSO redshift for that field. In order to ensure that our clustering results are not being dominated by a single field, we repeated our analysis on subsamples of the data consisting of 14 of the 15 fields, removing a different field each time. In each case the magnitude and scale of the overdensity was consistent with that observed when all 15 fields were included in the analysis, indicating that the observed magnitude and scale of the overdensity are not determined by any single field.

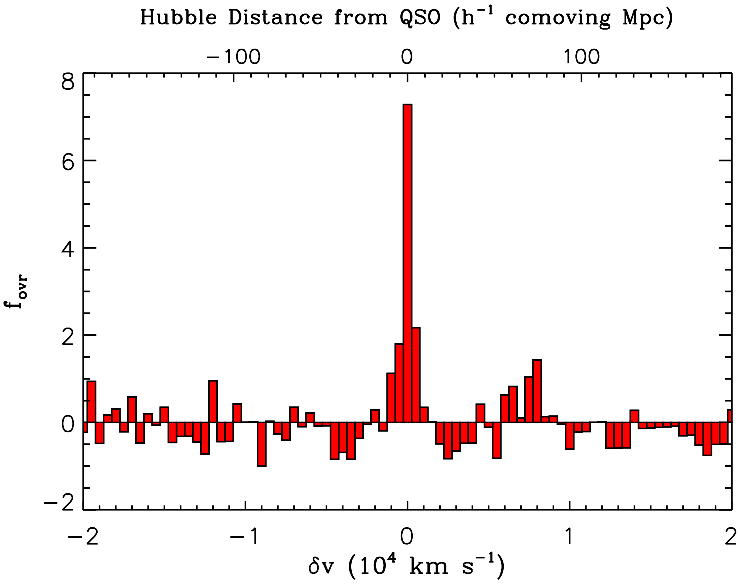

Figure 2.3: The relative overdensity $f_{\rm ovr}$ (Eq. 2.7) as a function of velocity relative to the central HLQSOs over a wide velocity range. The overdensity is measured in bins of 500 km s^{-1}, as this Hubble flow velocity roughly corresponds to the same physical scale as our transverse field of view ($5h^{-1}$ cMpc $\sim$ 500 km s^{-1}). See §2.3.1 for details on the selection function.

2.3.3 Redshift Clustering Results

Fig. 2.1 shows the observed galaxy distribution in units of velocity along with the selection function estimate from §2.3.1. The peak in the galaxy distribution near the HLQSO redshifts is clearly visible. Fitting a Gaussian function to the histogram in Fig. 2.1 gives a velocity width $\sigma_{\rm v,fit} = 350\pm50$ km s^{-1}, which includes the effect our $\sigma_{\rm v,err} \simeq 125$ km s^{-1} galaxy redshift errors and the random residual errors in our HLQSO redshifts, assumed to be $\sigma_{\rm v,err} \sim 270$ km s^{-1}. After subtracting the redshift errors in quadrature, we find an intrinsic velocity width of $\sigma_{\rm v,pec} \simeq 200$ km s^{-1} for the galaxy overdensity, which we attribute to peculiar velocities. Note that the residual HLQSO redshift errors are uncertain and likely to be largely systematic (see §2.2.1), so our estimated velocity dispersion is an upper limit on the true peculiar velocity scale if the random component of the HLQSO redshift error is larger than we have assumed.

We also consider the relative overdensity at the HLQSO redshift by comparing the observed density to that predicted by our selection function. The distribution is plotted as a relative overdensity

$$f_{\rm ovr} = (N_{\rm obs} - N_{\rm pred})/N_{\rm pred} \tag{2.7}$$

in Fig. 2.3, where $N_{\rm obs}$ is the number of galaxies observed in a given velocity bin and $N_{\rm pred}$ is the number predicted for that bin by our selection function. The relative overdensity is measured in bins with $\Delta v = 500$ km s^{-1}; this scale was chosen to correspond roughly to the transverse scale of our field, since a Hubble-flow velocity of 500 km s^{-1} $\sim 5h^{-1}$ cMpc at these redshifts. Fig. 2.3 shows that the HLQSOs are associated (on average) with a $\delta n/n \sim 7$ overdensity of galaxies when considered on the $\sim 5h^{-1}$ Mpc scale of our field, with no features of comparable amplitude over a wide range of redshifts (40000 km s^{-1} corresponds to $\Delta z \simeq 0.5$ at $z \simeq 2.7$).

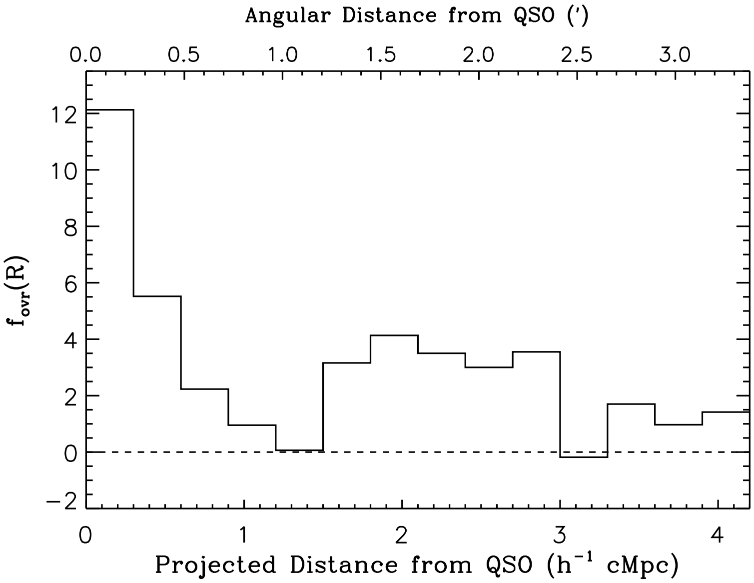

Figure 2.4: For each projected circular annulus, the relative overdensity ($f_{\rm ovr}$; Eq. 2.7) of galaxies within 1500 km s^{-1} of the HLQSO with respect to the redshift selection function and angular selection function. The overdensity of galaxies is localized for the most part to a tranverse scale $R \lesssim 0.5h^{-1}$ cMpc.

Repeating this analysis after dividing the galaxies into radial annuli, we find that the redshift association is most pronounced for those galaxies within 25″ of the HLQSO line of sight (∼200 pkpc), though a lower level of redshift clustering does extend to larger projected distances (see Fig. 2.4). If this distance is taken as an isotropic spatial scale of the galaxy overdensity, then the line-of-sight velocity dispersion due to the Hubble flow would be only ∼65 km s^{-1}. However, a less-significant overdensity does extend to larger radii, and thus likely includes many galaxies that are clustered around the HLQSO but move with the Hubble flow. In order to ensure that the measured velocity width is not inflated by these non-virialized galaxies, we directly measure the velocity dispersion among the 15 galaxies within 1500 km s^{-1} and 0.5 h^{-1} cMpc (200 pkpc) of the HLQSOs; as discussed in §2.5, these galaxies are likely to be virialized and associated with the HLQSO, and our selection functions predict only 1.5 galaxies in this volume in the absence of clustering. These 15 galaxy velocities have a sample standard deviation of 335 km s^{-1}, consistent with the velocity width measured for the entire overdensity. The observed velocity spread is thus presumably set by peculiar velocities of $\sigma_{\rm v,pec} \simeq 200$ km s^{-1} among the HLQSO-associated galaxies.

A comparison of Figs. 2.3 & 2.4 demonstrates that the relative overdensity is highly scale-dependent. If we assume that the width of the overdensity in velocity space is entirely due to peculiar velocities, and hence that all 15 of the galaxies observed with $R < 0.5h^{-1}$ cMpc and $|\delta v| < 500$ km s^{-1} are physically located within a three-dimensional distance $r < 0.5h^{-1}$ cMpc from their nearest HLQSO, then the number of galaxies in this composite volume is ∼50x the number predicted by our redshift and angular selection functions (described in §2.3.1 & §2.4.1.1, respectively).

2.4 Correlation Function Estimates

2.4.1 Galaxy-HLQSO Cross-Correlation Function

Much of the recent work on QSO clustering relies on large-scale two-point correlation functions, particularly the QSO autocorrelation function (see, e.g., Shen et al. 2007). The galaxy-HLQSO cross-correlation function ξ_Q can provide a complementary estimate of HLQSO host halo mass.

The correlation function is defined as the excess conditional probability of finding a galaxy in a volume dV at a distance $r = |\mathbf{r}_1 - \mathbf{r}_2|$, given that there is a HLQSO at point $\mathbf{r}_1$, such that $P(\mathbf{r}_2|\mathbf{r}_1)dV = P_0[1+\xi(r)]dV$, where $P_0 dV$ is the probability of finding a galaxy at an average place in the universe. Here we assume a power-law form for the correlation function: $\xi_{\rm GQ} = (r/r_0^{\rm GQ})^{-\gamma}$, where γ is the slope parameter and r_0 corresponds to the comoving distance at which the local number density of galaxies is twice that of an average place in the universe.

Many recent analyses of the two-point correlation function have dispensed with power-law fits in favor of directly modeling the halo-occupation distribution (HOD; see, e.g., Seljak 2000; Berlind & Weinberg 2002; Zehavi et al. 2004) based on the theory of Press & Schechter (1974) and a statistical method of populating dark matter (DM) halos with galaxies. A general feature of these HOD models is a deviation from a single power law at distances near $1h^{-1}$ cMpc due to a transition from the single-halo regime (the clustering of galaxies/QSOs within a single dark-matter halo) to the two halo regime (the clustering of galaxies/QSOs hosted by distinct halos).

In this chapter we implement the simpler power-law fitting technique for the following reasons. First, our smaller sample (with respect to the large surveys at low redshift) does not allow us to detect a deviation from a power-law fit with any significance, particularly for the galaxy-HLQSO cross-correlation. Second, our choice to fix the power-law slope γ (see below) desensitizes our result to the precise shape of the correlation function, leaving the clustering length $r_0^{\rm GQ}$ to primarily reflect the integrated pair-probability excess over the range of projected distances in our sample.

In practice, the three-dimensional correlation function $\xi(r)$ is not directly measurable: line-of-sight velocities are an imperfect proxy for radial distance due to peculiar velocities and redshift errors. As such, it is more useful to consider the reduced angular correlation function, $w_p(R|\Delta z)$ by integrating over a redshift or velocity window:

$$P(R)d\Omega = P_0' d\Omega \left[1 + w_p(R)\right] = d\Omega \int_{\Delta z} P(r) dz \,, \tag{2.8}$$

where $R = D_A(z)\theta(1+z)$ is the projected comoving distance from the HLQSO, and $D_A(z)$ is the angular diameter distance to the HLQSO. In the limit $\Delta z \to \infty$, and assuming a power-law form of the three-dimensional correlation function, it can be shown that the reduced angular correlation function has an equally simple power-law form:

$$w_p(R) = AR^{-\eta} \tag{2.9}$$

with $\eta = \gamma - 1$. However, we would like to restrict our analysis to small redshift/velocity scales, choosing a value of Δz that includes the entire clustering signal while eliminating the noise contribution of uncorrelated structure at large line-of-sight separations from the HLQSO, and this priority precludes the assumption of $\Delta z \to \infty$. In the case of a truncated redshift range, the reduced angular correlation function does not simplify to a power-law, and instead takes the form of a Gaussian hypergeometric function, denoted as ${}_2F_1(a,b;c;z)$. In our particular case, the reduced angular cross-correlation function w_p^{GQ} is expressed by the following:

$$\begin{aligned} w_p^{\mathrm{GQ}}(R) &= \int_{-z_0}^{z_0} (r/r_0^{\mathrm{GQ}})^{-\gamma} dz = \int_{-z_0}^{z_0} (\sqrt{R^2+z^2}/r_0^{\mathrm{GQ}})^{-\gamma} dz \\ &= \left(\frac{r_0^{\mathrm{GQ}}}{R}\right)^{\gamma} {}_2F_1\left(\frac{1}{2}, \frac{\gamma}{2}; \frac{3}{2}; \frac{-z_0^2}{R^2}\right) \end{aligned} \tag{2.10}$$

where z_0 is the half-width of the redshift window over which we compute the clustering strength. We choose a value z_0 = 1500 km s$^{-1} \simeq 14h^{-1}$ cMpc in order to encompass the entire observed overdensity (see Fig. 2.1) and the range of projected distances we are able to probe ($R < 4.2h^{-1}$ cMpc) without including excess noise. We then fit the reduced angular correlation function $w_p^{\mathrm{GQ}}(R|r_0^{\mathrm{GQ}}, \gamma)$ to the data by variation of the correlation length r_0^{GQ}. We fix $\gamma = 1.5$ for simplicity in matching our data to halo populations (see §2.4.3); this value of γ was chosen as it is a reasonably good fit to both the galaxy autocorrelation function and galaxy-HLQSO cross-correlation function, as well as the correlation functions among the simulated halo populations. Increasing the value of γ causes the best-fit value of r_0^{GQ} to decrease, but the corresponding halo mass is very insensitive to the choice of γ, so long as the same value is used for both the galaxy and the simulated halo populations.

In order to estimate $w_p^{\mathrm{GQ}}(R)$ from our data, we separate our fields into projected circular annuli of varying widths, constructed so that each annulus has a roughly similar signal-to-noise ratio, and with our largest annulus having its outer edge $\sim 200''$ from the HLQSO, a projected distance of $R = 4.2h^{-1}$ cMpc. As noted above, we wish to restrict our analysis to those galaxies that are closely associated with a HLQSO in redshift as well as projected position, so we also separate our galaxy sample into two velocity groups: one with $|\delta v| \leq 1500$ km s^{-1} and one with $|\delta v| > 1500$ km s^{-1}. In this way, we define $N_v(R_k)$ as the number of velocity-associated galaxies in the k$^{\mathrm{th}}$ annular bin and $N_0(R_k)$ as the number of non-associated galaxies in the bin.[2] The solid angle covered by the k$^{\mathrm{th}}$ annular bin is given by $\mathcal{A}_k = \pi(R^2_{\mathrm{outer,k}} - R^2_{\mathrm{inner,k}})$; thus we likewise define the area densities of galaxies $\Sigma_{v,0}(R_k) = N_{v,0}(R_k)/\mathcal{A}_k$.

---

[2] In this chapter, we will use the subscript or superscript v to denote velocity-associated galaxies, and 0 to denote non-associated galaxies.

We then used the selection function constructed in §2.3.1 to estimate the expected number of galaxies in each velocity group [i.e., $\mathcal{N}_v = \mathcal{N}(|\delta v| < 1500)$ and $\mathcal{N}_0 = \mathcal{N}(|\delta v| > 1500)$], which we convert to expected average area densities for each velocity group ($\Sigma_{v,0}^{\rm pred} = \mathcal{N}_{v,0}/\mathcal{A}_{\rm field}$). Finally, we divide the measured area densities by the average predicted value to define the relative overdensity of each annulus. If the overdensity $\Sigma_v(R_k)/\Sigma_v^{\rm pred}$ is purely due to the clustering signal, then the reduced angular cross-correlation function is given by $w_p^{\rm GQ} = \Sigma_{\rm v,obs}^{\rm GQ}(R_k)/\Sigma_{\rm v,pred}^{\rm GQ} - 1$; however, this assumption is invalid if the angular sampling of the field is not uniform, which we explore below.

2.4.1.1 Angular Selection Function

The use of the redshift selection function in $N_{\rm pred}$ ensures that large-scale variations and sampling biases in redshift are taken into account in our analysis. Selection biases can also occur in the plane of the sky; because our fields are centered on their HLQSOs, any bias that varies with distance from the center of the field will mimic a change in the correlation function. To account for this effect, we recall that galaxies with $|\delta v| > 1500$ km s^{-1} show no association with the HLQSO (see Fig. 2.1), and therefore should be uniformly distributed on average. Therefore, if the function $\Sigma_0(R)$ is not a constant, it must describe a non-uniform angular selection function, which encapsulates variations in optical selection sensitivity (e.g. due to non-uniform extinction or field coverage) as well as any biases in slit positions on our masks. We assume these biases are independent of redshift, and that they produce the same fractional excess of galaxy counts in all velocity bins. Therefore, the measured values of $\Sigma_v(R)/\Sigma_v^{\rm pred}$ correspond to the the true reduced correlation function $1+w_p(R)$ multiplied by a transverse (angular) selection function, which we estimate by $\Sigma_0(R_k)$.

$$\frac{\Sigma_v(R_k)}{\Sigma_v^{\rm pred}} = \frac{\Sigma_0(R)}{\Sigma_0^{\rm pred}}\left[1+w_p(R_k)\right] \ . \tag{2.11}$$

We found that the measured values of $\Sigma_0(R_k)$ are well-matched by a power-law in R, and therefore, rather than using Eq. 2.11 directly to estimate $w_p(R_k)$, we found best-fit parameters α and β for the following model:

$$\frac{\Sigma_0(R)}{\Sigma_0^{\rm pred}} = \alpha R^{\beta} \ . \tag{2.12}$$

The best-fit parameters for this model are $\alpha = 1.59$, $\beta = -0.58$ with R in h^{-1} cMpc; the fit selection function is displayed in Fig. 2.5. Combining Eqs. 2.10, 2.11, & 2.12, we arrive at an explicit model for $\Sigma_v(R)$ in terms of the galaxy-HLQSO cross-correlation length r_0 and correlation slope γ:

$$\frac{\Sigma_v(R_k)}{\Sigma_v^{\rm pred}} = \alpha R^{\beta}\left[1+\left(\frac{r_0}{R}\right)^{\gamma} {}_2F_1\left(\frac{1}{2},\frac{\gamma}{2};\frac{3}{2};\frac{-z_0^2}{R^2}\right)\right] \tag{2.13}$$

where $z_0 = (1500 \text{ km s}^{-1})H_0^{-1}(1+z)^{-1}$ is the half-width of the redshift window in physical units, and again α and β are set by fitting $\Sigma_0(R)$ to $\Sigma_0(R_k)$. We then adjust the free parameter r_0 corresponding to the cross-correlation function to fit the measured values of $\Sigma_v(R_k)$.

The fit to Σ_v was performed via a simple χ^2-minimization using an error vector constructed assuming Poisson uncertainties in the galaxy counts. The binned data cover a range of projected distances $0.22-3.57h^{-1}$ cMpc.

Our empirical estimate for $w_p(R)$ obtained via the above methods is displayed in Fig. 2.6. We find a best-fit correlation length $r_0 = (7.3 \pm 1.3)h^{-1}$ Mpc after fixing $\gamma = 1.5$, where the error is a 1σ uncertainty computed via a bootstrap estimate. This procedure consisted of repeating the entire analysis 100 times (computation of selection functions, counting of pairs, and χ^2-fitting of w_p) using a random bootstrap sample of 15 of the 15 independent fields selected with replacement. The quoted uncertainty is the standard deviation of parameter values derived from these 100 bootstrap samples. The results of this procedure were consistent with the results of jackknifing estimates performed using 14 of the 15 fields (i.e., an $n-1$ jackknife estimate) or using 8 of the 15 fields (i.e., an approximately $\sim n/2$ jackknife estimate). The χ^2 value for the fit is 3.7 on 4 degrees of freedom.

As noted in §1, Adelberger & Steidel (2005b) performed a cross-correlation measurement with a similar sample of color-selected galaxies to compare black hole and galaxy masses over a large range of AGN luminosities (-20 $\gtrsim$ $\mathrm{M_{AB}}$(1350Å) $\gtrsim$ -30) at a similar range of redshifts to our galaxy sample ($1.5 \lesssim z \lesssim 3.6$). That study separated the AGN sample into two bins of black-hole mass, obtaining galaxy-AGN cross-correlation lengths $r_0 = 5.27^{+1.59}_{-1.36}\ h^{-1}$ cMpc for AGNs with $10^{5.8} < M_{\mathrm{BH}}/\mathrm{M}_\odot < 10^8$ and $r_0 = 5.20^{+1.85}_{-1.16}\ h^{-1}$ cMpc for AGNs with $10^8 < M_{\mathrm{BH}}/\mathrm{M}_\odot < 10^{10.5}$. These measurements are fairly consistent with our own measurement of r_0 for the galaxy-HLQSO cross-correlation, given the size of the uncertainties, and Adelberger & Steidel (2005b) assume a correlation function slope of 1.6, rather than the slope of 1.5 used in this study. As noted above, the best-fit value of r_0 varies inversely with the chosen slope for the range of separations our measurements include, and this effect likely accounts for the slight discrepancy between these two estimates.

2.4.2 Comparison to Galaxy-Galaxy Clustering

The strength of the clustering signal corresponds to the mass scale of the HLQSO-host halos, which we are interested in comparing to the average halo mass scale of non-active galaxies. As such, the relative strengths of the galaxy-galaxy (GG) and galaxy-HLQSO (GQ) clustering reveal the relative mass scales of their respective host halos, and therefore illuminate any halo-mass requirements for the formation of HLQSOs at $z \simeq 2.7$.

Our estimate of the galaxy-galaxy correlation function is based on the same technique as our galaxy-HLQSO estimates but is modified by centering on each galaxy in turn, rather than on the HLQSO. In addition, we restrict our GG analysis to those galaxies at redshifts $z_{\mathrm{gal}} > 2.25$ so that the GG autocorrelation function probes a similar redshift range to that of the GQ cross-correlation; the 909 galaxies with $z > 2.25$ have a median redshift $z_{\mathrm{gal}}^{\mathrm{med}} = 2.63$, while the median HLQSO redshift is $z_{\mathrm{QSO}}^{\mathrm{med}} = 2.66$. For each galaxy in our sample, we consider the number density (per unit solid angle) of galaxies as a function of projected distance from our fiducial galaxy, separating between redshift-associated galaxies (those within 1500 km s^{-1} and in the same

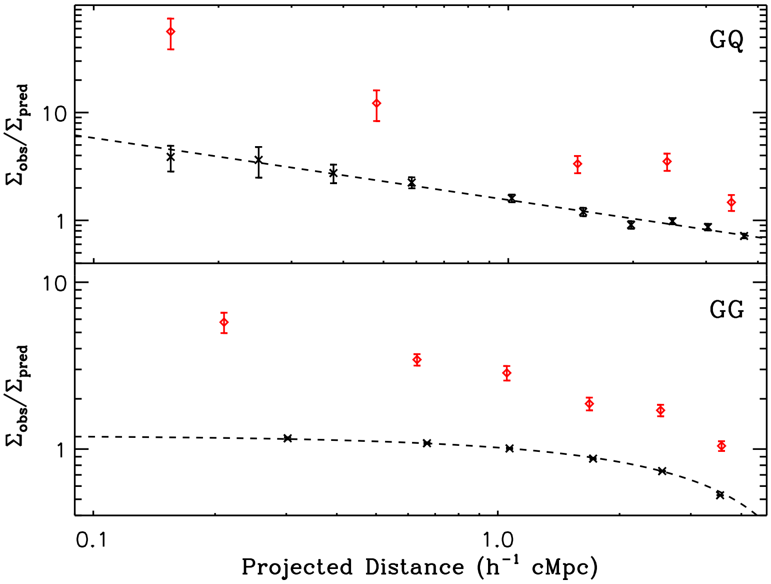

Figure 2.5: The ratio $\Sigma^{\rm obs}/\Sigma^{\rm pred}$ for the galaxy-QSO clustering (GQ; top) and galaxy-galaxy clustering (GG; bottom). In each panel, the red diamonds denote $\Sigma_v^{\rm obs}/\Sigma_v^{\rm pred}$, while the black crosses denote $\Sigma_0^{\rm obs}/\Sigma_0^{\rm pred}$. The error bars are from Poisson uncertainties. The dashed black line is the fit to $\Sigma_0^{\rm obs}/\Sigma_0^{\rm pred}$ and defines the angular selection function; the functional form is a power-law for the GQ selection function (§2.4.1.1) and linear for the GG case (§2.4.2).

field as the fiducial galaxy) and non-associated galaxies (those outside the velocity range or in a different field). We then integrate over the redshift selection function (§2.3.1) to find the expected number of galaxies in each interval, from which we can define an angular correlation function for each interval (by analogy to Eq. 2.11):

$$\frac{\Sigma^{\rm GG}_{v,\rm obs}(R)}{\Sigma^{\rm GG}_{v,\rm pred}} = \frac{\Sigma^{\rm GG}_{0,\rm obs}(R)}{\Sigma^{\rm GG}_{0,\rm pred}}\left[1+w_p^{\rm GG}(R)\right] \tag{2.14}$$

where again the v subscript denotes quantities corresponding to the redshift-associated sample, and the 0 subscript denotes those corresponding to the non-associated sample. The non-associated sample is not expected to cluster about the arbitrary line of sight defined by the position of our fiducial galaxy, so we interpret the quantity $\Sigma_{\rm obs,0}(R)/\Sigma_{\rm pred,0}(R)$ as an estimate of the relative completeness of our angular sampling. We found the completeness (i.e., the angular selection function of the galaxy-galaxy pairs) of our sample to be well-described by a linear model in R with negative slope: $\Sigma_0 = aR+b$. This shape reflects the fact that we are able to measure the power on small scales for essentially all galaxies, while we can see the maximum separation $\simeq 2R_{\rm max}$ only for the small fraction of galaxies at the edge of our fields (and even then we see only the subset of pairs that lie entirely within the field). The best-fit parameter values for the GG angular selection function are $a = -0.160$, $b = 1.04$ with R in h^{-1} cMpc (Fig. 2.5).

As in the case of the GQ cross-correlation function, we then fit a model to $\Sigma_v^{\rm GG}$ that is a combination of the underlying clustering signal described by $w_p^{\rm GG}(R)$ and the selection function described by $\Sigma_0^{\rm GG}$. The

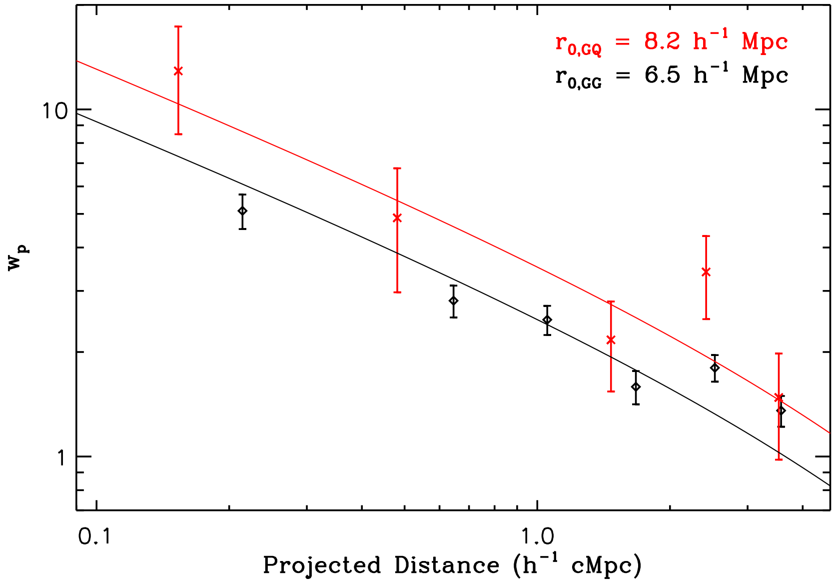

Figure 2.6: Estimate of the reduced galaxy-HLQSO (red) and galaxy-galaxy (black) correlation functions $w_p(R)$ for those galaxies closer than 1500 km s^{-1} from the HLQSO (or fiducial galaxy) redshift. w_p is the excess probability of a galaxy appearing at a projected comoving separation R from the HLQSO line of sight, as compared to predicted galaxy number counts determined by the redshift selection function (§2.3.1) and angular selection function (§2.4.1.1). Solid curves are fits to the best-matched MultiDark halo populations (§2.4.3), which imply a galaxy halo mass $\log(M_{h,gal}/M_\odot) = 11.9\pm0.1$ (see §2.4.4) and a HLQSO halo mass $\log(M_{h,QSO}/M_\odot) = 12.3\pm0.5$.

combined model is given by Eq. 2.15:

$$\frac{\Sigma_v^{GG}(R)}{\Sigma_v^{pred}} = (aR+b)\left[1+\left(\frac{r_0^{GG}}{R}\right)^{\gamma}{}_2F_1\left(\frac{1}{2},\frac{\gamma}{2};\frac{3}{2};\frac{-z_0^2}{R^2}\right)\right].$$

Fitting this model to the measured values of $\Sigma_v^{GG}(R_k)$, we find the best-fit galaxy autocorrelation length to be $r_0^{GG} = (6.0\pm0.5)h^{-1}$ Mpc, again fixing the slope $\gamma = 1.5$. In this case, the errors in Σ_v^{GG} cannot be considered Poissonian because each galaxy is counted in several pairs and the galaxy counts are correlated between bins. However, the 15 HLQSO fields each provide an independent estimate of Σ_v^{GG}, and the error used for the χ^2-fitting is based on the scaled scatter among these values. The quoted error on r_0^{GG} is the 1σ uncertainty from the same bootstrap and jackknife procedures described for r_0^{GQ} (§2.4.1.1). The χ^2 value for the fit is 9.3 on 5 degrees of freedom.

This autocorrelation length is significantly larger than that found by Adelberger et al. (2005b) [$r_0 = (4.0\pm0.6)h^{-1}$ cMpc at $z = 2.9$], despite both studies relying on a similarly-selected set of galaxies. However, this study is restricted to the spectroscopically-observed galaxies, which have a higher mean luminosity than the galaxies in the photometric sample used in Adelberger et al. (2005b), and are more comparable to the higher-luminosity sub-sample of galaxies used in that chapter, for which the authors estimated $r_0 = (5.2\pm0.6)h^{-1}$ cMpc. In addition, the much larger set of spectroscopic redshifts used in our sample allows us to characterize the redshift selection function with much greater accuracy, as well as to restrict our analysis to those galaxies associated with the HLQSOs in three-dimensional space. For example, an injudicious choice of z_0 in Eq. 2.10 would lower the estimated cross-correlation length, either by failing to count HLQSO-associated galaxies ($z_0 < 1500$ km s^{-1}) or by diluting the clustering signal by the inclusion of the voids adjacent to the HLQSO in redshift space ($z_0 > 1500$ km s^{-1}).

2.4.3 Estimate of Halo Mass

The measured clustering of the galaxies in our sample is primarily useful in its connection to the mass scale of the galaxy host halos. Because the clustering strength of dark matter halos is a function of halo mass, we can invert this relation to obtain the halo mass for a population of objects with a given autocorrelation length. In practice, we perform this inversion numerically, finding the population of simulated halos (for which the mass is known) that match the clustering strength of our galaxy sample.

Using halo catalogs from the MultiDark MDR1 simulation (Prada et al. 2011; accessed via the MultiDark Database of Riebe et al. 2011), we measured the correlation length r_0 as a function of minimum halo mass $\mathrm{M_h}$ using the Landy-Szalay estimator (Landy & Szalay 1993) and assuming the same power-law slope (γ = 1.5) used in our fit to the galaxy autocorrelation function. The correlation function was measured for halo populations of differing masses by varying the minimum $\mathrm{M_h}$ in steps of 0.05 dex; the correlation lengths for a subset of the halo samples are listed in Table 2.3. A power-law correlation function is a poor fit to the halo clustering at small scales due to the effect of halo exclusion; therefore, we restricted our fit to pairs with separations $1 \leq d/(h^{-1}\ \mathrm{Mpc}) \leq 5$, a range that avoids the halo-exclusion zone while still closely matching the range of projected distances in our observed sample. In this manner, we find that our galaxy sample is most consistent with having a minimum halo mass $\log(\mathrm{M_h/M_\odot}) > 11.7 \pm 0.1$, the fit to which is displayed in Fig. 2.6. The halos in this mass range have a median mass $\log(\mathrm{M_h/M_\odot}) = 11.9 \pm 0.1$. The statistical error in the mass estimate is entirely due to the propagated error in the autocorrelation function, as the uncertainty in the autocorrelation function among simulated halos is negligible by comparison.

In addition to matching clustering strengths, we can also attempt to match the abundances of observed galaxies and simulated halos. Although our spectroscopic sample of galaxies is incomplete, we can compare this halo population to the galaxy luminosity function (GLF) of Reddy et al. (2008), which corrects for incompleteness in both the spectroscopic and photometric samples. Luminosity functions are measured separately for galaxies with $1.9 \leq z < 2.7$ and $2.7 \leq z < 3.4$, while our sample straddles these two redshift intervals, but the GLF evolves very little over this redshift range, and the predictions of either model are quite similar. Using the Schechter (1976) GLF parameters listed in Table 7 of Reddy et al. (2008), and taking our magnitude limit $\mathcal{R} < 25.5$ to correspond to $\mathrm{M_{AB}(1700Å)} \lesssim -19.9$ at $z \simeq 2.7$, the Reddy et al. models predict a galaxy number density $\phi_{\mathrm{gal}} = 2.4 - 7.0 \times 10^{-3} h^3 \mathrm{Mpc}^{-3}$ (including the 1σ limits on ϕ^*). The number density of $\log(\mathrm{M_h/M_\odot}) > 11.7$ halos in the MultiDark MDR1 simulation is $\phi_{\mathrm{sim}} = 4.4 \times 10^{-3} h^3 \mathrm{Mpc}^{-3}$, entirely consistent with the measured value of ϕ_{gal}.

Taking the population of $\log(\mathrm{M_h/M_\odot}) > 11.7$ halos to represent the host halos of the galaxies in our sample,

Table 2.3. Clustering Properties of Simulated Halos

Minimum $\log(\frac{M_h}{M_\odot})$	ACF r_0[a] (h^{-1} Mpc)	XCF r_0[b] (h^{-1} Mpc)
11.50	5.1	5.6
11.60	5.6	5.9
11.70	6.1	6.1
11.80	6.7	6.3
11.90	7.1	6.8
12.00	7.8	6.8
12.10	8.6	7.2
12.20	9.6	7.6
12.30	10.5	7.8
12.40	11.6	7.9
12.50	12.8	8.4
12.60	14.6	8.6
12.70	16.3	9.0
12.80	18.6	9.1

[a] Halo autocorrelation length (compare to $r_0^{GG} = (6.0\pm0.5)h^{-1}$ cMpc)

[b] Cross-correlation length with halos of mass $\log(M_h/M_\odot)>11.7$ (compare to $r_0^{GQ} = (7.3\pm1.3)h^{-1}$ cMpc)

we then estimate the mass of the HLQSO hosts by finding the population of simulated halos whose cross-correlation with the representative galaxy halos is equal to our measured galaxy-HLQSO cross-correlation function. Again varying the minimum M_h (of fiducial HLQSO hosts) in 0.05 dex increments, and using a Landy-Szalay variant for a cross-correlation with $\gamma = 1.5$, we find that a HLQSO host halo mass $\log(M_h/M_\odot)>12.1\pm0.5$ (a median halo mass of $\log(M_h/M_\odot) = 12.3\pm0.5$) is most consistent with our galaxy-HLQSO cross-correlation measurement. The error in the mass is due to the error on both r_0^{GQ} and the propagated error on the galaxy host halo mass, since the strength of the cross-correlation function depends on the mass of both the HLQSO-host and galaxy-host halo populations. The fit to the corresponding simulated cross-correlation function is shown in Fig. 2.6. The MultiDark halos of $\log(M_h/M_\odot)>12.1\pm0.5$ have an autocorrelation length of 6–15 h^{-1} cMpc, which we consider to be an estimate of the HLQSO autocorrelation length, and such halos have an abundance $\phi_{\rm sim} = (0.17-5.9)\times10^{-3}h^3{\rm Mpc}^{-3}$ at $z\sim2.5$ in the simulation.

2.4.4 Dependence on Simulation Cosmology

The MultiDark suite of simulations used cosmological parameters based on the WMAP 5-year results, $\{\Omega_m,\Omega_\Lambda,\sigma_8,h\} = \{0.27,0.73,0.82,0.70\}$, which are consistent with the most recent WMAP 7-year results from Larson et al. (2011): $\{0.276\pm0.029,0.734\pm0.029,0.801\pm0.030,0.710\pm0.025\}$. In comparison, the older (and widely-utilized) Millennium simulation (Springel et al. 2005) used cosmological parameters based on the WMAP 1-year results, $\{\Omega_m,\Omega_\Lambda,\sigma_8,h\} = \{0.25,0.75,0.9,0.73\}$. We here consider how such a variation in these cosmological parameters affects the halo-matching process employed in this study.

The parameters Ω_m and σ_8 both affect halo abundances, and thus affect the halo bias and the mapping from clustering strengths to halo masses. Zehavi et al. (2011) conduct an HOD analysis on a large sample of galaxies and find that varying the matter density over the range $0.25 \le \Omega_m \le 0.3$ produces only a $\sim$2% variation in their clustering measurements, which is quite small compared to the statistical uncertainty in our measurements.

However, the amplitude of the linear dark-matter fluctuations, σ_8, is tied to the clustering in a more pronounced and complicated manner. The clustering of galaxies in linear theory is given by the galaxy bias and the dark-matter clustering: $\xi_{\rm GG}(M) = b^2(M)\xi_{\rm DM}$. Decreasing σ_8 decreases the value of $\xi_{\rm DM}$ but also greatly decreases the number density of high-mass halos, which causes the bias at a given halo mass $b(M)$ to increase. For high-mass halos, the overall effect is to increase the clustering strength at a given mass when σ_8 is decreased, which suggests that mapping halo masses to clustering strengths using the Millennium simulation would result in a shift toward larger halo masses. Repeating our halo-matching analysis on Millennium halo catalogs, we find that the best-matched halo population of galaxies has a minimum halo mass $\log(\mathrm{M_{h,Mill}/M_\odot})>12.0\pm0.1$ and a median mass $\log(\mathrm{M_{h,Mill}/M_\odot})=12.2\pm0.1$ in that simulation. The discrepancy between the two simulations is $\sim$3x the statistical uncertainty in the galaxy halo mass measurements, confirming that the clustering of these massive halos is quite sensitive to the chosen cosmological parameters.

2.4.5 Relative Abundances of Galaxy-Host and HLQSO-Host Halos

The mass scales of the host halos for galaxies and HLQSOs map to halo abundances, as described in §2.4.3. A galaxy host halo abundance of $\phi_{\rm sim,11.7} = 4.4\times10^{-3}h^3\mathrm{Mpc}^{-3}$ (the MultiDark Simulation abundance of halos with $\log(\mathrm{M_h/M_\odot})>11.7$) and a HLQSO host halo abundance of $\phi_{\rm sim,12.1} = 1.2\times10^{-3}h^3\mathrm{Mpc}^{-3}$ suggest that halos massive enough to host a HLQSO are only $\sim$4x less abundant than those massive enough to host the average galaxy in our sample; the fact that far fewer than one quarter of the galaxies in our sample host a HLQSO is a strong constraint on the duty cycle of these objects. However, the precise value of the HLQSO duty cycle depends on the number density of HLQSOs, which in turn depends on the choice of QSO population.

All of our HLQSOs have luminosities at rest-frame 1450Å of $\log(\nu L_\nu/\mathrm{L_\odot})\sim14$, or an absolute magnitude M(1450Å) ~ -30.[3] This is brighter than the luminosity range for which large-sample statistics are available in surveys such as SDSS and SLAQ [see, e.g., Croom et al. 2009, whose $\mathrm{M_g}(z=2)$ is comparable to M(1450Å)], but we can obtain an estimate of the $z\sim2.7$ quasar luminosity function (QLF) by extrapolating the results of the highest redshift bins of Croom et al. (2009) to slightly higher redshifts and luminosities; in this way we

---

[3] This criterion may not be satisfied for the gravitationally lensed object Q0142-10, and it is possible that other QSOs in our sample are also lensed. However, we regard it as unlikely that significant lensing has remained undetected in these well-studied objects, so the rest-frame luminosities quoted here are assumed to be accurate.

roughly estimate the number density of M(1450Å) $\gtrsim -30$ QSOs to be $\phi_{\rm QSO} \sim 10^{-9.5} h^3$ Mpc^{-3}. Integrating this density over the total comoving volume between redshifts $2 \leq z \leq 3$ predicts $\sim$25 QSOs in this luminosity range over the entire sky, suggesting that a large fraction of the comparably bright QSOs at these redshifts are already in our sample.

Given this number density, we can extract the duty cycle of HLQSOs from the ratio $\phi_{\rm QSO}/\phi_{\rm sim,12.1} \simeq 10^{-6} - 10^{-7}$, defining the duty cycle as the fraction of halos massive enough to host a hyperluminous QSO [log(L/L$_\odot$)$\gtrsim$14] that actually do host such a QSO. This extreme rarity with respect to the number of potential host halos indicates that the formation of the HLQSO must rely on a correspondingly rare event occurring on scales much smaller than those probed by our analysis, perhaps related to an extremely atypical merger or galaxy interaction scenario.

2.4.6 Black Hole Mass vs. Halo Mass

It is interesting to compare the host halo masses of the HLQSOs to the minimum black hole (BH) masses allowed by their luminosities under the assumption of Eddington-limited accretion; we will refer to this minimum mass as M$_{\rm BH}$. The minimum BH masses for each HLQSO are listed in Table 2.2. We calculate the value of M$_{\rm BH}$ directly from L$_{1450}$ (the value of νL_ν at a rest-frame wavelength of 1450Å):

$$M_{\rm BH} = \frac{\sigma_{\rm T} L_{1450}}{4\pi G m_{\rm p} c} = 3.1 \times 10^{-5} \left(\frac{L_{1450}}{L_\odot}\right) {\rm M}_\odot \,. \tag{2.15}$$

We use L$_{1450}$ in place of the bolometric luminosity L$_{\rm bol}$ in order to avoid the additional uncertainty in the bolometric correction. The true bolometric correction is likely to be small: Nemmen & Brotherton (2010) use a thin accretion disc model to predict a correction factor L$_{\rm bol}$/L$_{1450}$ ~ 3, which is consistent with the empirical correction estimated by Netzer & Trakhtenbrot (2007) for L$_{5100}$ and scaled by the L$_{5100}$/L$_{1450}$ relationship of Netzer et al. (2007). However, there is substantial scatter in these corrections, and it may be expected that L$_{\rm bol}$/L$_{1450}$ approaches unity for QSOs selected by the most extreme rest-UV luminosities, so L$_{1450}$ is a useful estimate (and likely a lower limit) on L$_{\rm bol}$.

The HLQSOs in our sample span a range of $\sim$5x in M$_{\rm BH}$ (with the possible exception of Q0142-10), and it is notable that the field (HS1549+1919) with the largest value of M$_{\rm BH}$ is also associated with the largest redshift overdensity in the galaxy distribution (see column N_{1500} in Table 2.2). However, there is no clear relation between N_{1500} and M$_{\rm BH}$ among the other fields, and our galaxy samples are not large enough to comment on the variation of M$_{\rm BH}$ with halo mass.

The median value of M$_{\rm BH}$ for our sample is log(M$_{\rm BH}$/M$_\odot$) $\simeq 9.7$. This indicates that the HLQSO host DM halos are only $\sim$300-2000x more massive than their associated supermassive BHs, even assuming accretion at the Eddington limit. The relationship between BH mass and DM halo mass is uncertain even at $z \simeq 0$ (compare, e.g., Ferrarese 2002, Booth & Schaye 2010, and Kormendy & Bender 2011), but these BHs lie well above the predictions of the M$_{\rm BH}$-σ or M$_{\rm BH}$-v_c relations for any reasonable mapping of the DM halo mass to the bulge velocity dispersion σ or circular velocity v_c, as demonstrated below.

Three such mappings are considered in Ferrarese (2002), in which the halo virial velocity $v_{\rm vir}$ is related to the circular velocity by considering $v_c = v_{\rm vir}$ (a zeroth-order approximation), $v_c = 1.8 v_{\rm vir}$ (based on observational constraints on DM halo mass profiles by Seljak 2002), or $v_c/v_{\rm vir}$ given by a function of halo mass extracted from the N-body simulations of Bullock et al. (2001). These three different assumptions predict BH masses of $\log(\mathrm{M_{BH}/M_\odot}) = 7.0$, 8.4, and 7.5, respectively, for a halo of mass $\log(\mathrm{M_h/M_\odot}) = 12.3$, corresponding to $\mathrm{M_{DM}/M_{BH}} \simeq 2 \times 10^5$, 8×10^3, and 6×10^4. In any of these cases, the minimum BH masses for the HLQSOs in our sample are 1-2 orders of magnitude higher than the predictions of the low-redshift associations, implying that the host halos must “catch up” with the BHs in order to fall on the established relations by $z \simeq 0$.

Though estimates of BH masses at high redshift are highly uncertain, as are the stellar masses of their host galaxies, this result agrees qualitatively with several observational studies that find BH host galaxies at high redshift ($1 \lesssim z \lesssim 4$) of a given stellar mass have systematically higher BH masses than in the local universe (e.g. Peng et al. 2006; Decarli et al. 2010; Merloni et al. 2010; Greene et al. 2010); Booth & Schaye (2010, 2011) describe an interpretation of this evolution in terms of the compactness of DM halos, which are more tightly bound at high redshifts. These studies generally find a smaller deviation from the $z \simeq 0$ relations than is present in our sample, but the extreme luminosities of the HLQSOs in our sample force us to probe the highest-mass end of the BH mass distribution, so our measurements are very sensitive to the scatter in the $\mathrm{M_h}$–$\mathrm{M_{BH}}$ relation as well as to evolution in the mean.

If we consider the possibility that the dynamical mass discussed in §2.5 includes matter external to the HLQSO host halo at $z \simeq 2.7$, which may merge into a single more massive halo by $z \simeq 0$, we can calculate where such a halo would fall in the $\mathrm{M_h}$–$\mathrm{M_{BH}}$ relations of Ferrarese (2002). Taking a halo mass $\log(\mathrm{M_h/M_\odot}) = 13$, the above prescriptions predict BH masses of $\log(\mathrm{M_{BH}/M_\odot}) = 8.3$, 9.6 and 8.7, respectively, which lie much closer to the range of BH masses seen in our sample. However, it seems clear that the extremely high BH masses indicate that the HLQSOs are atypical (with respect to the general population of QSOs) at the smallest scales.

2.5 Group-Sized HLQSO Environments

In addition to the properties of the HLQSO host halos themselves, it is interesting to consider the type of larger environment these hyperluminous objects inhabit. The spatial scale of the galaxy overdensities occupied by the HLQSOs in our sample is $\sim 0.5 h^{-1}$ cMpc (Fig. 2.4; $\sim$200 pkpc), and the peculiar velocity scale of the composite overdensity is $\sigma_{\rm v,pec} \simeq 200$ km s^{-1} after accounting for our measurement errors (Fig. 2.1). The relatively compact nature of the overdensity suggests that it may represent a virialized structure (discussed below), in which case the inferred size and velocity scales can be combined to provide a crude estimate of the mass scale of the overdensity. The virial mass estimator can be expressed in terms of the 3D velocity dispersion $\langle \mathbf{v}^2 \rangle$, a characteristic radius R, the gravitational constant G, and a constant $\alpha \sim 1$ that depends on the geometry of the system:

$$M_{\rm dyn} = \alpha R \langle \mathbf{v}^2 \rangle / G\,. \tag{2.16}$$

If we approximate our group as a sphere of uniform density, we have $\alpha = 5/3$. We can also take $\langle \mathbf{v}^2 \rangle = \langle v_{\rm x}^2 \rangle + \langle v_{\rm y}^2 \rangle + \langle v_{\rm z}^2 \rangle = 3\sigma_v^2 \simeq 3 \times (200\ {\rm km\ s^{-1}})^2$ and $R \simeq 200$ pkpc from the scales above, from which we find that the average HLQSO overdensity is associated with a total mass $\log({\rm M_{dyn}/M_\odot}) \simeq 13$ — the approximate mass scale of a small galaxy group, and consistent with the HLQSO host halo mass derived from the clustering analysis in §2.4.3.

Because of the crude nature of this estimate, we considered several checks to determine whether these overdensities are indeed consistent with virialized groups. If the galaxies around the HLQSOs are in virial equilibrium, their spatial extent should roughly match the virial radius r_{200} of a $\log({\rm M_h/M_\odot}) \simeq 13$ halo, where $r_{200} = (3M_{\rm grp}/800\pi\rho_{\rm crit})^{1/3}$. In fact, the virial radius for this mass scale is approximately $r_{200} \simeq 200$ pkpc $\simeq 0.5h^{-1}$ cMpc — this close match to the observed overdensity scale suggests that the HLQSO-associated galaxy overdensities are indeed virialized.

Finally, we can estimate the number of galaxies associated with each HLQSO. From our smoothed selection function (§2.3.1), we find that the approximate number density of spectroscopically-observed galaxies at $z \sim 2.7$ is $\phi_{\rm spec} = 1.3 \times 10^{-3} h^3 {\rm Mpc}^{-3}$, while the number density of $\log({\rm M_h/M_\odot}) > 11.7$ halos in the MultiDark simulation is $\phi_{\rm sim} = 4.4 \times 10^{-3} h^3 {\rm Mpc}^{-3}$ (which is also the abundance of galaxies predicted by the GLF of Reddy et al. 2008). Under the assumption that each of these $\log({\rm M_h/M_\odot}) > 11.7$ dark matter halos hosts a galaxy of comparable luminosity to those in our sample (§2.4.3), this implies that our spectroscopic sample is $\sim$30% complete. We find a total of 15 galaxies in our sample that are within 1500 km s^{-1} and $0.5h^{-1}$ projected cMpc of a HLQSO; taking our completeness into account, we expect that there are another ~ 35 galaxies remaning unobserved in this volume. On average, therefore, each of the 15 HLQSOs in our sample has $\sim$3 other $\log({\rm M_h/M_\odot}) \simeq 12$ galaxies within 200 pkpc, again suggesting a group-sized environment.

Note that we use the term "environment" here to connote a region that may or may not correspond to the host halo of the HLQSO. The mass we derive here is slightly larger than the average HLQSO host halo mass of $\log({\rm M_{h,QSO}/M_\odot}) = 12.3 \pm 0.5$ derived from our clustering analysis (§2.4.3), and the galaxies associated with the HLQSO overdensity extend to greater projected radii than the $\sim$130 pkpc virial radius of such a halo (Fig. 2.4). The discrepancy in the mass estimate may be due to larger-than-assumed errors in the HLQSO redshifts, as noted in §2.3.3; overestimation of the galaxy velocity dispersion would inflate the dynamical mass estimate of the system. However, it may also be that the HLQSO host and its galaxy neighbors are subhalos within a larger structure corresponding to our measured dynamical mass.

In addition, we note that the velocity scale of 200–300 km s^{-1} and the overdensity of galaxies in such an environment are extremely conducive to mergers and dissipative interactions among galaxies. We suggest that the results of this study are thus strong evidence that the fueling of these HLQSOs is associated with merger activity, with the caveat that our sample of HLQSOs are extreme outliers in the QSO luminosity distribution, and thus may be formed and sustained by rather different mechanisms than the average QSO at these redshifts.

2.6 Summary

We have used a large sample of galaxy redshifts to investigate the environments of 15 hyperluminous QSOs (HLQSOs) in the redshift range $2.5 < z < 2.9$. Our galaxy sample includes 1558 spectroscopic redshifts between $z = 1.5 - 3.6$ from the KBSS—we use the galaxies far from the HLQSOs to characterize our redshift selection function in much greater detail than is possible with purely photometric samples. Furthermore, all the redshifts in our sample are projected within $\sim 3'$ of one of the HLQSOs, which allows us to describe the HLQSO environments on sub-Mpc scales. The principal conclusions of this work are given here:

1. The HLQSOs are associated with a $\delta \sim 7$ overdensity in redshift when considered on scales of $\sim 5h^{-1}$ Mpc. The overdensity has a velocity scale of $\sigma_{\mathrm{v,pec}} \simeq 200$ km s^{-1} after subracting the effect of redshift errors, and a projected scale of $R \sim 200$ pkpc. When stacked at the redshifts of the HLQSOs, the combined galaxy distribution shows no peaks of similar significance, and stacking on random galaxy redshifts shows that the HLQSOs are correlated with much more significant small-scale overdensities than the average galaxy in our sample.

2. Careful treatment of the HLQSO redshifts is essential in order to accurately determine which galaxies are associated with the HLQSOs in three-dimensional space. When available, we used a combination of low-ionization broad lines, narrow emission lines, and the onset of the Ly-α forest in the HLQSO spectra themselves in conjunction with narrow Ly-α at small angular separations from the HLQSOs to obtain HLQSO redshifts offset by hundreds or thousands of km s^{-1} from their previously published values. The velocity scale of the observed overdensity, which is smaller than the measured offset for any one of these HLQSOs, demonstrates both the accuracy of our redshifts and the inadequacy of common techniques for estimating the redshifts of these hyperluminous objects.

3. The best-fit autocorrelation function for the subset of galaxies in our sample with $z > 2.25$ ($z_{\mathrm{med}} \simeq 2.63$) has a correlation length $r_0^{\mathrm{GG}} = (6.0 \pm 0.5)h^{-1}$ cMpc. Comparison to dark-matter halo catalogs from the MultiDark simulation suggests that the galaxies in our sample have a minimum halo mass of $\log(\mathrm{M_h/M_\odot}) > 11.7 \pm 0.1$ and a median halo mass of $\log(\mathrm{M_{h,med}/M_\odot}) = 11.9 \pm 0.1$.

4. The best-fit galaxy-HLQSO correlation function for our sample has a correlation length $r_0^{\mathrm{GQ}} = (7.3 \pm 1.3)h^{-1}$ cMpc. By measuring the clustering between dark matter halos of various masses and those halos having masses $\log(\mathrm{M_h/M_\odot}) > 11.7$, we find that the cross-correlation between $\log(\mathrm{M_h/M_\odot}) > 11.7$

halos and $\log(M_h/M_\odot)>12.1$ halos most closely matches our observed value of r_0^{GQ}. We therefore deduce that each HLQSO in our sample inhabits a dark matter halo with mass $\log(M_h/M_\odot)>12.1\pm0.5$, which corresponds to a median halo mass of $\log(M_{h,med}/M_\odot) = 12.3\pm0.5$. The number density of these halos exceeds the number density of HLQSOs by a factor $\sim10^6-10^7$.

5. The HLQSO luminosities imply minimum masses $\log(M_{BH}/M_\odot) \gtrsim 9.7$, suggesting a BH-DM mass ratio $M_{DM}/M_{BH} \lesssim 300$–$2000$ for a dark matter mass $\log(M_{DM}/msun) \simeq 12.3$–$13$. Such a small ratio indicates that the HLQSOs are significantly overmassive with respect to the M_{BH}–M_h relation at $z \simeq 0$, and appear overmassive with respect to equivalent relations at higher redshift (though black hole mass estimates are quite uncertain at high redshifts).

6. The HLQSOs in our sample are associated with group-sized environments with total mass $\log(M_{grp}/M_\odot)\sim13$. This conclusion follows from a dynamical mass estimate from the peculiar velocities and projected scale of the galaxy overdensity, and is consistent with the virial radius and galaxy counts expected for such a group. The peculiar velocities and overdensities associated with groups strongly indicates that these HLQSOs inhabit environments where mergers and dissipative interactions are common.

In conclusion, the results of this chapter demonstrate that the host halos of HLQSOs are not rare, so the scarcity of these objects is likely due to an extremely improbable small-scale phenomenon that produces HLQSOs. Such a phenomenon could be related to an atypical galaxy interaction geometry or similar scenario: the overdense environment with small relative velocities would increase the probability of such an event, but an unusual merger configuration is likely required to generate such large black hole masses and QSO luminosities.

We thank our collaborators for their important contributions to the Keck Baryonic Structure Survey over the course of many years: M. Bogosavljevic, D. Erb, D.R. Law, M. Pettini, O. Rakic, N. Reddy, G. Rudie, and A. Shapley. Thanks also to C. Bilinski for his help reducing some of the TripleSpec QSO spectra. RFT would also like to thank B. Siana, N. Konidaris, A. Benson, C. Hirata, R. Quadri, and J.R. Gauthier for many useful discussions. We are grateful for the many useful comments we received from an anonymous referee, particularly in regard to the estimation of uncertainties in the correlation function parameters. The MultiDark Database used in this chapter and the web application providing online access to it were constructed as part of the activities of the German Astrophysical Virtual Observatory as the result of a collaboration between the Leibniz-Institute for Astrophysics Potsdam (AIP) and the Spanish MultiDark Consolider Project CSD2009-00064. The MultiDark simulation was run on the NASA's Pleiades supercomputer at the NASA Ames Research Center. The Millennium Simulation databases used in this chapter and the web application providing online access to them were constructed as part of the activities of the German Astrophysical Virtual Observatory. We are indebted to the staff of the W.M. Keck Observatory who keep the instruments and telescopes running effectively. We also wish to extend thanks to those of Hawaiian ancestry on whose sacred mountain we are privileged to be guests. This work has been supported by the US National Science Foundation through grants AST-0606912 and AST-0908805. CCS acknowledges additional support from the John D. and Catherine T. MacArthur Foundation and the Peter and Patricia Gruber Foundation.

Chapter 3

Constraints on Hyperluminous QSO Lifetimes via Fluorescent Lyα Emitters at $Z \simeq 2.7$

This chapter was previously published as Trainor & Steidel 2013, ApJ, 775, L3.

Abstract

We present observations of a population of Lyα emitters (LAEs) exhibiting fluorescent emission via the reprocessing of ionizing radiation from nearby hyperluminous QSOs. These LAEs are part of a survey at redshifts $2.5 < z < 2.9$ combining narrowband photometric selection and spectroscopic follow-up to characterize the emission mechanisms, physical properties, and three-dimensional locations of the emitters with respect to their nearby hyperluminous QSOs. These data allow us to probe the radiation field, and thus the radiative history, of the QSOs, and we determine that most of the 8 QSOs in our sample have been active and of comparable luminosity for a time 1 Myr $\lesssim t_{\rm Q} \lesssim$ 20 Myr. Furthermore, we find that the ionizing QSO emission must have an opening angle $\theta \sim 30^\circ$ or larger relative to the line of sight.

3.1 Introduction

The extreme luminosities of QSOs make them effective tracers of black hole growth over most of the Universe's history ($0 < z \lesssim 7$) and likewise illuminate the evolution of galaxies and large-scale structure over these cosmological epochs and volumes. In particular, the mass of supermassive black holes is tightly correlated with properties of their host galaxies (e.g. Magorrian et al. 1998; Gebhardt et al. 2000; Ferrarese & Merritt 2000), while QSO clustering properties are well-matched to the expected distribution of dark matter in and out of halos (e.g. Seljak 2000; Berlind & Weinberg 2002; Zehavi et al. 2004) according to the cosmological standard model.

However, the manner in which QSOs populate and interact with galaxies and dark-matter halos is obscured by the unknown timescales and geometries over which black holes accrete mass and produce substantial radiation. Specifically, the fraction of black holes that can be observed as QSOs depends sensitively on the length of their active phases and whether their emission is isotropic or confined to a narrow solid angle. A short QSO lifetime ($t_{\rm Q}$) and/or a small opening angle ($\theta_{\rm Q}$) would indicate that observed QSOs comprise a small fraction of the total population of black holes (and therefore galaxies and dark-matter halos) that will pass through a QSO phase. Furthermore, both the comparison of $t_{\rm Q}$ to a typical star-formation timescale $t_{\rm SF} \sim 100$ Myr and the value of $\theta_{\rm Q}$ have deep implications for the mechanisms by which the QSO couples to the ISM in galaxies and produces feedback.

Current estimates of $t_{\rm Q}$ utilize numerous methods, many of which are described in detail in a review by Martini (2004), and in general allow for QSO lifetimes in the range 10^6 yr $< t_{\rm Q} < 10^8$ yr. In the last decade, measurements of the QSO luminosity function and clustering have provided particularly powerful constraints on a globally-averaged $t_{\rm Q}$ (e.g. Kelly et al. 2010), but they also rely on the poorly-constrained black hole mass function or assume that the most luminous QSOs populate the most massive halos, contrary to some observations and physically-motivated models (e.g. Trainor & Steidel 2012; Adelberger & Steidel 2005a; Conroy & White 2013). These global measures of $t_{\rm Q}$ are also degenerate between single-phase QSO accretion (in which the bulk of activity occurs in a single event) and multi-burst models (in which the same total time in a QSO phase is distributed over many short accretion events).

More direct measurements of $t_{\rm Q}$ may be obtained from the effect of QSO radiation on their local environments. Measures of the transverse proximity effect use the volumes (and associated light-travel times) over which bright QSOs ionize their nearby gas and have yielded estimates or lower limits in the range $t_{\rm Q} \sim 16-40$ Myr by tracing He II (e.g. Jakobsen et al. 2003; Worseck et al. 2007) and metal-line (Gonçalves et al. 2008) absorption systems.

The detection of fluorescent Lyα emission provides another direct measurement of $t_{\rm Q}$. Fluorescent Lyα arises from the reprocessing of ionizing photons (either from the metagalactic UV background or a local QSO) at the surfaces of dense, neutral clouds of H I. This effect has been modeled with increasing complexity over the last few decades (Hogan & Weymann 1987; Gould & Weinberg 1996; Cantalupo et al. 2005; Kollmeier et al. 2010) and has now been observed around bright QSOs (Adelberger et al. 2006; Cantalupo et al. 2007, 2012; Trainor et al. 2013, in prep.). These detections have verified the feasibility of identifying fluorescent emission from the intergalactic medium (IGM) and suggested a wide opening angle $\theta_{\rm Q}$ of QSO emission (but see also Hennawi & Prochaska 2013). They are consistent with other constraints on $t_{\rm Q}$, but have been limited by small sample sizes and/or a lack of the 3D spatial information necessary to probe the spatial variation of the QSO radiation field in detail.

This chapter presents results from a large survey of Lyα emitters (LAEs) in fields surrounding hyperluminous ($L_{\rm UV} \sim 10^{14}$ L$_\odot$) QSOs at redshifts $2.5 < z < 2.9$. The full results of this survey, including a detailed analysis of the Lyα emission mechanisms and physical properties of the LAEs, will be presented in Trainor et al. (2014, in prep.) and in Chapter 4. This chapter focuses on the implications of these data for $t_{\rm Q}$ and $\theta_{\rm Q}$. Observations and the data are briefly discussed in §3.2; identification of fluorescent sources is discussed in §3.3.1; constraints on $t_{\rm Q}$ and $\theta_{\rm Q}$ appear in §3.3.2–§3.3.5; and conclusions are given in §3.4. A standard cosmology with $H_0 = 70$ km s^{-1} and $\{\Omega_{\rm m}, \Omega_\Lambda\} = \{0.3, 0.7\}$ is assumed throughout, and distances are given in physical units (e.g. pMpc).

3.2 Observations

We conducted deep imaging in each survey field using custom narrowband filters and corresponding broadband filters sampling the continuum near Lyα with Keck 1/LRIS-B over several years; these data are described in Chapter 4. All eight fields are part of the Keck Baryonic Structure Survey (KBSS; Rudie et al. 2012; Steidel et al. 2013, in prep.)

We used one of four narrowband filters to image each of the eight QSO fields (centered on or near the QSO); a brief description of the fields and corresponding filters is given in Table 3.1. Each filter has a FWHM ~ 80Å and a central wavelength tuned to Lyα at the redshift of one or more of the hyperluminous QSOs. The QSOs span a redshift range $2.573 \leq z \leq 2.843$, and the filter width corresponds to $\Delta z \approx 0.066$ or $\Delta v \approx 5400$ km s^{-1} at their median redshift. The narrowband images have total integration times of 5-7 hours and reach a depth for point sources of $m_{\rm NB}(3\sigma) \sim 26.7$; the continuum images are typically deeper by ~ 1.5 mag.

Object identification and narrowband and continuum magnitude measurements were performed with SExtractor. The success rate of our initial follow-up spectroscopy dropped sharply above $m_{\rm NB} = 26.5$, so our LAEs are selected to have $20 < m_{\rm NB} < 26.5$ and $m_{\rm cont} - m_{\rm NB} > 0.6$ (corresponding to a rest-frame equivalent width in Lyα $W_{\rm Ly\alpha} \gtrsim 20$Å). These criteria define a set of 841 LAEs. The LAEs range from unresolved/compact to extremely extended (FWHM $\gtrsim 10''$) sources. The extended objects require large photometric apertures that may enclose unassociated continuum sources; in order to avoid the complication of determining the true continuum counterparts of these sources, LAEs with FWHM $> 3''$ were removed from our sample for this analysis, leaving a final photometric sample of 816 LAEs.

Spectra were obtained with Keck 1/LRIS-B in the multislit mode using the 600/4000 grism; the spectral

Table 3.1. Lyα-Emitter Field Descriptions

QSO Field	z_Q	NB Filter	N_{phot}	N_{spec}	$N_{W_{\mathrm{Ly}\alpha}>100\mathrm{Å}}$
Q0100+13 (PHL957)	2.721 ± 0.001	NB4535	79	20	9
HS0105+1619	2.652 ± 0.001	NB4430	109	23	6
Q0142–10 (UM673a)	2.743 ± 0.001	NB4535	58	25	11
Q1009+29 (CSO 38)	2.652 ± 0.001	NB4430	60	35	13
HS1442+2931	2.660 ± 0.001	NB4430	120	39	23
HS1549+1919	2.843 ± 0.001	NB4670	202	95	27
HS1700+6416	2.751 ± 0.001	NB4535	66	23	11
Q2343+12	2.573 ± 0.001	NB4325	122	0[a]	16

[a] Spectroscopic follow-up observations of field Q2343+12 had not been obtained at the time of this publication.

resolution near Lyα for these spectra is $R \sim 1200$. Redshifts were measured via an automated algorithm described in Chapter 4; the detected Lyα lines have a minimum SNR $\sim$ 3.5 and a median SNR $\sim$ 15. Detected lines were required to lie at a wavelength where the transmission exceeds 10% for the narrowband filter used to select their associated candidates (typically a ~110Å range), but no other prior was used to constrain the automatic line detection. Redshifts were measured for 260 of the LAEs meeting our final photometric criteria; these comprise the spectroscopic sample used in this chapter. QSO redshifts were determined as described in Trainor & Steidel (2012) and have estimated uncertainties $\sigma_{z,\mathrm{QSO}} \approx 270$ km s^{-1}.

3.3 Results

3.3.1 Detection of Fluorescent Emission

Lyα emission is subject to complex radiative-transfer effects and is ubiquitous in star-forming galaxies, so accurate discrimination between fluorescence and other Lyα emission mechanisms is key to its use as a QSO probe (see Cantalupo et al. 2005; Kollmeier et al. 2010). A powerful tool in this regard is the rest-frame equivalent width of Lyα ($W_{\mathrm{Ly}\alpha}$), which has a natural maximum in star-forming sources because the same massive stars produce the UV continuum and the ionizing photons that are reprocessed as Lyα emission. Empirically, UV-continuum-selected galaxies at $2 \lesssim z \lesssim 3$ almost never exhibit $W_{\mathrm{Ly}\alpha} > 100$Å (Kornei et al. 2010), which is also the maximum value expected for continuous star-formation lasting $\sim 10^8$ yr or longer (Steidel et al. 2011). This threshold may demarcate the realm of fluorescence from that of typical star-forming galaxies. Furthermore, models of star-formation in the extreme limits of metallicity and short bursts predict a stringent limit of $W_{\mathrm{Ly}\alpha} < 240$ Å (see Schaerer 2002 and discussion in Cantalupo et al. 2012) for even the most atypical star-forming galaxies.

The distribution of $W_{\mathrm{Ly}\alpha}$ and m_{NB} for the LAEs are displayed in Fig. 3.1. Observed-frame equivalent

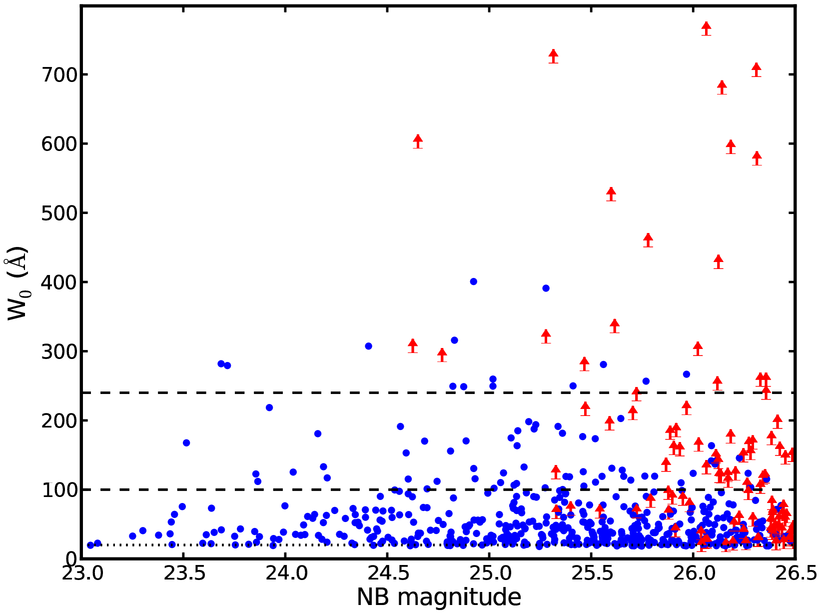

Figure 3.1: The rest-frame equivalent width ($W_{\rm Ly\alpha}$) of Lyα determined from the measured $m_{\rm cont} - m_{\rm NB}$ color for each LAE in our photometric sample. Objects detected in the continuum band are displayed as blue circles, while objects consistent with having no continuum flux (after subtracting the measured Lyα flux) are displayed as red arrows denoting 1σ lower limits. Thresholds for the maximum value of $W_{0,Ly\alpha}$ consistent with typical and extremely brief star-formation are plotted as dashed lines at $W_{\rm Ly\alpha}$ = 100Å and $W_{\rm Ly\alpha}$ = 240Å, respectively (see §3.3.1 for details). The dotted line at $W_{\rm Ly\alpha}$ = 20Å denotes the minimum Lyα equivalent width for a LAE.

widths (W) were measured from the narrowband color excess while accounting for the presence of Lyα within the continuum filter bandpass; details of this procedure are given in Chapter 4. $W_{\rm Ly\alpha}$ is estimated from W by $W_{\rm Ly\alpha} = W/(1+z_{\rm QSO})$, where $z_{\rm QSO}$ is the redshift of the associated hyperluminous QSO.

Fig. 3.1 demonstrates that many of our LAEs exceed both the model and empirical thresholds for the maximum $W_{\rm Ly\alpha}$ consistent with pure star formation: of the 816 LAEs, 116 exceed $W_{\rm Ly\alpha} > 100$Å and 32 exceed $W_{\rm Ly\alpha} > 240$Å. We consider these high-$W_{\rm Ly\alpha}$ sources as excellent candidates to be fluorescence-dominated, with minimal stellar contribution to their Lyα flux.

3.3.2 Time delay of fluorescent emission

The presence of a fluorescent emitter indicates that its local volume element was illuminated by ionizing QSO radiation at the lookback time $t_{\rm Ly\alpha}$ when the observed Lyα photon was emitted. Depending on whether the fluorescent source lies in the foreground or background of the QSO, $t_{\rm Ly\alpha}$ may be greater or less than $t_{\rm QSO}$, the lookback time to the QSO itself.

However, this fluorescent Lyα photon was generated by the reprocessing of an ionizing QSO photon emitted a time $t_{\rm lt}$ before $t_{\rm Ly\alpha}$, where $t_{\rm lt}$ is the light-travel time from the QSO to the emitter. It is geometrically trivial to show that $t_{\rm QSO} \leq t_{\rm Ly\alpha} + t_{\rm lt}$, and we can define the delay time for an emitter at a vector position $\mathbf{r}$:

$$t_{\rm delay}(\mathbf{r}) = t_{\rm Ly\alpha}(\mathbf{r}) + t_{\rm lt}(\mathbf{r}) - t_{\rm QSO} \ . \tag{3.1}$$

It can likewise be shown that the locus of points for which $t_{\rm delay}$ is constant forms a paraboloid pointed toward the observer with the QSO at the focal point (see Fig. 3.2, top, for a pictorial representation at varying values of $t_{\rm delay}$).

The significance of such a delay surface can be seen by considering a simple, step-function model of QSO emission in which the ionizing emission was zero a time $t_{\rm Q}$ before we observe the QSO and has been constant since that time. Under such a model, the ionizing field is zero for $t_{\rm delay}(\mathbf{r}) > t_{\rm Q}$, and the spatial distribution of fluorescent emitters must be restricted to the interior of the paraboloid defined by $t_{\rm delay}(\mathbf{r}) = t_{\rm Q}$.

Since the high-$W_{\rm Ly\alpha}$ LAEs described in §3.3.1 are highly likely to be dominated by fluorescence, they represent the best tracers of the QSO ionizing field. Below, we use the distribution of these sources to set limits on $t_{\rm Q}$.

3.3.3 Constraints on $t_{\rm Q}$ from the redshift distribution

The geometry of our survey volume is such that we can probe long timescales (10^7 yr $\lesssim t_{\rm Q} \lesssim 10^8$ yr) via the line-of-sight distribution of sources (see red box in Fig. 3.2, top). The distribution of $W_{\rm Ly\alpha}$ vs. $d_{\rm z}$ for the 260 LAEs with measured redshifts is displayed in Fig. 3.2 (middle), where $d_{\rm z}$ is the Hubble distance of each emitter from its associated hyperluminous QSO determined from the difference of emitter and QSO redshifts.

Due to the effects of redshifts errors and peculiar velocities among the LAEs and QSOs, our foreground/background discrimination breaks down at $\Delta v \approx 700$ km s^{-1}, corresponding to $d_{\rm z} \lesssim 3$ pMpc and $t_{\rm delay} \lesssim 20$ Myr; we are therefore unable to constrain $t_{\rm Q}$ lower than 20 Myr based on the redshift distribution of sources. At $t_{\rm delay} > 20$ Myr, however, there is a significant paucity of high-$W_{\rm Ly\alpha}$ sources: only four sources with $W_{\rm Ly\alpha} > 100$Å lie in this range, and there are none at $t_{\rm delay} > 33$ Myr. This suggests $t_{\rm Q} \lesssim 20$ Myr for these fields; we evaluate the significance of this result via numerical tests below.

The non-uniform redshift coverage of our QSO fields complicates the analysis of $d_{\rm z}$; the observed redshift distribution is modulated by the narrowband filter bandpass and the distribution of large-scale structure along the QSO line of sight. In addition, the QSO redshifts are not perfectly centered in their filter bandpasses, which contributes part of the observed asymmetry. Fortunately, the distribution of star-forming galaxies presumably represented by our $W_{\rm Ly\alpha} < 100$Å LAEs trace all of these effects, and we can use their redshift distribution to determine the expected distribution of emitters in the absence of fluorescence. We use the entire sample of emitters with spectroscopic redshifts and $W_{\rm Ly\alpha} < 100$Å for this comparison.

First, we utilize the two-sample Kolmogorov-Smirnov (KS) test, a measure of the probability that two samples of observations are drawn from the same parent distribution. Evaluating the test on the distributions of $d_{\rm z}(W_{\rm Ly\alpha} > 100$Å$)$ and $d_{\rm z}(W_{\rm Ly\alpha} \leq 100$Å$)$ yields a KS statistic $M_{\rm KS} = 0.234$, corresponding to $p < 4 \times 10^{-3}$.

There are insufficient emitters with redshift measurements to perform the test on the higher-threshold ($W_{\mathrm{Ly}\alpha} >$ 240Å) sample with significance.

A disadvantage of the two-sample KS test is that it is most sensitive to differences that occur near the center of two distributions, whereas we expect the strongest deviation in these distributions at large d_z, where no fluorescent emitters would appear if $t_Q \lesssim 20$ Myr. For this reason, we conducted a Monte-Carlo test in which subsamples of the $W_{\mathrm{Ly}\alpha} < 100$Å LAEs were randomly selected (with replacement), where each subsample has 67 objects, the number of $W_{\mathrm{Ly}\alpha} > 100$Å emitters with spectroscopic redshifts in our actual sample. For each subsample, the number of sources with $d_z > 3$ pMpc (corresponding to $t_{\mathrm{delay}} \gtrsim 20$ Myr) was counted.

As noted above, only four sources with $W_{\mathrm{Ly}\alpha} > 100$Å exceed $d_z = 3$ pMpc. In 10^5 simulated subsamples, 40 had three or fewer objects with $d_z > 3$ pMpc, yielding a significance $p < 4 \times 10^{-4}$. We therefore conclude that the 7 QSOs with spectroscopic follow-up (i.e., all except Q2343+12) are consistent with $t_Q \lesssim 20$ Myr (approximately the lowest it can be measured unambiguously from our redshift measurements).

3.3.4 Constraints on t_Q from the projected distribution

While the redshift distribution is not sensitive for probing shorter QSO lifetimes, sufficiently small values of t_Q will affect the projected distribution of sources in the survey volume. In particular, the constant-t_{delay} paraboloids for $t_{\mathrm{delay}} \lesssim 1$ Myr are well matched to the geometry of our survey volume (see curves on the left side of Fig. 3.2, top).

Fig. 3.3 shows the correspondence of these surfaces (shown for 10^4 yr $\leq t_{\mathrm{delay}} \leq 10^6$ yr) to the radial distribution of $W_{\mathrm{Ly}\alpha}$ for the entire photometric sample (note that the survey geometry is not to scale, unlike in Fig. 3.2). As above, a QSO with $t_Q \leq t_{\mathrm{delay}}$ will produce fluorescent emission only within the corresponding paraboloid. For $t_Q < 0.3$ Myr, this would produce a maximum projected distance (d_θ) at which a fluorescent emitter could appear in our survey volume. For 0.3 Myr $\leq t_Q \leq$ 1 Myr, the fractional volume of the survey within the time-delay surface decreases with increasing d_θ, predicting that the probability of a given emitter exhibiting fluorescence will likewise decrease with d_θ. [1]

Notably, the projected distribution of LAEs is well-populated by objects with $W_{\mathrm{Ly}\alpha} > 100$Å and those with $W_{\mathrm{Ly}\alpha} > 240$Å out to the largest values of d_θ probed by our survey, thus firmly ruling out lifetimes $t_Q < 0.3$ Myr. Furthermore, the radial distributions of sources with $W_{\mathrm{Ly}\alpha} > 100$Å and $W_{\mathrm{Ly}\alpha} \leq 100$Å are entirely consistent when subjected to a two sample KS test ($M_{\mathrm{KS}} = 0.095$; $p < 0.24$); the null result is similar using the $W_{\mathrm{Ly}\alpha} = 240$Å threshold. Given the large number of objects in our photometric sample ($N_{\mathrm{phot}} = 816$), these data provide strong evidence that $t_Q \gtrsim 1$ Myr for the QSOs in our sample.

---

[1] The probability of being fluorescence-dominated will also vary with distance due to the fall-off of the QSO ionizing radiation field, but the effect on a flux-limited sample depends on the size distribution of fluorescently-emitting regions. Simulations by Kollmeier et al. (2010) indicate that the net effect is small, so we neglect it here.

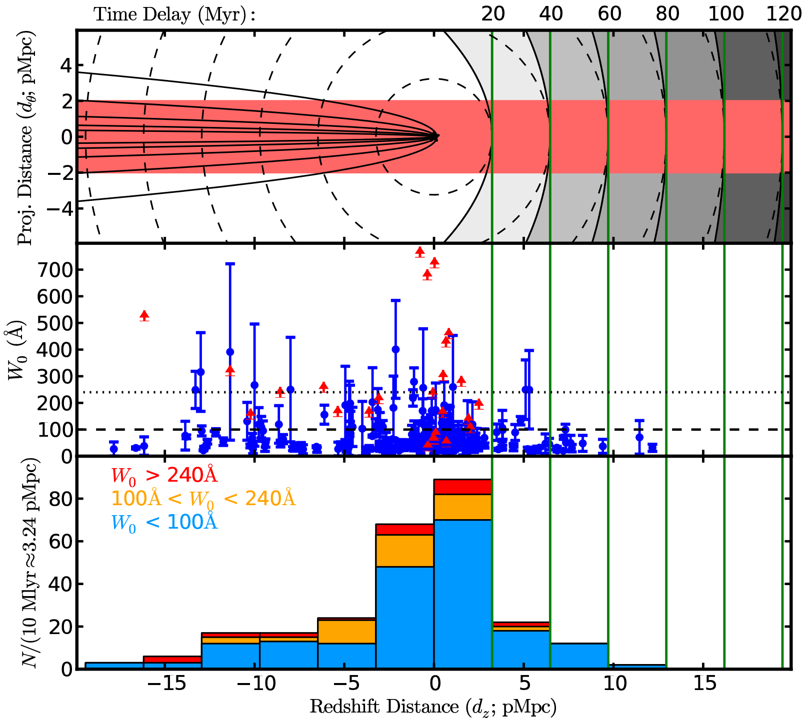

Figure 3.2: Redshift constraints on QSO lifetimes. *Top:* Schematic representation of QSO light travel with observer lying to the left of the plot. Dashed circles represent the current position of photons emitted by the QSO 10 Myr, 20 Myr, ... 60 Myr ago. Shaded parabolas on right side denote surfaces of constant t_{delay}. For the simple model of QSO emission discussed in §3.3.2, sources may only exhibit fluorescent emission if they lie in the foreground of the surface for which $t_{\text{delay}} = t_{\text{Q}}$, where t_{Q} is the QSO lifetime. The red region shows the geometry of this survey, for which surfaces of constant time delay are well-approximated by surfaces of constant redshift (green lines) for $t_{\text{delay}} \gtrsim 20$ Myr. The narrow parabolas on the left side are time-delay surfaces for $t_{\text{delay}} \leq 1$ Myr, which are shown in more detail in Fig. 3.3. *Middle:* Lyα equivalent width ($W_{\text{Ly}\alpha}$) as a function of line-of-sight distance from the QSO for LAEs with measured redshifts. Red limits and blue points are plotted as in Fig. 3.1 with the addition of 1σ error bars. Nearly all points with $W_{\text{Ly}\alpha} > 100$Å lie in the foreground of the $t_{\text{delay}} = 20$ Myr surface. *Bottom:* The redshift distribution of emitters in three bins of $W_{\text{Ly}\alpha}$, where $W_{\text{Ly}\alpha}$ is either the detected value or the 1σ lower limit. The fraction of emitters with $W_{\text{Ly}\alpha} > 100$Å drops sharply for $d_z > 10$ Mlyr ≈ 3.24 pMpc.

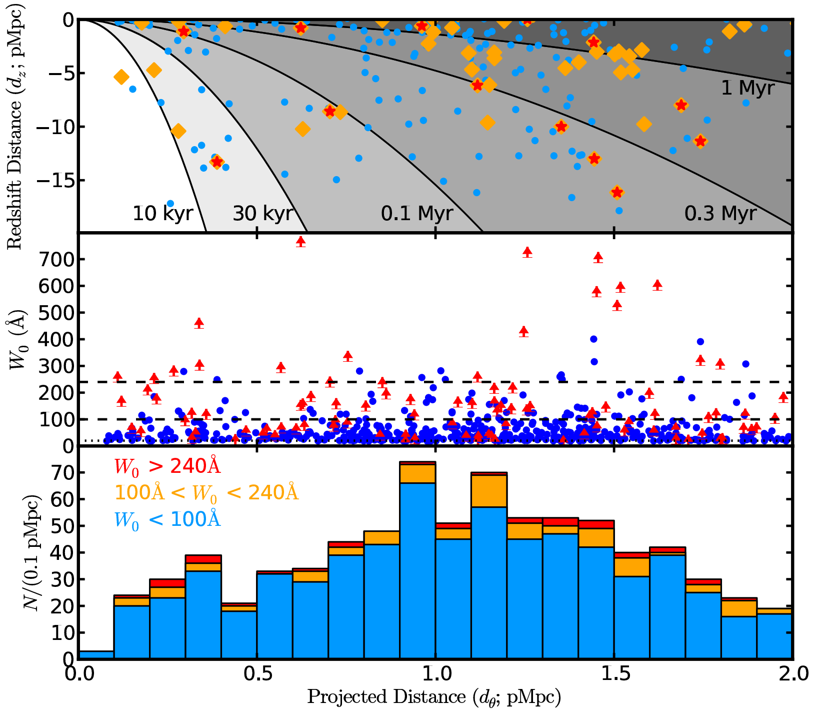

Figure 3.3: Plane-of-sky constraints on QSO lifetimes. *Top:* Schematic representation of QSO region (as in Fig. 3.2, top), with observer lying to the bottom of the plot. Shaded parabolas denote surfaces of constant time delay ($10^4 \leq t_{\rm delay} \leq 10^6$ as noted on figure). For all lifetimes $t_{\rm Q} \lesssim 1$ Myr, few or no fluorescent sources are predicted at large ($d_\theta \sim 2$ pMpc) separations from the QSO for our survey geometry. The 2D distribution of spectroscopic LAEs is shown for comparison as $W_{\rm Ly\alpha} < 100$Å (blue dots), $W_{\rm Ly\alpha} > 100$Å (orange diamonds), and $W_{\rm Ly\alpha} > 240$Å (red stars). *Middle:* Lyα equivalent width ($W_{\rm Ly\alpha}$) as a function of projected distance from the QSO for photometrically-identified LAEs. Red limits and blue points are plotted as in Fig. 3.1. Sources with $W_{\rm Ly\alpha} > 100$Å are common out to the maximum projected distances probed by our survey volume, suggesting that the QSOs in our sample have lifetimes $t_{\rm Q} \gtrsim 1$ Myr. *Bottom:* The projected distribution of emitters in three bins of $W_{\rm Ly\alpha}$, where $W_{\rm Ly\alpha}$ is either the detected value or the 1σ lower limit. The fraction of emitters with $W_{\rm Ly\alpha} > 100$Å is fairly constant for $d_\theta < 2$ pMpc.

3.3.5 Constraints on $\theta_{\rm Q}$

For $\theta_{\rm Q} \ll \pi/2$, a substantial fraction of the survey volume at large d_θ will be inaccessible to the ionizing emission of the QSO, which will affect the distribution of d_θ for fluorescent sources similarly to $t_{\rm Q} \ll 1$ Myr. We can probe $\theta_{\rm Q}$ in detail through the 2D spatial distribution of those high-$W_{\rm Ly\alpha}$ LAEs with spectroscopic redshifts. It is easily seen in Fig. 3.3 (top) that the high-$W_{\rm Ly\alpha}$ LAEs (red and orange points) extend to large projected radii at or near the QSO redshift, suggesting that ionizing emission is emanating from the QSO nearly perpindicularly to the line of sight (i.e., with $\theta_{\rm Q} \sim 90\,$deg). In reality, redshift errors and peculiar velocities prohibit us from establishing the line-of-sight distance of an LAE from the QSO to be less than 3 pMpc (see §3.3.3), so these data (with a 2 pMpc projected range) provide the constraint $\theta_{\rm Q} \gtrsim \arctan(2/3) \approx 30\,$deg.

3.4 Conclusions

We have presented constraints on the lifetime and opening angle of ionizing QSO emission based on a large photometric/spectroscopic survey of LAEs in the regions around hyperluminous QSOs (described in detail in Chapter 4), finding 1 Myr $\lesssim t_{\rm Q} \lesssim$ 20 Myr and $\theta_{\rm Q} \gtrsim 30°$.

These results are consistent with the most of the literature discussed in §3.1; in particular, our estimate of $t_{\rm Q}$ falls at the short end of the broad range allowed by the measurements reviewed in Martini (2004) and is similar to the transverse proximity effect measurements of Gonçalves et al. (2008), which included a QSO of comparable luminosity to those in this sample. Perhaps most significantly, $t_{\rm Q}$ measured here is short compared to the *e*-folding timescale of Salpeter (1964): $t_{\rm Sal} = M_{\rm BH}/\dot{M}_{\rm BH} \approx 45$ Myr for a QSO with $L = L_{\rm Edd}$ and a radiative efficiency $\epsilon = L/\dot{M}c^2 = 0.1$. Unless these QSOs have $L \gg L_{\rm Edd}$ or are accreting with a low radiative efficiency (neither of which is expected for luminous QSOs), then these observed hyperluminous accretion events do not dominate the accretion history of their central black holes.

Acknowledgments

We are indebted to the staff of the W.M. Keck Observatory who keep the instruments and telescopes running effectively. We also wish to extend thanks to those of Hawaiian ancestry on whose sacred mountain we are privileged to be guests. This work has been supported in part by the US National Science Foundation through grant AST-0908805.

Chapter 4

The Kinematic and Gaseous Properties of Lyα-Emitting Galaxies at $Z \simeq 2.7$

Abstract

We present a systematic survey of a population of faint, Lyα-emitting galaxies (LAEs) in the Mpc-scale regions around hyperluminous QSOs (HLQSOs) at $2.5 < z < 3$. The dataset of 749 photometrically-identified LAEs includes 316 with spectroscopic detections of their Lyα emission line. A sample of 35 LAEs with rest-frame optical emission line spectra from MOSFIRE are used to interpret the LAE spectra in the context of their systemic redshifts. The fields described herein are from the Keck Baryonic Structure Survey (KBSS), which includes a large amount of ancillary broadband imaging. This large, multiwavelength database allows us to characterize the distributions of LAE luminosities and Lyα equivalent widths and compare them to studies of LAEs unassociated with known, bright QSOs. We find evidence for a fluorescent contribution to their Lyα luminosities, strengthening the results of our previous studies. Using the MOSFIRE spectra, we study the distributions of Lyα-line velocities with respect to the LAE systemic redshifts, finding a small population of objects with significantly blueshifted Lyα emission, a potential indicator of inflowing gas. We also use the MOSFIRE redshifts to calibrate and stack the 316 rest-FUV LAE spectra into their rest frame, yielding the first detections of metal-enriched, outflowing winds in these faintest high-redshift galaxies. Further observations, particularly continued deep spectroscopy in the observed near-IR, are necessary to further probe the evolution and enrichment of these galaxies in the context of their QSO environments.

4.1 Introduction

While the association of Lyα emission with star formation in galaxies has long been expected (Partridge & Peebles 1967), the samples of galaxies at low redshift continually displayed extremely weak or indiscernable Lyα emission (e.g. Giavalisco et al. 1996 and references therein). Only at high redshifts did the Lyα line become an effective tool for tracing star-formation or selecting galaxies, first for individual sources (Lowenthal et al. 1991; Wolfe et al. 1992), and eventually in large numbers through narrowband surveys (e.g. Cowie & Hu 1998; Steidel et al. 2000). The increased efficacy of high-redshift surveys draws in part from logistical factors: the detection of FUV photons suffers from significant terrestrial and galactic extinction as well as technological limitations, all of which are ameliorated by allowing these photons to redshift into more accessible regions of the electromagnetic spectrum. However, the intrinsic Lyα-emitting properties of galaxies also increase with redshift out to at least $z \sim 6$ (Stark et al. 2011), and this evolution is likely driven by changes in the internal properties of galaxies that generate Lyα photons and/or inhibit their escape.

In particular, the resonant nature of the Lyα line causes these photons to experience many scatterings before leaving a galaxy, which causes the net emission to be highly sensitive to both the initial sources of Lyα photons (e.g. star-formation) and the transmissive properties of their surrounding medium (e.g. the dust, neutral gas, and their spatial and kinematic distributions). For these reasons, galaxies selected by their Lyα line (so-called Lyman-α emitters; LAEs) are found to be younger, fainter, and less reddened than those selected by the Lyman break and analogous continuum-color techniques (LBGs), despite the fact that all such galaxies emit at least low-level Lyα emission (Steidel et al. 2011).

In addition to providing a complementary population of high-redshift galaxies to LBG samples, narrowband LAE surveys provide a notable advantage for isolating volumes of specific interest for galaxy selection. The first detections of LAEs noted above came from targeting the fields and redshift intervals associated with damped Lyα absorbers (DLAs), and narrowband surveys have been used to detect large numbers of LAEs around radio galaxies (Venemans et al. 2007), QSOs (Cantalupo et al. 2007, 2012; Trainor & Steidel 2013), and known galaxy overdensities (Steidel et al. 2000; Erb et al., submitted). Such targeted surveys generate essential information on the environmental dependence of galaxy evolution while also providing a more efficient means of selecting large numbers of galaxies with respect to "blank field" studies.

Futhermore, LAE surveys drive our understanding of the faint galaxies that likely dominate the star-formation density and ionizing emission of the early universe (e.g. Robertson et al. 2013). Many aspects of galaxy properties that are well-determined for LBG samples at high redshift have not been extended to low stellar masses and continuum luminosities. Perhaps most importantly, the gaseous outflows seen ubiquitously in large samples of LBGs (Steidel et al. 1996; Pettini et al. 2001; Shapley et al. 2003) have extremely limited observational constraints in LAEs. The primary markers of these outflows are blueshifted absorption features in the spectra of galaxies, and the intrinsic faintness of LAEs in the continuum essentially prohibits these measurements in all but the most atypically luminous LAEs. The typically-redshifted Lyα line can similarly indicate the presence of outflowing winds, but only in conjunction with an independent measurement of the systemic (i.e. stellar) redshift of the galaxy. Rest-UV features associated with the systemic redshift are inaccessible in continuum-faint spectra, and rest-optical nebular emission lines have been quite observationally expensive until the recent advent of multi-object infrared spectrometers. However, it is precisely the faint LAEs that provide the most exciting enviroment for studying the kinematics of gas and galaxies. If the feedback processes omnipresent in LBGs extend to the earliest and faintest galaxies, then the effects of galaxies on their local gaseous environments must be taken into account when modeling the enrichment (e.g. Steidel et al. 2010) and transparency (e.g. Schenker et al. 2013) of the circumgalactic and intergalactic media (CGM and IGM).

In this chapter, we describe a survey of 749 LAEs in the regions around 8 hyperluminous QSOs (HLQSOs) at $2.5 < z < 2.9$. The galaxy overdensities around these luminous black holes provide a means of studying the environmental dependence of LAE population parameters (e.g. the luminosity function and equivalent width distribution in Lyα), while also allowing the efficient selection of many more LAEs than would be observable in the same time in a blank field. The higher density of sources in these fields also facilitates efficient spectroscopic follow-up, and we present rest-FUV spectroscopy of a large fraction (316/749; 42%) of these LAEs to describe their velocity distribution, emission line morphologies, and absorption spectra. Lastly, we present a smaller subsample of 35 LAEs for which we have obtained rest-frame optical spectra, thereby revealing their systematic redshifts and Lyα kinematics and allowing the calibration and interpretation of the much larger sample of rest-UV-only spectra.

The survey design and detailed descriptions of the photometric, rest-UV spectroscopic, and rest-optical spectroscopic LAE samples are given in Sec. 4.2. The distributions of photometric properties of the LAEs are given in Sec. 4.3, including measurements of the Lyα luminosity function in the HLQSOs in comparison with numerous studies of blank fields, the distribution of the measured Lyα equivalent width ($W_{\mathrm{Ly}\alpha}$) in comparison with blank fields, and the broadband photometric properties of these LAEs with respect to previous galaxy samples of LAEs and LBGs. In Sec. 4.4, we present the spectroscopic properties of the Lyα emission lines, including the measurements of the shift of the line with respect to systemic for objects with rest-optical spectra. In Sec. 4.5, we present measurements of metal absorption lines in the stacked continuum spectra of the rest-UV spectroscopic sample, and we characterize the ionization, covering fraction, and velocity distribution of star-formation driven outflows in the LAEs. A brief discussion and summary is given in Sec. 4.6. Physical quantities are given in observable units when possible, but a ΛCDM universe with (Ω_{m}, Ω_{Λ}, H_0) = (0.3, 0.7, 70 km s^{-1}) is assumed when necessary.

Table 4.1. Lyα-Emitter Field Descriptions

QSO Field	z_Q (±0.001)	NB Filter	FWHM (Å)	Exp (s)[a]	BB Filter[b]	N_{phot}	N_{spec}	N_{HST}[c]
Q0100+13 (PHL957)	2.721	NB4535	76	24,590	B+G	69	20	12
HS0105+1619	2.652	NB4430	72	21,600	B	79	22	22
Q0142–10 (UM673a)	2.743	NB4535	76	18,000	B+G	48	22	10
Q1009+29 (CSO 38)	2.652	NB4430	72	18,000	B	71	35	15
HS1442+2931	2.660	NB4430	72	18,000	B	140	41	29
HS1549+1919	2.843	NB4670	88	18,000	G	198	95	44
HS1700+6416	2.751	NB4535	76	23,400	B+G	56	20	9
Q2343+12	2.573	NB4325	74	15,896	B	88	63	23

[a] Exp is the total exposure time on LRIS-B with the corresponding NB filter in the final selection image for each field.

[b] BB Filter refers to the broadband filter (*B*, *G*, or a combination of the two) used to measure the continuum magnitude of the LAEs in each field (Sec. 4.2.1).

[c] N_{HST} refers to the number of objects in each field with *HST*/WFC3 photometry in one or both of the F140W and/or F160W filters.

4.2 Observations

4.2.1 Photometric Sample

We conducted deep imaging in each survey field using custom narrowband (NB) filters and corresponding broadband filters sampling the continuum near Lyα with Keck 1/LRIS (Oke et al. 1995; Steidel et al. 2004) over a period of several years; these observations are described in Table 4.1. All eight fields are part of the Keck Baryonic Structure Survey (KBSS; Rudie et al. 2012) and hence have ancillary images in a variety of broadband filters; the collection and reduction of these data are described in Steidel et al. (2004), Erb et al. (2006), Reddy et al. (2008), and references therein. The MOSFIRE near-infrared (NIR) *J* and *K* imaging will be described in A. Strom et al. (in prep.).

The NB images were taken as a series of 1800 s exposures with a dither pattern optimized to cover the 13.5$''$chip gap on LRIS-B. Each field had ∼10 NB exposures for a total of ∼5 hours of observing time per field, for a typical 3-σ depth of $m_{NB}(3\sigma) \sim 26.7$ as estimated through Monte-Carlo simulations of simulated fake objects. The recovered fraction of simulated objects in these simulations suggest that our survey is >95% complete (cumulatively) for $m_{NB} < 26.8$ and has a magnitude-specific completeness $\gtrsim$90% for all magnitude bins $m_{NB} \lesssim 26.8$. We used 4 NB filters for this survey, and each field was imaged with the NB filter centered most closely to the wavelength of Lyα at the redshift of its corresponding QSO. Other than their central wavelengths, the 4 NB filters have similar transmission properties, with FWHM ∼ 80 Å and a peak transmission ∼85% in all cases. As the QSOs span a redshift range $2.573 \leq z \leq 2.843$, the filter width corresponds to $\Delta z \approx 0.066$ or $\Delta v \approx 5400$ km s^{-1} at their median redshift. See Table 4.1 for more detailed statistics on each field.

The continuum filter also varied among the fields in order to effectively sample the wavelength range close to Lyα with minimal sensitivity to the continuum slope. For this reason, images were obtained using the LRIS-B *B* and/or *G* filters; the continuum image for each field is then the *B* image, *G* image, or an equal-weighted combination of the two images (see Table 4.1). In each field, the effective central wavelength of the continuum image is within $\sim$60 Å of that of the correponding NB filter. Broadband images were taken with exposure times of $\gtrsim$1 hour, for a typical 3-σ depth of $m_{\rm BB}(3\sigma) \sim 28$, again estimated through simulations of fake objects. Henceforth, $m_{\rm BB}$ denotes the measured magnitude from the broadband filter(s) used to infer the UV continuum value (*B*, *G*, or both).

Standard IRAF routines were used to reduce the data via bias subtraction, flat-fielding, cosmic-ray rejection, sky-subtraction, and image registration and combination. Before the final image combination, individual exposures were astrometrically registered to LRIS-R $\mathscr{R}$-band images previously obtained as part of the KBSS and corrected for distortion and rotation; the use of these deep broadband images for image registration ensured a high density of sources across the entire field. In this manner, we optimize the relative astrometric registration between our NB and Lyα-continuum images as well as their correspondence to the ancillary KBSS data. As part of this process, all the images are registered to the $0\farcs211$ pix^{-1} scale of LRIS-R before being combined. Gaussian smoothing was performed to one or both of the NB and Lyα-continuum images in order to match the PSFs of the two images.

Photometric calibration of the Lyα-continuum images was performed using photometric standard stars from the catalogs of Massey et al. (1988) and Oke (1990) as described in Steidel et al. (2003). The NB images were calibrated iteratively with respect to the continuum images during object selection. SExtractor was used in two-image mode to select objects in the NB image and measure their magnitudes in both the NB and continuum images. For each field, the resulting catalog and color-magnitude diagram contained a well-defined ridge of points with fairly constant $m_{\rm NB} - m_{\rm BB}$; the zero-point of the NB image was then adjusted iteratively until this ridge-line corresponded to $m_{\rm NB} - m_{\rm BB} = 0$. In fields where this ridge line was not constant in $m_{\rm NB} - m_{\rm BB}$ color, a color-dependent correction was applied to the broadband fluxes. In all cases, this color correction effectively *increased* the broadband flux, a choice we made to ensure a lack of contamination by low-$W_{\rm Ly\alpha}$ sources; however, this choice may have caused us to underestimate the value of $W_{\rm Ly\alpha}$ for the faintest objects.

The success rate of our initial follow-up spectroscopy dropped significantly above $m_{\rm NB} = 26.5$ (see Sec. 4.2.2), so our photometrically-identified LAEs are selected to have $22 < m_{\rm NB} < 26.5$. The initial object selection used in Trainor & Steidel (2013) was based on the color excess $m_{\rm BB} - m_{\rm NB} > 0.6$ (corresponding closely to a rest-frame equivalent width in Lyα [$W_{\rm Ly\alpha}$] $\gtrsim$ 20Å). However, this color excess is not a perfect proxy for equivalent width: the range of redshifts of our QSO fields mean that a given value in $W_{\rm Ly\alpha}$ corresponds to a slightly different color for each narrowband filter. Furthermore, measurement uncertainties in flux map to uncertainties in $W_{\rm Ly\alpha}$ in a non-trivial manner, particularly for sources with little or no detected

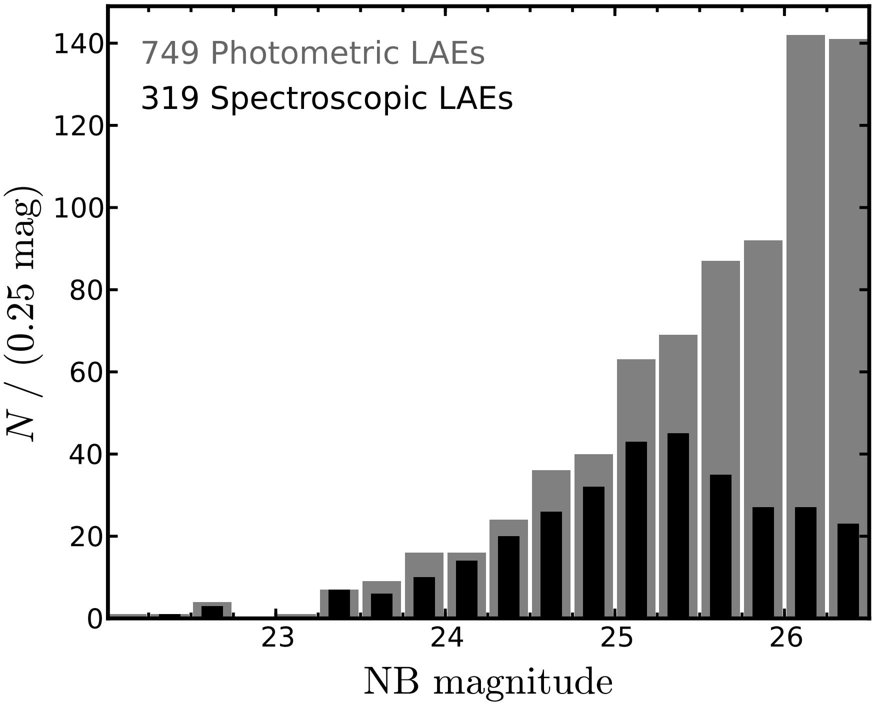

Figure 4.1: The apparent magnitude distribution of all photometric and spectroscopic LAEs observed in the survey. NB magnitude denotes the apparent magnitude of each LAE in the narrowband (NB) filter used to select it. Nearly all LAEs with NB $<$ 25.5 were targeted spectroscopically. For NB $>$ 26.5, the success rate of spectroscopic identification of the Lyα emission line dropped precipitously; for this reason, this paper primarily considers only those LAEs with a NB magnitude brighter than 26.5.

broadband flux. Because of these complexities, the best value and and uncertainty on $W_{\mathrm{Ly}\alpha}$ was estimated via a Monte-Carlo method described in Sec. 4.3.2, and the final photometric selection is such that $W_{\mathrm{Ly}\alpha} > 20$Å as determined by those methods. As in Trainor & Steidel (2013, Chapter 3), extended sources (FWHM $> 3''$) were removed from our sample for this analysis, as were objects visually identified as likely contaminants (such as those near bright stars, image defects, or the edge of the detector, as well as those with spectral signatures of contamination; see below). Via spectroscopic searches for contamination to our sample from other emission lines, we estimate a total contamination due to low-redshift interlopers of $<$3% (see below). In total, these photometric criteria define a set of 749 LAEs. This sample is slightly different from that of Trainor & Steidel (2013) because of the more robust treatment of $W_{\mathrm{Ly}\alpha}$ for faint sources, as well as stricter criteria for omitting potentially spurious sources. The apparent magnitude distribution of both the photometric and spectroscopic sample of LAEs is given in Fig. 4.1.

Photometry for the other KBSS broadband images was performed as above, using SExtractor in two-image mode to extract broadband magnitudes for the NB-defined apertures. Most of the images come from ground-based telescopes (Keck LRIS, MOSIRE; Palomar WIRC) and cover the entire $\sim 5' \times 7'$ footprint of the KBSS-Lyα fields. HST/WFC3 data were obtained in the single pointings[1] at the center of each field in the F140W (PI: Erb) and F160W (PI: Law) bands; these smaller images are $\sim 2' \times 2'$ and cover only 91 of the 749 KBSS-Lyα LAEs. These data are described in detail in Erb et al. (in prep.) and Law et al. (2012), respectively, and they are summarized in Table 4.1.

4.2.2 LRIS Spectroscopic Sample

Rest-UV spectra were obtained with Keck 1/LRIS-B in the multislit mode using the 600/4000 grism and 560nm dichroic; the spectral resolution near the observed Lyα wavelength for these spectra is $R \sim 1300$, corresponding to a velocity resolution $\sigma_v \sim 100$ km s^{-1}. Spectroscopic observations were performed in sets of 3-4 1800 s exposures, for a total of 1.5-2 hours of total integration time per object. By the completion of the survey, more than 50% of candidates in all fields had been observed, with some candidates being observed on as many as three different masks. These observations were conducted and reduced in essentially the same manner as those of the KBSS and preceding surveys, a detailed description of which can be found in Steidel et al. (2003) and Steidel et al. (2004). Specifically, masks were constructed and targets assigned as described by Steidel et al. (2003), but with a minimum slit length of $11''$in order to provide better background subtraction for these continuum-faint ($\mathcal{R} \sim 27$; see 4.3.3) sources. The data were reduced (including flat-fielding, cosmic-ray rejection, background subtraction, flexure compensation, and wavelength/flux calibration) using a set of standard IRAF tasks as described in Steidel et al. (2003). The output spectra were resampled to the median wavelength scale of the observations, 1.26 Å/pix.

The resulting one-dimensional spectra were then subjected to an automated line-detection algorithm, described here. First, each spectrum was smoothed with a kernel corresponding to the instrumental resolution (∼3.5Å FWHM). A detection region of the spectrum was then isolated: in order to ensure that spectroscopically-detected objects corresponded to their NB-selected counterparts, the algorithm only located emission lines that would fall between the 10% power points of the corresponding NB filter used to select them. The highest peak in this detection region was then used to define the first guess at the emission line wavelength. The significance of the detected peak was then estimated by

$$P(y) = 1 - \left(\int_{y_{\max}/\sigma_y}^{\infty} G(x)\, dx \right)^{n_{\rm pix}}, \tag{4.1}$$

where $y_{\max}$ is the observed peak (minus any measured continuum, which is usually not detected) in the smoothed spectrum, σ_y is the sample standard deviation of the smoothed spectrum in the detection region, $G(x) = e^{-x^2/2}/\sqrt{2\pi}$ is the normal distribution function, and $n_{\rm pix}$ is the number of pixels in the detection region of the spectrum. In this way, $P(y)$ represents the probability of measuring one or more pixels with value $y \geq y_{\max}$ within the detection region, assuming the pixel values are normally distributed with variance σ_y^2. Spectra with $P(y) \leq 0.05$ were rejected as non-detections, while those with $P(y) > 0.05$ were designated

---

[1] A second F160W pointing was obtained in the Q2343 field away from the QSO, but these data are not used in this chapter.

candidate emission lines. The total flux in each candidate emission line was then estimated both by Gaussian fitting and by direct integration of the unsmoothed spectrum. If the fit was poor (either by comparison of the two flux values or by the χ^2-value of the fit) or the signal-to-noise of the line was sufficiently high ($f_\lambda \geq 5 \times 10^{-18}$ erg s^{-1} cm^{-2} Å^{-1}), the line was re-fit using an asymmetric line profile:

$$f_\lambda(\lambda) = \begin{cases} Ae^{-(\lambda-\mu)/2\sigma^2_{\rm blue}} & \lambda < \mu \\ Ae^{-(\lambda-\mu)/2\sigma^2_{\rm red}} & \lambda \geq \mu\ . \end{cases} \tag{4.2}$$

Here, $\sigma_{\rm blue}$ represents the line-width measured from the "blue" side of the peak, while $\sigma_{\rm red}$ is the width on the "red" side of the peak. From these quantities, we can likewise define the asymmetry of the line shape, $\alpha_{\rm asym} \equiv \sigma_{\rm red}/\sigma_{\rm blue}$, a potential diagnostic of Lyα escape physics (Zheng & Wallace 2013; Chonis et al. 2013). For lines found to be multi-peaked (defined by the existence of a second peak in the smoothed spectrum at least 2.5σ above the continuum and within 1500 km s^{-1} of the primary peak), a second Gaussian or asymmetric Gaussian component was allowed to be fit as well. No more than two Gaussian components were allowed in each fit. When fitting asymmetric profiles, the fits were constrained such that neither $\sigma_{\rm blue}$ nor $\sigma_{\rm red}$ could fall below the instrument resolution ($\sigma_{\rm blue/red} > 1.5$Å). The asymmetries and multiple components of the Lyα profile will be presented in future work, and they may contain additional information about the Lyα emission and obscuration mechanisms present in these LAEs.

The observed wavelength of the emission lines were estimated via two methods: direct integration of the unsmoothed spectrum (i.e. the flux-weighted line centroid), and the fit value of μ (i.e. the peak of the fit Gaussian profile, whether symmetric or asymmetric). For multi-peaked lines, the peak of the component that encompassed a majority of the line flux was used. Henceforth in this chapter, $z_{{\rm Ly}\alpha,{\rm peak}}$ denotes the redshift of the Lyα line derived from the Gaussian peak, while $z_{{\rm Ly}\alpha,{\rm ave}}$ refers to the redshift derived from direct integration; these values are compared in Sec. 4.4.1.

The observed spectral range for each spectrum depends on the placement of the corresponding slit on the mask, but most slits were placed to cover a rest-wavelength range 900Å$\lesssim\lambda\lesssim$1500Å at $z\sim$2.7. As such, contaminants to our LAE sample were considered by searching for anomalous emission lines outside of the Lyα detection window. A small number of such objects were found. Because the narrowband filters employed in this survey all have $\lambda_c < 5000$Å, [O III] emitters are excluded by design; all the spectroscopically-identified contaminants were lower-redshift AGN in which strong C IV λ1550 ($z\sim$1.9) or He II λ1540 ($z\sim$1.7) emission was detected by our narrowband filter and misidentified as Lyα. In these systems, all of Lyα, C IV, and He II show high-equivalent-width emission. In order to control for such contaminants, each spectrum was checked by the line-detection algorithm for emission at the expected location of the other two lines in the case of a line mis-identification. In this manner, 5 objects were found where the narrowband excess was caused by C IV emission, and another 5 objects were detected due to He II emission. These objects were removed from both our spectroscopic and photometric samples. In total, these constraints define a sample of 422 spectra for 316 unique LAEs; the contamination rate for the photometric sample is thus estimated to be $10/(316+10) = 3.1\%$

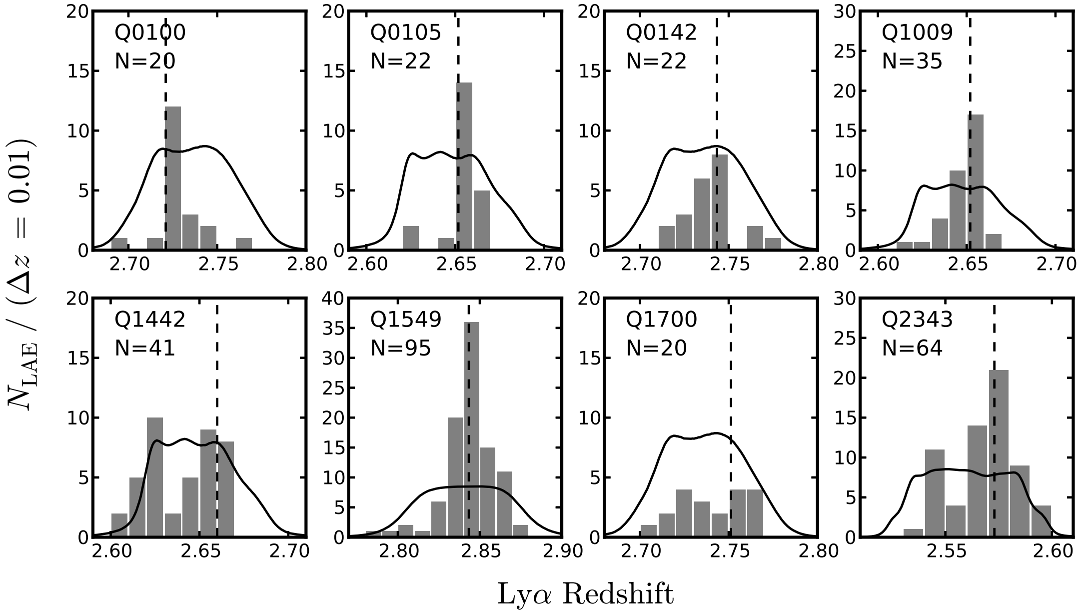

Figure 4.2: The redshift distribution of all spectroscopically-identified LAEs in each field (red). For each field, the number of objects with spectra is given in the upper left. Vertical dashed lines correspond to the HLQSO redshift in each field. Solid black lines denote transmission function for the narrowband filter used to select objects in each field; the normalization is such that N=1 is 10% transmission, the cut-off value for the automatic line-detection algorithm. Note that nearly all fields display a strong association of LAEs with the QSO redshift in addition to a more broadly-distributed component.

based on the number of these identified low-*z* AGN contaminants.

QSO redshifts were determined as described in Trainor & Steidel (2012) and have estimated uncertainties $\sigma_{\rm z,QSO} \approx 270$ km s^{-1}. The redshift distribution of LAEs with respect to their nearby QSO is shown for each field in Fig. 4.2. On small scales, the redshift distribution of LAEs with respect to the HLQSOs is more meaningful to consider as a distribution of velocities. The relative LAE-QSO velocities are calculated as in Eq. 2.4, with $v_{\rm LAE} = c(z_{\rm LAE} - z_{\rm QSO})/z_{\rm QSO}$. The distribution of QSO-centric velocities for our entire spectroscopic LAE sample is given in Fig. 4.3. In this case, the $z_{\rm LAE}$ is not equal to $z_{\rm Ly\alpha}$, but has been shifted by -200 km s^{-1} to account for the typical redshift of the Lyα emission peak with respect to systemic derived from our MOSFIRE data set; this analysis is discussed in Sec. 4.4.1.

4.2.3 MOSFIRE Spectroscopic Sample

For a small subset of these Lyα-selected objects, rest-frame optical spectra were also obtained via the new Multi-Object Spectrometer For InfraRed Exploration (MOSFIRE; McLean et al. 2010, 2012) on the Keck 1 telescope. These data were taken over the course of the KBSS-MOSFIRE survey (Steidel et al. 2014). All the MOSFIRE data considered in this analysis are from the field around the HLQSO Q2343+12 (z = 2.573). *H*-band and *K*-band spectra were obtained for 42 LAEs in this field and reduced via the MOSFIRE-DRP;

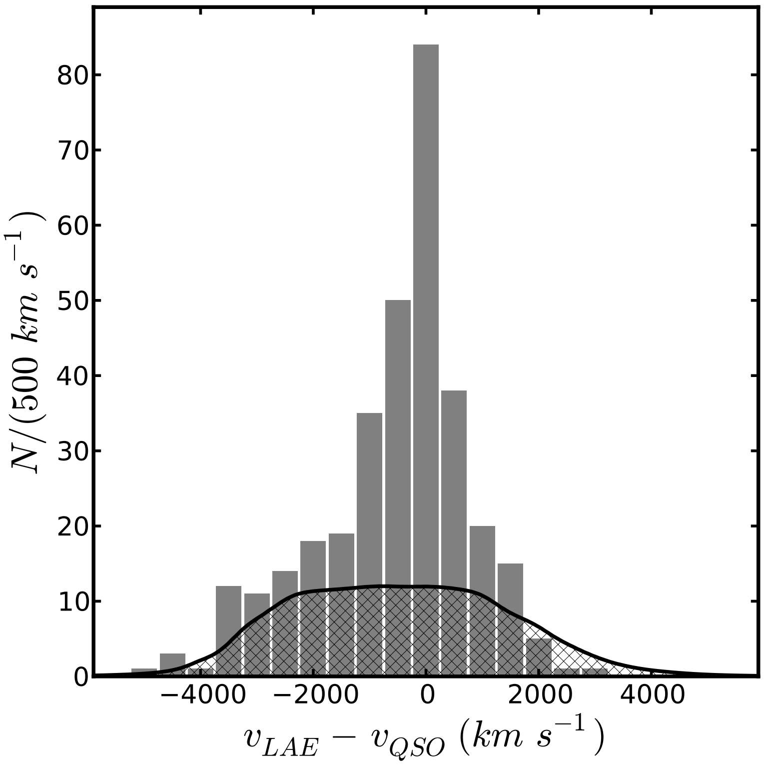

Figure 4.3: The velocity distribution of all spectroscopically-identified LAEs with respect to their nearby hyperluminous QSO. The LAE redshifts are taken from the spectral detection of Lyα, but are shifted by –200 km s^{-1} to account for the mean Lyα offset with respect to systemic. The hatched curve is the selection function defined by the set of narrowband filters used to select the LAEs.

Table 4.2. MOSFIRE Observations

Object Name	$W_{\mathrm{Ly}\alpha}$ (Å)	$z_{\mathrm{Ly}\alpha}$[a]	z_H[a]	z_K[a]	σ_{neb} (km s^{-1})[b]	$f_{\mathrm{Ly}\alpha}/f_{\mathrm{H}\alpha}$[c]
Q2343-NB0280	52.6	2.580	2.5777	2.5627	50± 5	1.9
Q2343-NB0308	58.8	2.569	-	2.5663	37± 8	6.4
Q2343-NB0345	36.9	2.592	-	2.5877	68± 0	2.5
Q2343-NB0405	134.8	2.589	2.5861	-	59± 6	-
Q2343-NB0565	313.9	2.566	-	2.5636	55± 8	3.1
Q2343-NB0791	37.4	2.571	-	2.5740	69± 8	1.1
Q2343-NB0970	44.1	2.561	-	2.5755	52±14	3.9
Q2343-NB1041	133.9	2.550	-	2.5477	31± 8	4.5
Q2343-NB1154	54.1	2.577	-	2.5907	58±10	3.1
Q2343-NB1174	236.6	2.551	-	2.5477	48± 7	5.9
Q2343-NB1361	90.6	2.560	2.5588	-	97±15	-
Q2343-NB1386	25.8	2.569	-	2.5670	50±10	0.4
Q2343-NB1416	20.7	2.560	2.5584	-	36± 6	-
Q2343-NB1501	35.2	2.561	-	2.5604	193±41	0.6
Q2343-NB1518	22.3	2.589	-	2.5860	145±32	2.8
Q2343-NB1585	303.4	2.567	2.5651	(2.5645)[d]	45± 5	7.0
Q2343-NB1692	359.2	2.562	-	2.5605	46± 7	6.7
Q2343-NB1783	35.0	2.578	2.5766	(2.5767)[d]	68± 3	1.4
Q2343-NB1789	88.2	2.547	-	2.5446	46± 8	4.7
Q2343-NB1806	19.3	2.598	-	2.5952	61±11	2.4
Q2343-NB1828	26.7	2.575	-	2.5723	83±13	2.6
Q2343-NB1829	32.1	2.578	-	2.5754	78± 9	0.9
Q2343-NB1860	23.6	2.574	-	2.5737	67±13	1.5
Q2343-NB2089	51.9	2.572	-	2.5773	68±10	2.4
Q2343-NB2211	66.2	2.578	-	2.5758	40± 5	2.8
Q2343-NB2571	29.4	2.582	-	2.5922	25± 5	1.3
Q2343-NB2785	14.2	2.572	-	2.5785	73±14	1.9
Q2343-NB2816	58.5	2.578	-	2.5737	42± 8	3.2
Q2343-NB2821	32.4	2.580	-	2.5783	45± 8	0.5

the observational strategies employed and reduction software are described in Steidel et al. (2014). Redshift fitting and object extraction were performed using the IDL program MOSPEC (A. Strom et al., in prep.). Of the 42 observed LAEs, 35 yielded redshifts via measurement of Hα (K-band, 31 objects) and/or the [O III] $\lambda\lambda 4959, 5007$ doublet (H-band, 7 objects) in emission (note that three objects have measured redshifts in both bands). Four of these objects do not meet the Lyα equivalent width threshold employed here to define LAEs in a strict sense ($W_{\mathrm{Ly}\alpha} > 20$Å), but these four are kept in the sample because they were otherwise selected via the same photometric techiniques used to define the rest of the sample, and they all display strong Lyα emission in their spectra. Further information on these spectra is given in Table 4.2 and Fig. 4.4.1. The redshift measured from the MOSFIRE spectra, whether from the H or K band, is hereafter denoted by z_{neb}. In the three cases where a measurement was obtained in both bands, the measurement of the higher-S/N H was used, but both bands generally agree quite closely ($\lesssim$ 35 km s^{-1}).

Table 4.2

Object Name	$W_{\mathrm{Ly}\alpha}$ (Å)	$z_{\mathrm{Ly}\alpha}$[a]	z_H[a]	z_K[a]	σ_{neb} (km s^{-1})[b]	$f_{\mathrm{Ly}\alpha}/f_{\mathrm{H}\alpha}$[c]
Q2343-NB2834	7.2	2.570	-	2.5654	60±12	2.5
Q2343-NB2957	23.3	2.580	-	2.5550	45± 7	1.7
Q2343-NB3061	57.6	2.579	-	2.5765	108±23	1.4
Q2343-NB3170	90.0	2.549	-	2.5499	60±12	2.6
Q2343-NB3231[e]	110.4	2.574	2.5715	(2.5709)[d]	45± 5	10.1
Q2343-NB3292	13.4	2.570	-	2.5630	38± 9	1.2

[a] $z_{\mathrm{Ly}\alpha}$, z_H, and z_K denote the redshifts measured from fitting the Lyα emission line, H band emission lines (primarily [O III λ5007]), and K band emission lines (Hα exclusively).

[b] σ_{neb} is the velocity width of the nebular emission line used to define z_{neb}. The instrumental profile width of $\sim$35 km s^{-1} has not been removed.

[c] $f_{\mathrm{Ly}\alpha}/f_{\mathrm{H}\alpha}$ is the ratio of Lyα to Hα for those objects with K-band spectroscopy. $f_{\mathrm{Ly}\alpha}$ comes from direct integration of the Lyα LRIS spectrum, while $f_{\mathrm{H}\alpha}$ is estimated by a fit to the MOSFIRE spectrum. No slit correction is applied to either measurement.

[d] In the three cases where both the H and K band spectra yielded redshifts, we adopted the higher-S/N H band redshifts to define z_{neb}.

[e] The nebular redshift of Q2343-NB3231 was measured from the [O III] λ4959Å line because the λ5007Å line did not fall on the detector.

4.3 Photometric properties of LAEs

4.3.1 The Lyα luminosity function

The distribution of Lyα-line luminosities for our photometric sample of LAEs is given in Fig. 4.4. Individual LAE luminosities are estimated using the continuum-subtracted NB image and laboratory-estimated filter width (FWHM, see Table 4.1) to infer an integrated line flux. As the redshift of each photometrically-selected LAE is not known, the luminosity distance to the QSO in each field was used to convert these integrated fluxes into luminosities.

The NB filters used to measure these fluxes are not perfectly top-hat in shape (Fig. 4.2), so some censoring and underestimation of flux will occur for those objects that fall in the wings of the filter transmission function. To account for this effect, we follow the method of Gronwall et al. (2007) and Ciardullo et al. (2012) in computing a convolution kernel to apply to the flux distribution. Those works studied the distribution of LAEs in blank fields, however, and the underlying redshift distribution was assumed to be fairly uniform. The presence of bright QSOs that are known to be associated with galaxy overdensities (Trainor & Steidel 2012) thus violate this assumption. To account for this, we applied the numerical convolution of the filter transmission function via a Monte Carlo technique that accounts for the fact that most objects lie near the QSO, where the filter transmission is highest. Specifically, emitters were simulated with redshifts drawn from a two component distribution: a combination of gaussian distribution centered on the QSO redshift

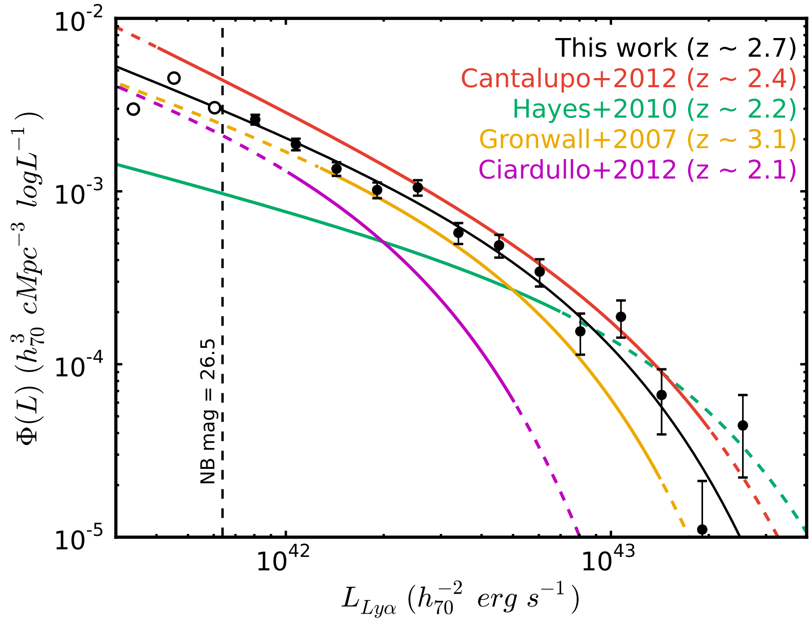

Figure 4.4: The Lyα luminosity function for the 749 LAEs in our photometrically-identified sample. In converting NB flux to a Lyα luminosity, each LAE was assumed to lie at the redshift of its nearby QSO, and a correction was made for the non-"top hat" transmission function of the NB filter (see §4.3 for explanation). The best-fit Schechter function is plotted in black. Overplotted curves correspond to Lyα luminosity functions at similar redshifts from the literature (Cantalupo et al. 2012; Hayes et al. 2010; Gronwall et al. 2007; Ciardullo et al. 2012); each curve is solid over the ranges of luminosity used to derive it and dashed to extrapolate over the entire range covered by this survey. Note that the survey of Cantalupo et al. (2012) was conducted in the field around a HLQSO of comparable luminosity to those described here, but with a more narrow selection filter. That work did not formally fit the luminosity function, but rather assumed the values of Hayes et al. (2010) for ϕ^* and L^*, adjusting α (Eq. 4.3) to provide a visually acceptable fit to their data.

Table 4.3. Best-fit Schechter Function Parameters

$\log(L^*/\mathrm{erg\ s^{-1}})$	$\log(\phi^*/h_{70}^3\ \mathrm{cMpc^{-3}})$	α	χ^2
43.04 ± 0.15	-3.49 ± 0.24	1.80 ± 0.11	10.8
43.1 (fixed)[a]	-3.58 ± 0.05	1.84 ± 0.05	10.9

[a] The Schechter (1976) function was fit in two ways; first by fitting all three functional parameters simultaneously, and secondly by fixing L^* to the value measured by Hayes et al. (2010) and assumed by Cantalupo et al. (2012). The fits (and goodness-of-fit) are nearly identical in both cases, but the covariance is significantly decreased in the fixed-L^* fit. The parameters of the full fit are used in Fig. 4.4.

and a flat distribution covering the NB bandpass. The width of the gaussian and relative normalization of the two components were chosen such that the output distribution matched the observed combined velocity distribution of LAEs with respect to their nearby QSOs (Fig. 4.3). The overall effect is a slight (∼20%) boost to the average LAE flux, and these corrections have been applied to the binned points in Fig. 4.4 in order to facilitate comparison to the curves of Gronwall et al. (2007) and Ciardullo et al. (2012), which have been similarly corrected. A χ^2 fit was also performed to the binned values using Poisson errors and assuming a Schechter (1976) functional form:

$$\phi\left(L/L^*\right) = \phi^* \left(\frac{L}{L^*}\right)^{1-\alpha} e^{-L/L^*} \tag{4.3}$$

the fit parameter values for which are given in Table 4.3. The χ^2 value of the fit is 10.8 on 9 degrees of freedom. At $z \sim 2.7$, our measurements might be expected to lie inbetween the $z \sim 3.1$ and $z \sim 2.1$ curves of Gronwall et al. (2007) and Ciardullo et al. (2012), but all our points lie above even the $z \sim 3.1$ curve. Furthermore, the faint-end slope inferred from our data ($\alpha \sim 1.8$) is steeper than those measured in the blank fields ($\alpha \sim 1.65$) but is comparable to the faint-end slope measured in populations of LBGs (e.g. Reddy et al. 2008). Notably, the break in the luminosity function is not strong, and the L^* and ϕ^* parameters are quite degenerate: if we assume $\log(L^*/\mathrm{L}_\odot) = 43.1$ (Hayes et al. 2010; Cantalupo et al. 2012), the χ^2 value increases marginally to 10.9 on 10 degrees of freedom (Table 4.3).

The shift in overall normalization is consistent with the measured overdensity of galaxies in the QSO neighborhoods from Trainor & Steidel (2012), and both the normalization and the faint-end slope closely resemble the luminosity function of Cantalupo et al. (2012), which was also measured in a single HLQSO field. That analysis is not corrected for filter censoring, but any correction would likely be minor (as here) due to the intrinsic association of the LAEs with the central QSO. In addition to including only a single field and omitting spectroscopy, the major difference between that survey and the work presented here is the width of the NB filter employed: ∼40Å in Cantalupo et al. (2012) and ∼80Å for the four filters of KBSS-

Lyα. The difference in filter width corresponds to a difference in effective survey volume, and the wider filter in our survey includes subtantial volume relatively far from the QSO, thus diluting the effect of the QSO-associated overdensity on the overall luminosity function. Accounting for this difference in effective volumes, the luminosity function measured here is almost identical to that of Cantalupo et al. (2012), though with much tighter constraints and extending to higher Lyα luminosities.

The steeper faint-end slope observed both in these data and in Cantalupo et al. (2012) is likely caused by a fluorescent contribution to the observed Lyα luminosity, in which ionizing QSO radiation incident on optically-thick H I in these gas-rich galaxies is reprocessed as Lyα photons (Cantalupo et al. 2005; Kollmeier et al. 2010). Radiative transfer simulations conducted by Cantalupo et al. (2012) show that this process causes a steepening of the Lyα faint-end slope due to the fact that the fluorescent contribution to the total Lyα flux produces the greatest fractional effect in gas-rich, intrinsically faint galaxies. In this interpretation, many of the faint objects selected near the QSOs are likely to harbor very faint stellar populations that would fall below the detection limit in a similarly deep survey in a blank field.

For comparison, similarly-constructed Lyα luminosity functions are presented for each of the eight fields individually in Fig. 4.5. The diversity among fields is apparent in the figure and can also be seen among the blank field surveys at $z \sim 2.2$ in Fig. 4.4. Nearly all the QSO fields, however, are fairly consistent with the combined luminosity function; the one exception is the field around HS1549+1919, which is the brightest QSO in the sample and was previously known to harbor an exceptionally rich overdensity of galaxies (Trainor & Steidel 2012).

4.3.2 Lyα equivalent width distribution

The rest-frame equivalent width of Lyα, $W_{\mathrm{Ly}\alpha}$, is an essential quantity for characterizing LAEs: not only does $W_{\mathrm{Ly}\alpha}$ define the selection criterion for LAEs, but its distribution is seen to evolve significantly with redshift (e.g. Ciardullo et al. 2012) and likely traces the evolving physical properties that dominate the emission and transmission of Lyα photons.

The value of $W_{\mathrm{Ly}\alpha}$ is difficult to define and to measure, however. The resonant scattering of Lyα photons through the interstellar and circumgalactic media quite generally produces diffuse Lyα halos around high-redshift galaxies that appear compact in the UV continuum (Steidel et al. 2011), causing the observed Lyα equivalent width to vary with aperture size and surface-brightness sensitivity. This issue is especially problematic in spectroscopic measurements of Lyα flux and equivalent width, where differential slit losses between the line and continuum flux can cause the Lyα line to appear in emission, absorption, or a superposition of the two even for net-Lyα-emitters (Steidel et al. 2011). Additionally, the continua of these faint, high-$W_{\mathrm{Ly}\alpha}$ sources are not significantly detected in individual spectra.

In light of these issues, we use photometric estimates of $W_{\mathrm{Ly}\alpha}$ for source selection and analysis using the narrowband and broadband UV continuum images discussed in Sec. 4.2.1. While m_{NB} and m_{BB} correspond closely to the Lyα and UV continuum fluxes, a precise estimate of $W_{\mathrm{Ly}\alpha}$ requires accounting for the Lyα

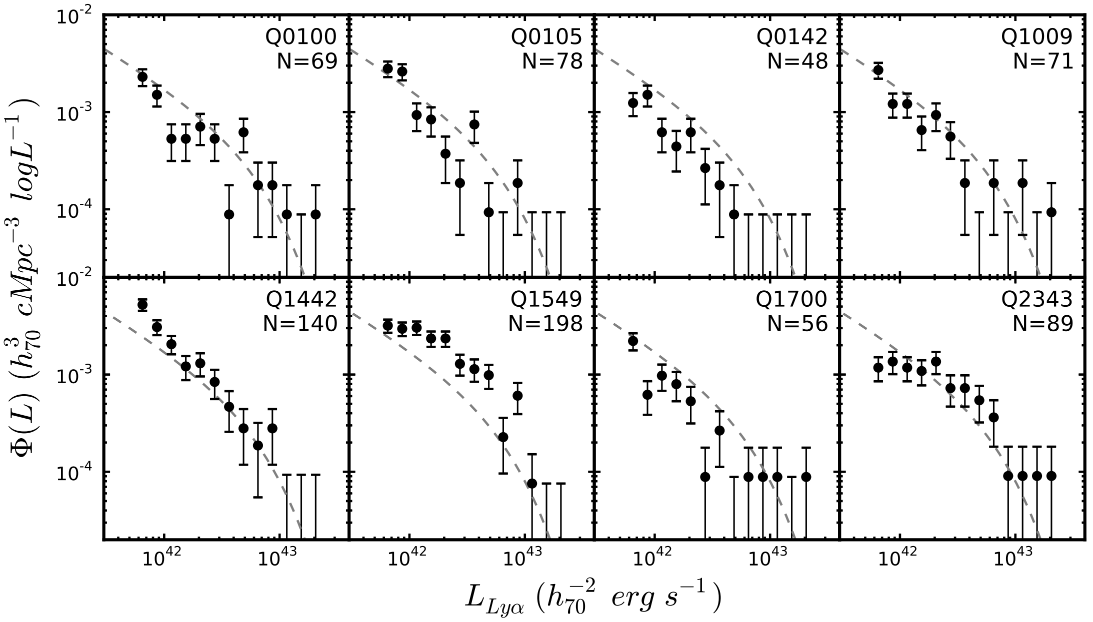

Figure 4.5: The Lyα luminosity function for each field (blue points), computed in the same manner as the overall Lyα luminosity function in Fig. 4.4 (dashed black line). The number of photometrically-identified LAEs in each field is given in the upper right.

flux falling within the broadband passband; for the highest-$W_{\mathrm{Ly}\alpha}$ sources, the Lyα line flux can dominate the measured broadband flux. The expression for $W_{\mathrm{Ly}\alpha}$ is thus given by the following:

$$W_{\mathrm{Ly}\alpha} = \Delta\lambda_{\mathrm{NB}} \left(\frac{\Delta\lambda_{\mathrm{BB}} - \Delta\lambda_{\mathrm{NB}}}{(f_{\mathrm{BB}}/f_{\mathrm{NB}})\Delta\lambda_{\mathrm{BB}} - \Delta\lambda_{\mathrm{NB}}} - 1 \right) \frac{1}{z_{\mathrm{QSO}}} \ , \tag{4.4}$$

where f_{NB} and f_{BB} are the AB flux densities corresponding to m_{NB} and m_{BB}, $\Delta\lambda_{\mathrm{NB}}$ and $\Delta\lambda_{\mathrm{BB}}$ are the effective FWHM of the narrowband and broadband images for each field (see Table 4.1), and z_{QSO} is the redshift of the nearby HLQSO, taken to be the most likely redshift for the LAEs selected in each field.

Because $W_{\mathrm{Ly}\alpha}$ is undefined for $f_{\mathrm{BB}} = f_{\mathrm{NB}}\Delta\lambda_{\mathrm{NB}}/\Delta\lambda_{\mathrm{BB}}$ in this expression, we consider it to be formally measured only if $f_{\mathrm{BB}} \geq f_{\mathrm{NB}}\Delta\lambda_{\mathrm{NB}}/\Delta\lambda_{\mathrm{BB}} + \sigma_{\mathrm{BB}}$, where σ_{BB} is the estimated error on f_{BB}[2]. If this condition is not met, only a lower limit can be set on $W_{\mathrm{Ly}\alpha}$. The dependence of $W_{\mathrm{Ly}\alpha}$ on f_{BB} also means that small errors in f_{BB} can translate to extremely large errors in $W_{\mathrm{Ly}\alpha}$ for continuum-faint sources. The uncertainties and lower limits on $W_{\mathrm{Ly}\alpha}$ thus depend on the flux uncertainties in a complicated manner, so we estimate these values via the following Monte-Carlo technique.

For each object, 1000 “observations” of f_{NB} and f_{BB} are performed in which a small error is added to both flux values; these errors are independently drawn from gaussian distributions with zero mean and variance σ^2_{NB} and σ^2_{BB}, respectively. These recomputed flux values are designated f'_{NB} and f'_{BB}. For each “observation”, $W'_{\mathrm{Ly}\alpha}$ is then computed from f'_{NB} and f'_{BB} using Eq. 4.4, so long as $f_{\mathrm{BB}} \geq f_{\mathrm{NB}}\Delta\lambda_{\mathrm{NB}}/\Delta\lambda_{\mathrm{BB}}$. If this condition

---

[2] This is equivalent to requiring that the line-subtracted continuum flux is greater than the uncertainty in the continuum flux.

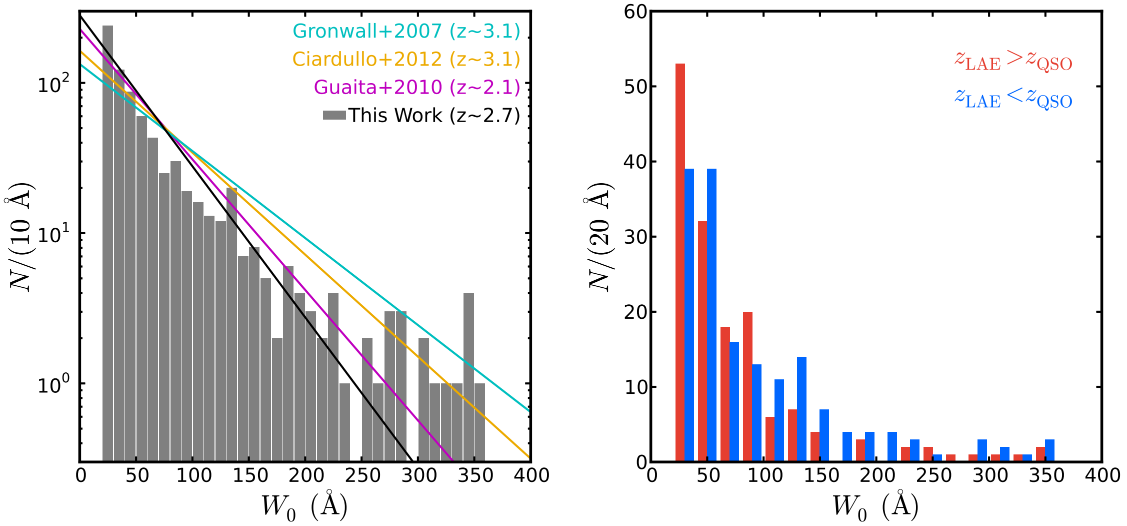

Figure 4.6: The distribution of $W_{\rm Ly\alpha}$, the rest-frame equivalent width of Lyα. *Left:* The overall distribution of $W_{\rm Ly\alpha}$ (grey), with the best-fit exponential function (blue line). The histogram is in log scale to emphasize the high-$W_{\rm Ly\alpha}$ end, where the distribution deviates strongly from an exponential. Best-fit functions from Gronwall et al. (2007), Ciardullo et al. (2012), and Guaita et al. (2010) are plotted for comparison. *Right:* The distributions of $W_{\rm Ly\alpha}$ for those LAEs with spectroscopic redshifts lying in front (blue) or behind (red) the QSO. The foreground LAEs are $\sim$20Å higher in average $W_{\rm Ly\alpha}$ than those in the background and include $\sim 2\times$ more sources with $W_{\rm Ly\alpha} > 100$Å.

is not satisfied, $f'_{\rm BB}$ is replaced by $f_{\rm NB}\Delta\lambda_{\rm NB}/\Delta\lambda_{\rm BB}$ in the computation of $W'_{\rm Ly\alpha}$. Estimated uncertainties on $W_{\rm Ly\alpha}$ are then drawn from the distribution of $W'_{\rm Ly\alpha}$: the 15.7 and 84.2 %-tile values of $W'_{\rm Ly\alpha}$ are taken as the lower and upper 1-σ uncertainties on $W_{\rm Ly\alpha}$ in cases where $W_{\rm Ly\alpha}$ is formally measured, while the 31.8 %-tile value is taken as the lower limit on $W_{\rm Ly\alpha}$ when $f_{\rm BB} < f_{\rm NB}\Delta\lambda_{\rm NB}/\Delta\lambda_{\rm BB} + \sigma_{\rm BB}$.

The distribution of $W_{\rm Ly\alpha}$ calculated in this way is given in Fig. 4.6. For comparison, best-fit exponential distribution functions from Ciardullo et al. (2012), Gronwall et al. (2007), and Guaita et al. (2010) are shown as well (parameterized as $P(W_{\rm Ly\alpha}) = e^{-W_{\rm Ly\alpha}/W_0}/W_0$). Ciardullo et al. use these fits to argue that the distribution evolves significantly from $z \sim 3.1$ to $z \sim 2.1$: Guaita et al. (2010) find a most-likely e-folding scale of $W_0 = 50 \pm 7$Å at $z \sim 2.1$, while Gronwall et al. (2007) and Ciardullo et al. (2012) find $W_0 = 64 \pm 9$Å and $W_0 = 75 \pm 6$Å respectively, for the same field at $z \sim 3.1$ using two different NB filters.

Using the maximum-likelihood estimator of the e-folding scale for our data gives $W_0 = 43$Å, and this curve is also plotted for comparison. However, none of these distributions provide an acceptable description of our data. An Anderson-Darling test for the likelihood of these data being drawn from an exponential distribution (Anderson & Darling 1954) rejects that hypothesis at probability $p \ll 1\%$. The non-exponential nature of the distribution is clear from Fig. 4.6 (left panel): while the curve fits reasonably well at $50\text{Å} < W_{\rm Ly\alpha} < 200$Å, it significantly underpredicts the fraction of LAEs with $W_{\rm Ly\alpha} > 200$Å, and all four curves underpredict the fraction of LAEs with low values of $W_{\rm Ly\alpha}$.

The failure of the exponential function to fit these data may simply be due to the size of the data set, as an underlying non-exponential $W_{\rm Ly\alpha}$ distribution can be obscured in smaller samples such as those referenced above. However, as those samples are also taken from blank fields, the differences in our sample may also be associated with the presence of the nearby QSO. It is well known that LAEs are associated on average with lower dust fractions and younger stellar populations than continuum-bright galaxies, and Ciardullo et al. (2012) suggest that the evolution of the equivalent-width distribution tracks the production of dust and aging of stellar populations over this time period. As galaxy evolution is expected to proceed more quickly in more highly-biased environments (e.g. Steidel et al. 2005; Kulas et al. 2013), it is perhaps not surprising that the scale length of the equivalent-width distribution is smaller in these overdense QSO environments in the field. On the other hand, the QSO fields also show an excess of high-$W_{\rm Ly\alpha}$ LAEs. Cantalupo et al. (2012) find a similar population of high-$W_{\rm Ly\alpha}$ LAEs in a QSO field at $z \sim 2.4$, arguing (as in Trainor & Steidel 2013, Chp. 3) that this effect is a key prediction of models of QSO-induced fluorescent emission.

The HLQSOs in this sample were estimated to have ages $t_{\rm QSO} \sim 10$ Myr based on the spatial distribution of high-$W_{\rm Ly\alpha}$ LAEs; this effect can also be seen by comparing the distribution of $W_{\rm Ly\alpha}$ itself in the foreground and background of each QSO. These distributions are given in Fig. 4.6 (right panel). As expected from the results of Trainor & Steidel (2013, Chp. 3), the distributions differ: the 164 spectroscopic LAEs in the foreground, where fluorescence is detected, have an average value $\langle W_{\rm Ly\alpha} \rangle = 94 \pm 6$Å, while the background LAEs have $\langle W_{\rm Ly\alpha} \rangle = 77 \pm 6$Å. Similarly, 57 of the 88 spectroscopic LAEs with $W_{\rm Ly\alpha} > 100$Å lie in the QSO foreground, while only 31 lie in the background (most of which are consistent with lying at the QSO redshift, given their redshift uncertainties). Under a non-parametric KS test, the foreground and background distributions of $W_{\rm Ly\alpha}$ differ with moderate significance, $p = 0.03$.

4.3.3 Continuum properties

Because the presence of the nearby QSO seems to have a strong effect on the Lyα-emitting properties of the LAEs, it is useful to consider their properties at other wavelengths in order to constrain physical properties of the LAEs themselves, including those of their stellar populations. In Fig. 4.7, we show the distribution of NB and broadband fluxes for all the rest-frame optical and NIR bands covering the KBSS fields. The data are divided into subsamples based on $W_{\rm Ly\alpha}$, and the $W_{\rm Ly\alpha} > 100$Å sample in particular consists of objects with marginal detections or non-detections in all broadband filters, including deep HST WFC3 observations in many cases.

In the following sections, we consider some detailed spectral properties of the Lyα line, some of which are shown by Erb et al. (2014, submitted) to correlate with continuum brightness. It is useful to note that the LAEs studied here are significantly fainter on average than the sample of Erb et al., which had a median $\mathcal{R}$ magnitude of 26.0; the 749 LAEs of this sample have a median $\mathcal{R} = 27.2$, including 307 objects fainter than the 3-σ $\mathcal{R}$ depth of 27.6.

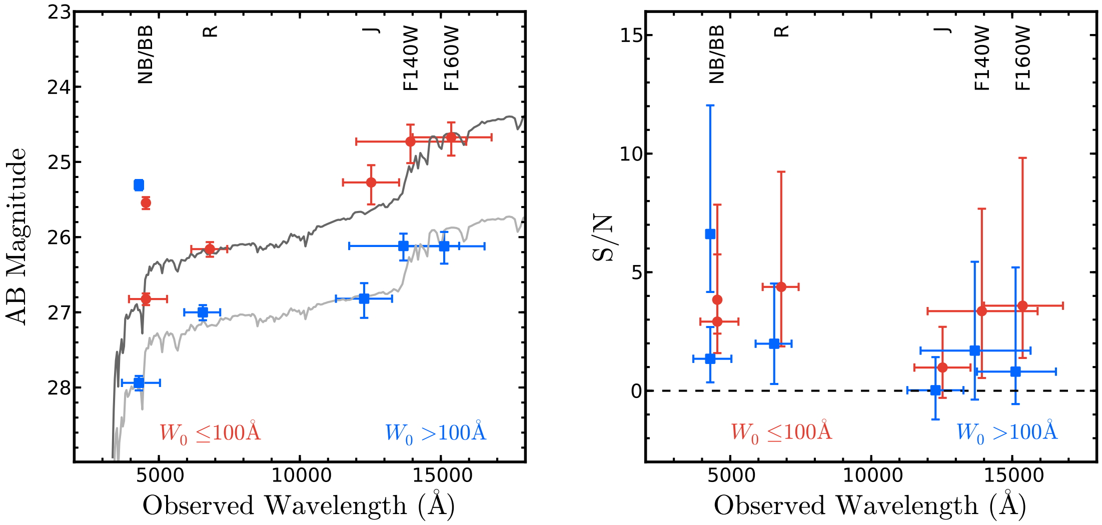

Figure 4.7: *Left:* Mean LAE fluxes in AB magnitudes. Vertical error bars denote the symmetric standard error on the mean in f_ν. Horizontal error bars display the approximate wavelength coverage of each band between half-max points; the NB filters are plotted without horizontal bars. Blue squares denote LAEs with $W_{\mathrm{Ly}\alpha} > 100$Å, while red circles denote LAEs with $W_{\mathrm{Ly}\alpha} \leq 100$Å. Note that HST/WFC3 images (F140W, F160W) do not cover the entire field (see Sec. 4.2.1), so they include a smaller number of objects. Model SEDs are plotted for comparison in grey. The dark grey curve has $\sim 3\times$ the star-formation rate and $\sim 5\times$ the stellar mass of the light grey curve. *Right:* Distribution of object signal-to-noise ratios of LAEs in each band, for each bin in $W_{\mathrm{Ly}\alpha}$. Center points are median values, while bars denote the interquartile range (25th and 75th %-tiles). A large fraction of the $W_{\mathrm{Ly}\alpha} > 100$Å sample is consistent with zero flux in all the NIR bands.

4.4 Lyman-α spectral morphology

As introduced in Sec. 4.1, the observed spectral profile of the Lyα line is the result of both the input distribution of Lyα photons produced directly from recombination and the resonant scattering that both impedes and shapes their escape. The net result of these processes in star-forming galaxies is generally seen to be the broadening of the Lyα line and an overall shift redward with respect to the systemic redshift (e.g. Shapley et al. 2003), an observation that can be simply explained by outflowing winds that drive Lyα photons to significant shifts in both space and velocity (Steidel et al. 2010). The details of these effects, however, depend on many factors, including the dust content, column density, covering fraction, and velocity distribution of the scattering medium.

As the Lyα line profile bears the imprint of these diverse galaxy and gas properties, it may be an important tool for studying galaxy evolution. However, the degenerate effects of these processes require care in their interpretation. For instance, Hashimoto et al. (2013), Schenker et al. (2013), and Shibuya et al. (2014) show that galaxies selected via their Lyα emission have a smaller velocity shift of Lyα with respect to systemic compared to continuum-selected galaxies (e.g. those of Steidel et al. 2010). Erb et al. (2014, submitted) extend this study to a large sample of LAEs and LBGs with systemic redshifts, demonstrating that the Lyα velocity shift shows a significant inverse trend with $W_{\mathrm{Ly}\alpha}$ for the combined population of galaxies selected by either technique. The physical basis of this relationship remains unclear, however. In particular, it is not clear whether the velocity offset of Lyα is predominantly driven by wind velocity (as suggested by Hashimoto et al. 2013) or H I optical depth (as suggested by Chonis et al. 2013). Furthermore, many LAEs do not exhibit simple Lyα shifts, but rather show complex, multipeaked profiles that may result from either internal star formation (Kulas et al. 2012) or externally-illuminated fluorescent processes (Kollmeier et al. 2010). In particular, Lyα lines that are blueshifted with respect to systemic may indicate systems that are dominated by inflowing H I (Verhamme et al. 2006) whose low star-formation and intrinsic Lyα-production would likely hide them from view in non-fluorescing populations. The distribution of Lyα spectral properties and their relation to other physical properties of the galaxies are thus an important window into the the processes that drive gas into and out of galaxies throughout their evolution.

4.4.1 Velocity shift with respect to systemic redshift

The offset of the Lyα line with respect to the systemic redshift was measured for each of the 36 LAEs in the MOSFIRE sample using the $z_{\mathrm{Ly}\alpha}$ and z_{neb} values estimated as described in Sec. 4.2.2 and 4.2.3. The velocity offset was then inferred from the measured redshifts as $v_{\mathrm{Ly}\alpha} = \frac{z_{\mathrm{Ly}\alpha} - z_{\mathrm{neb}}}{1+z_{\mathrm{neb}}} c$.

Postage stamps of each Lyα and nebular line spectrum in the MOSFIRE sample are displayed in Fig. 4.4.1. The majority of the nebular redshifts are derived from Hα, for which the intrinsic flux ratio $f_{\mathrm{Ly}\alpha}/f_{\mathrm{H}\alpha} = 8.7$ under the typical assumption of case-B recombination. The actual line ratios in Fig. 4.4.1 vary considerably ($f_{\mathrm{Ly}\alpha}/f_{\mathrm{H}\alpha} \sim 0.4-10.1$, Table 4.2) due to the differential slit losses and attenuation affecting Lyα and Hα

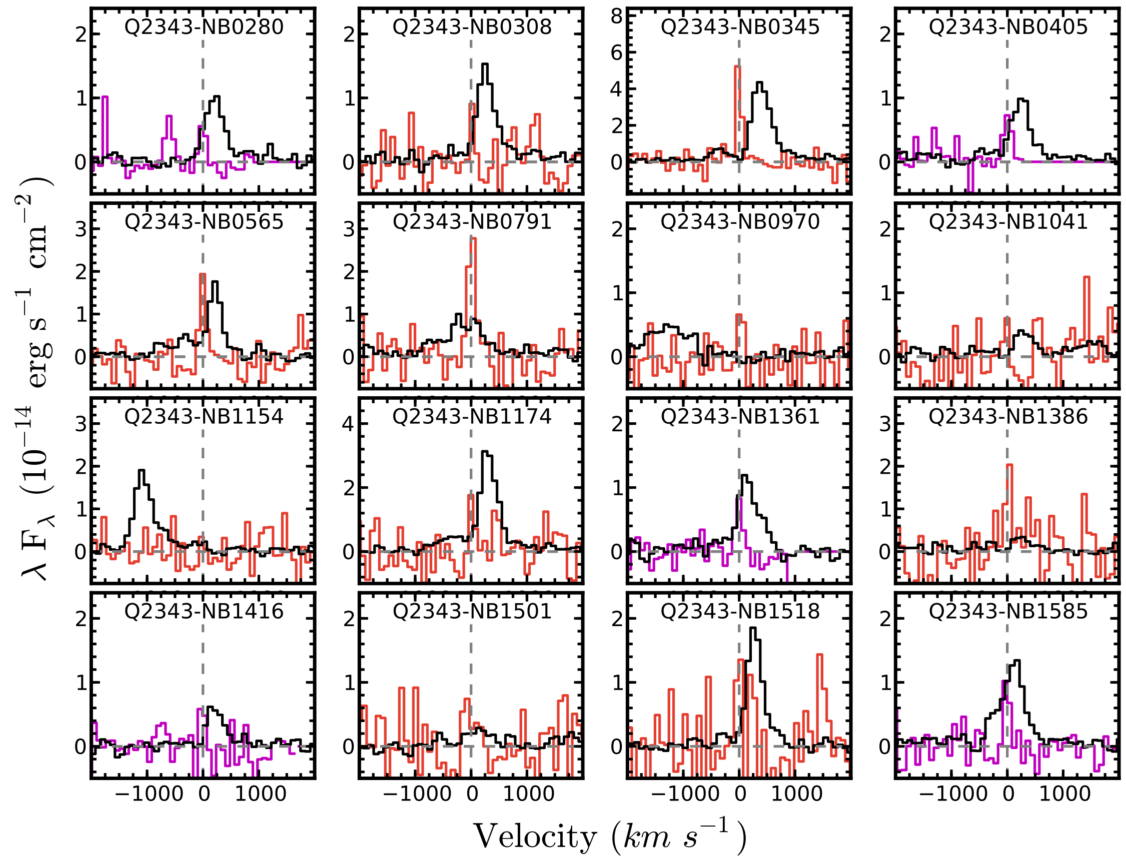

Figure 4.8: Lyα and nebular line spectra for subsample of objects with MOSFIRE redshifts. Lyα spectra (black) are from LRIS, with resolution $R \sim 1300$. Nebular spectra are for the Hαline (red) or [O III] (purple), whichever was used to estimate the systemic redshift. All [O III] spectra are for the 5007Å line with the exception of NB3231, for which we use the 4959Å line because the higher-wavelength emission line fell off the detector. MOSFIRE spectra have been down-sampled by a factor of three to match the LRIS resolution and suppress noise; the narrowest lines are resolved in the un-binned spectra. Both spectra are shifted to the redshift frame estimated from $z_{\rm neb}$. The fluxes are in λF_λ units to facilitate comparison of their integrated line luminosities.

photons.

The imperfect correspondence of the Lyα line to the systemic redshift is clear from the panels in Fig. 4.4.1. The majority (28/35; 80%) of spectra display the redshifted Lyα profile typical of star-forming galaxies, but there are several objects with minimal velocity shift, or even a dominant peak blueward of the systemic redshift. The distribution of measured velocity shifts, $v_{\rm Ly\alpha}$, is given in Fig. 4.9. The typical Lyα shift of +200 km s^{-1} is clearly visible. This shift is consistent with that found for the few samples of LAEs with systemic redshifts in the literature (e.g. McLinden et al. 2011; Hashimoto et al. 2013; Chonis et al. 2013; Shibuya et al. 2014), and significantly less than that found in typical samples of LBGs (Steidel et al. 2010).

The two panels of Fig. 4.9 show the effect of defining $z_{\rm Ly\alpha}$ by either the fitted peak ($z_{\rm Ly\alpha,peak}$) or the flux-weighted mean of the line profile ($z_{\rm Ly\alpha,ave}$; see Sec. 4.2.2). While both methods yield qualitatively

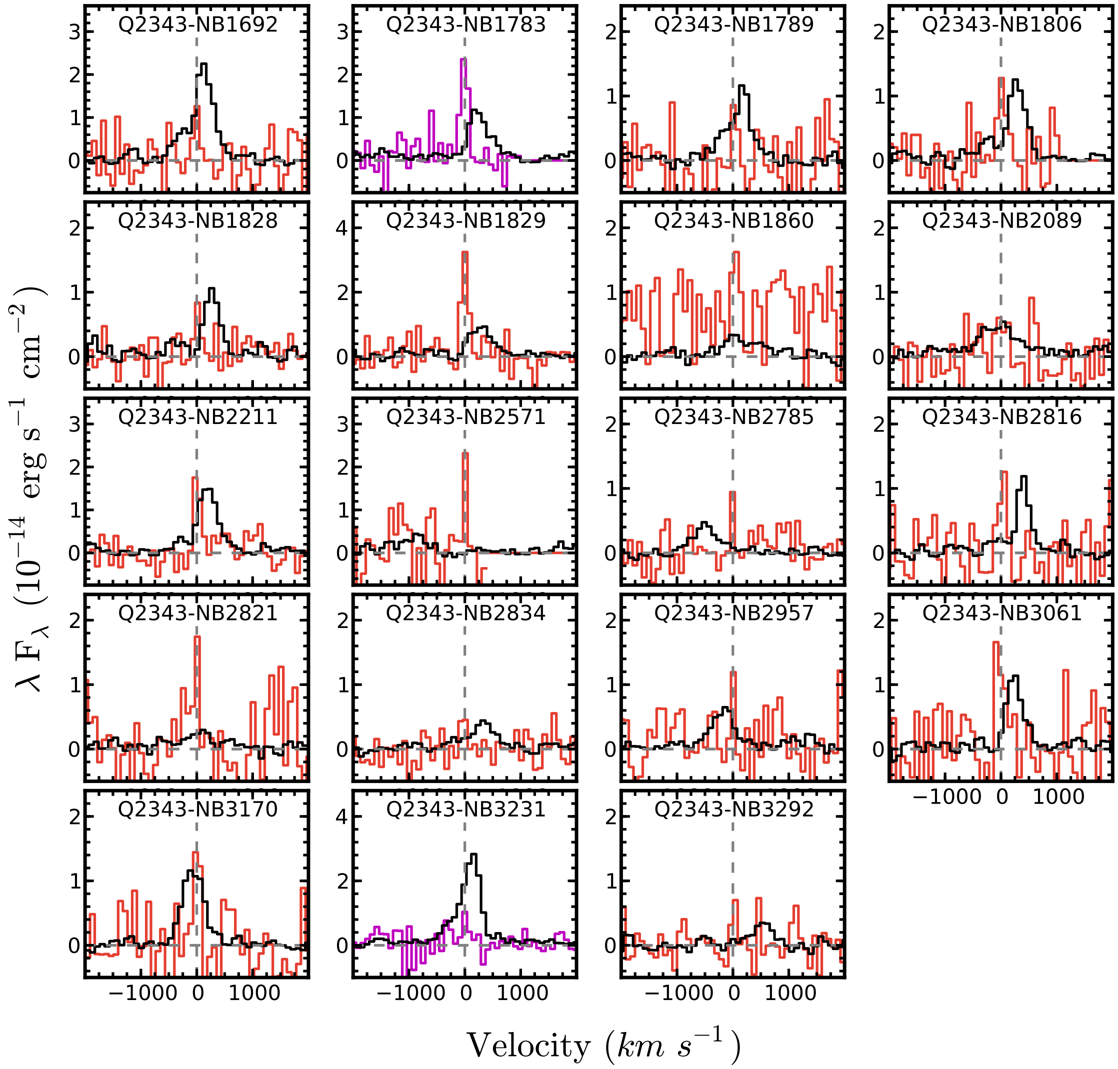

Figure 4.8: Continued.

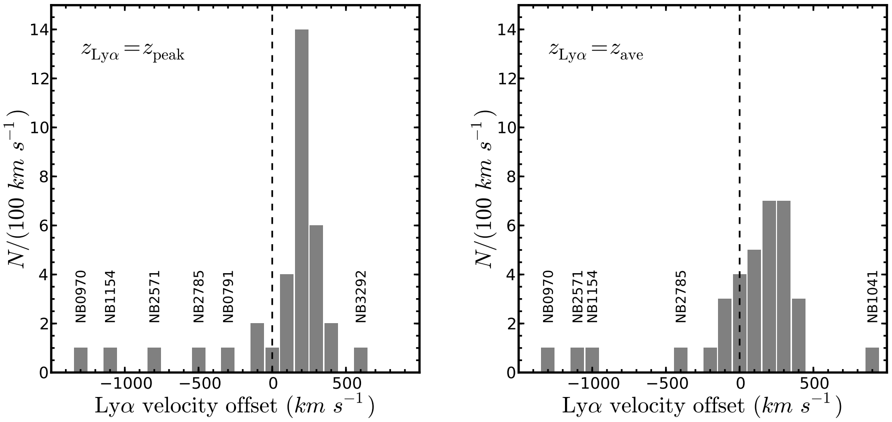

Figure 4.9: Distribution of Lyα velocity offsets for the LAEs with nebular redshifts measured with MOSFIRE. In each panel, the vertical dashed line denotes $v_{\mathrm{Ly}\alpha} = 0$. *Left:* The distribution when $z_{\mathrm{Ly}\alpha}$ is defined by the peak of the fit line profile ($z_{\mathrm{Ly}\alpha,\mathrm{peak}}$). Most of the LAEs have offsets in a tight range around $v_{\mathrm{Ly}\alpha} = 200$ km s^{-1}, but a few have Lyα lines blueshifted with respect to the systemic redshift ($v_{\mathrm{Ly}\alpha} < 0$). The LAEs falling outside this narrow peak are labeled for comparison with Fig. 4.4.1. *Right:* The distribution when $z_{\mathrm{Ly}\alpha}$ is defined by the flux-averaged central value of the line ($z_{\mathrm{Ly}\alpha,\mathrm{ave}}$). Most LAEs again have $v_{\mathrm{Ly}\alpha} \sim 200$ km s^{-1}, but with a broader distribution. Again, discrepant objects are labeled, 5/6 of which are in common with the z_{peak} plot.

similar distributions, $z_{\mathrm{Ly}\alpha,\mathrm{peak}}$ displays a markedly tighter correlation with the redshift derived from nebular emission lines than $z_{\mathrm{Ly}\alpha,\mathrm{ave}}$. Leaving aside the 7 LAEs with significantly discrepant values of $v_{\mathrm{Ly}\alpha}$ under either indicator (i.e., those labeled in either panel of Fig. 4.9), the standard deviations of the two distributions are $\sigma_{\mathrm{v,peak}} = 113$ km s^{-1} and $\sigma_{\mathrm{v,ave}} = 148$ km s^{-1}, where $\sigma_{\mathrm{v}} = \langle\Delta(z_{\mathrm{neb}} - z_{\mathrm{Ly}\alpha})\rangle$. The similarities between the two distributions suggest that either quantity is a reasonable proxy for the systemic redshift after correcting for the typical 200 km s^{-1} offset, and even the individual velocities computed by both measurements are consistent within 100 km s^{-1} for the majority of objects. Because $z_{\mathrm{Ly}\alpha,\mathrm{peak}}$ tracks z_{neb} more tightly, however, we adopt $z_{\mathrm{sys,Ly}\alpha} = z_{\mathrm{Ly}\alpha,\mathrm{peak}} - 200$ as the best estimate of the systemic redshift in the absence of nebular emission line measurements.

In addition to the distribution of average or peak Lyα line velocities, it is interesting to consider the total distribution of Lyα and nebular flux. Fig. 4.10 displays the stacked profile of the 35 LAEs in the MOSFIRE sample. Of particular note is the breadth of the Lyα profile with respect to the nebular line profile; assuming that the Lyα photons are generated by recombination processes in the same H II regions that generate the nebular emission, the left panel of Fig. 4.10 clearly displays the diffusion of the Lyα photons in velocity as they resonantly scatter through the surrounding H I gas. Fitting a Gaussian function to the stack of nebular lines yields a velocity width of $\sigma_{\mathrm{neb}} = 50 \pm 2$ km s^{-1}, while the stacked Lyα profile has a width of $\sigma_{\mathrm{Ly}\alpha} = 162 \pm 8$ km s^{-1} for the primary (red) peak. These figures include the instrumental resolution of MOSFIRE (~ 35 km s^{-1}) and LRIS (~ 100 km s^{-1}) in their observed modes; subtracting this factor in quadrature yields intrinsic widths of $\sigma_{\mathrm{neb}}^{\mathrm{intrinsic}} \simeq 40$ km s^{-1} and $\sigma_{\mathrm{Ly}\alpha}^{\mathrm{intrinsic}} = 127$ km s^{-1}. The peak of the stacked Lyα spectrum is again quite close to +200 km s^{-1}, but there is a distinct component blueward of the systemic

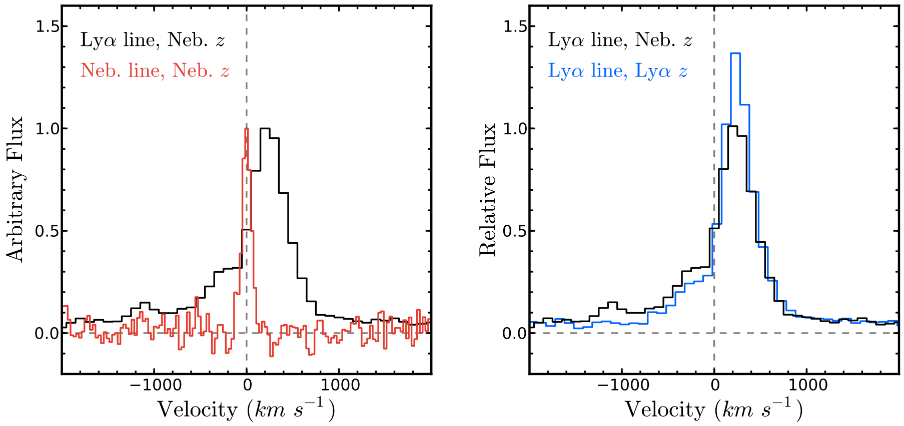

Figure 4.10: Stacked spectral profiles for the 36 LAEs with systemic (nebular) redshift measurements. *Left:* Comparision of the stacked nebular (red) and Lyα (black) line profiles for these LAEs. The nebular stack consists of both Hα and [O III] λ5007 lines where available. The lines are stacked according to their corresponding nebular redshifts, and the effect of resonant scattering on escaping Lyα photons is clearly visible, as is the typical Lyα velocity offset of $\sim$ 200 km s^{-1} redward of systemic. *Right:* Comparison of the average Lyα profiles when spectra are stacked according to their nebular, systemic redshift (black, as above) and a redshift derived directly from the Lyα line peak (blue, shifted +30 km s^{-1} for clarity), wherein the "systemic" redshift is estimated as $v_{\mathrm{sys,Ly}\alpha} = v_{\mathrm{Ly}\alpha} - 200$ km s^{-1}. Stacking via the Lyα redshift distorts the Lyα profile and diminishes the measured flux blueward of the systemic redshift.

redshift as well. After subtracting the low-level continuum, the fraction of Lyα line flux emitted blueward of $v = 0$ is 29%. For comparison, we show the effective profile that would result from stacking all the Lyα lines at the redshifts derived from the Lyα line and then making a +200 km s^{-1} shift in the right panel of Fig. 4.10. The resulting profile is narrower ($\sigma_{\mathrm{lya}} = 129 \pm 5$ km s^{-1}), and only 15% of the continuum-subtracted line flux is measured to be emitted at $v < 0$, roughly half of what is measured using the true systemic redshifts.

4.5 Evidence for winds in stacked spectra

4.5.1 Absorption signatures

While the resonance of the Lyα transition makes it a strong tracer of gas in and around high-redshift galaxies, this strong coupling can obscure the details of the physical processes driving Lyα absorption and emission. In particular, we note in Sec. 4.4 that Lyα transmission is sensitive to a variety of factors, including the optical depth, covering fraction, dust content, and kinematics of the gas distribution. Because they produce degenerate effects on the Lyα profile, Lyα emission alone is insufficient to fully characterize the dominant emission mechanisms and physical conditions in LAEs or high-redshift galaxies generally.

The measurement of non-resonant lines in the UV continuum spectra of galaxies is thus a crucial tool for disentangling these effects. Detailed analysis of the continuum spectra of typical high-redshift galaxies began with spectra of the gravitationally-lensed $z \sim 2.7$ galaxy MS 1512-cB58 (Pettini et al. 2000, 2002) and was extended to non-lensed galaxies through stacking the spectra of many ($\sim$1000) $z \sim 3$ LBGs by Shapley et al. (2003). These studies utilized the high S/N of the lensed or stacked spectra to extract metal abundances, ion-specific covering fractions, wind velocities, and systemic redshifts for the galaxies while placing these properties in the context of their star-formation rates, masses, and Lyα emission properties. For faint LAEs such as those in our sample, constraints on the metal content and wind velocities are especially interesting because they reveal the extent to which past and on-going star formation are already having an effect on the chemistry and kinematics of these particularly young, low-mass galaxies.

LAEs are by selection generally faint in the continuum, so absorption measurements of comparable fidelity to those of Shapley et al. (2003) are impossible in even the largest stacks of galaxies similar to those considered here. Hashimoto et al. (2013) consider the absorption profiles in a stack of 4 LAEs with systemic redshift measurements to measure wind velocities, and Shibuya et al. (2014) conduct a similar analysis in individual bright LAEs, finding typical outflow velocities $v_{\rm abs} \sim 100-200$ km s^{-1}. However, the objects in these studies have *B*-band magnitudes $\langle m_{\rm B} \rangle \sim 24$, suggesting that they would easily fall within typical selection criteria for continuum-selected star forming galaxies. While useful for studying the correlation between wind velocity $v_{\rm abs}$ and $W_{\rm Ly\alpha}$, these samples are clearly far removed from the faint LAEs considered in this thesis, with median continuum magnitude $\langle m_{\rm B} \rangle = 26.8$.

For such faint objects, large samples are needed to obtain even a low-fidelity measurement of metal absorption. Stacking our entire sample of 35 LAEs with MOSFIRE redshifts does not yield sufficient signal to measure individual absorption line strengths and velocities. However, the results of Sec. 4.4.1 demonstrate that the peak of the Lyα line is an excellent proxy for the systemic redshift for the majority of LAEs meeting our selection criteria. Using this correlation, we can stack the rest-UV spectra of all 316 LAEs with measured Lyα redshifts using a rest frame defined by $z_{\rm sys,Ly\alpha} = z_{\rm Ly\alpha,peak} - 200$ km s^{-1}. As many of our objects have multiple LRIS spectra of their rest-FUV continuum, we include all spectra for each object such that each spectrum received equal weighting, effectively weighting each object by total exposure time.[3] Furthermore, two spectra with individually-significant continua (likely AGN) were removed from the sample in order ensure that they did not dominate the stack; all the remaining spectra have S/N $\ll 1$ in the continuum. Lastly, the portion of each spectrum corresponding to $\lambda \approx 5577 \pm 15$Å in the observed frame was omitted from the stack in order to remove contamination from a bright sky line. In total, 422 LAE spectra were stacked, producing a final spectrum with an effective exposure time of $\sim$675 hours.

An error spectrum was then generated for the stack via a bootstrapping procedure. 1000 iterations were performed in which 422 spectra were drawn (with replacement) from our sample and stacked to make a set of 1000 randomized spectral stacks. The standard deviation of values at each pixel was then used to define the error spectrum of the true stacked data. From this error spectrum, we estimate that the stack has a median S/N ~ 10 in the range 1230Å $\lesssim \lambda_{\rm rest} \lesssim$ 1420Å, the range of interest for the absorption lines discussed below.[4]

---

[3] The results of the continuum stacking are insensitive to whether the objects are weighted equally, weighted by number of spectra, or weighted by total exposure time.

[4] Unfortunately, we are unable to obtain robust measurements of the C IV doublet 1549,1551Å, generally one of the strongest

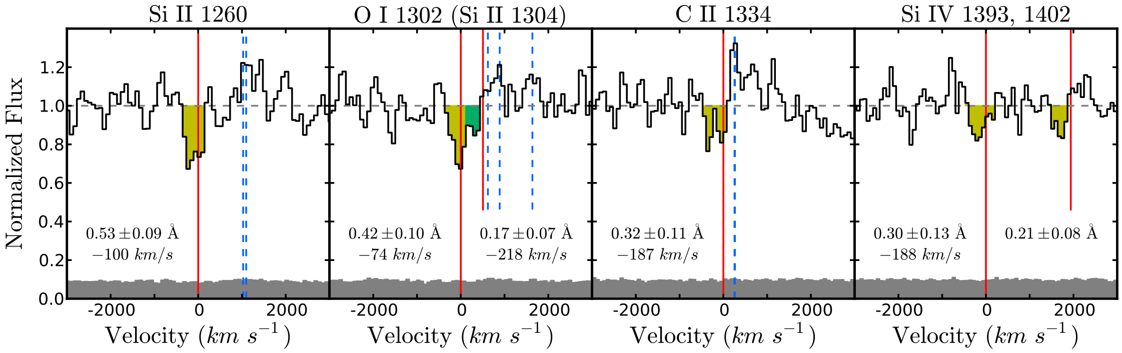

Figure 4.11: Interstellar absorption signatures of metal lines in the stacked spectrum of all 316 spectroscopic LAEs. Vertical red lines are the rest-wavelenths of metal ions seen in absorption, while dashed blue lines denote the wavelengths of fine-structure and nebular emission features. A detailed list of these lines is given in Table 4.4. Yellow shaded regions are the areas used to calculate the equivalent width and absorption-weighted velocity of each species; the absorption estimated for Si II λ1304 is shaded green to differentiate it from the partially-blended O I λ1302 absorption. Uncertainties for the equivalent width measurements are estimated via a bootstrapping procedure described in the text; the bootstrapped error spectrum is displayed in grey at the bottom of each panel.

Measurements were made of the absorption of six metal lines, corresponding to four spectral regions (Fig. 4.11, Table 4.4). For each spectral region, the continuum level was independently estimated using the local median value, but the estimates among all four regions are consistent to $\lesssim$ 2% in λf_λ units. The measured continuum was also checked for consistency with the broadband photometry. At the median wavelength of the absorption lines ($\lambda_{\rm obs} \sim$ 5000Å), the stacked continuum flux is $7.5 \sim 10^{-8}$ Jy (m_{5000} = 26.72), comparable to the mean Lyα-subtracted broadband B/G flux ($7.9 \sim 10^{-8}$ Jy; $\langle m_{\rm BB} \rangle$ = 26.66) measured photometrically among the 318 objects in the spectral stack. Absorption measurements were then made for the low-ionization lines Si II λ1260, O I λ1302, Si II λ1304, and C II λ1334, as well as the high-ionization doublet Si IV $\lambda\lambda$1393,1402. The equivalent width of absorption is estimated in each case by numerically integrating the set of continuous pixels with $f_{\rm norm} < 1$ nearest the rest-frame metal-line wavelength in the normalized stack. The O I λ1302 and Si II λ1304 absorption lines are partially blended, so the division between them was determined by visual inspection of the stacked spectrum. Uncertainties in the equivalent width were computed by performing the same measurement for each line in each of the 1000 bootstrap spectra; the quoted error refers to the standard deviation of these bootstrap measurements. An absorption-weighted velocity was then measured for each line via numerical integration of the line profile: $v_{\rm abs} = \int [1 - f_{\rm norm(v)}] v dv$. While the equivalent widths in absorption of the two lines in the Si IV doublet were measured separately, they were constrained to have the same total absorption-weighted velocity.

All the measured absorption lines have measured mean velocities $\langle v_{\rm abs} \rangle \sim 100-200$ km s^{-1} with absorption extending to $v_{\rm abs} \sim 500$ km s^{-1}, in good agreement with the brighter LAE samples of Hashimoto et al.

---

absorption lines in high-redshift galaxies and a key indicator of AGN activity when seen in emission. Because we favor the resolution of the 600-line grism over the increased spectral range of the 300 or 400-line grisms, the C IV doublet falls off the spectrograph for many of our objects. Furthermore, the particular redshift range of our LAEs ($z \sim 2.6$) causes significant contamination near $\lambda_{\rm rest} \sim$ 1550Å due to the bright sky line at $\lambda_{\rm obs} \sim$ 5577Å.

Table 4.4. LAE Continuum Absorption Features

Ion	λ_{lab}[a]	f[b]	W_{ion} (Å)[c]	A_{ki} (10^8 s^{-1})[e]
Absorption features				
Si II	1260.422	1.007	0.53 ± 0.10	-
O I	1302.169	0.04887	0.43 ± 0.10[d]	-
Si II	1304.370	0.094	0.17 ± 0.08[d]	-
C II	1334.532	0.1278	0.32 ± 0.11	-
Si IV	1393.760	0.5140	0.30 ± 0.12	-
Si IV	1402.773	0.2553	0.21 ± 0.08	-
Emission features				
Si II*	1264.738	-	-	30.4
Si II*	1265.002	-	-	4.73
O I*	1304.858	-	-	2.03
O I*	1306.029	-	-	0.676
Si II*	1309.276	-	-	6.23
C II*	1335.663	-	-	0.476
C II*	1335.708	-	-	2.88

[a] Vacuum wavelength of transition

[b] Oscillator strength as in Pettini et al. 2002 (reproduced from Shapley et al. 2003)

[c] Equivalent width of absorption in stacked spectrum (Fig. 4.11)

[d] The O I λ1302 and Si II λ1304 absorption lines are partially blended, so the division between them is somewhat uncertain.

[e] Einstein A-coefficients from the NIST Atomic Spectra Database (www.nist.gov/pml/data/asd.cfm)

(2013) and Shibuya et al. (2014). Because the systemic redshifts are not precisely known for the LAEs in our stack, there may be some additional uncertainty in our measured velocities compared to those measured in samples with complete catalogs of systemic reshifts. However, our stacked spectra also show several fine-structure and nebular emission features (Fig. 4.11) that are more likely to trace the systemic galaxy redshifts; the correspondence of these peaks to the rest-frame wavelengths of these features further suggests that our corrected Lyα line measurements are a good proxy for the redshifts in these LAEs.

In addition to the velocities of this outflowing gas, these absorption lines likewise constrain its covering fraction, f_c. Because the Si II λ1304 line suffers from partial blending with O I λ1302 it is difficult to robustly measure the equivalent-width ratio W_{1260}/W_{1304} and thus the optical depth of Si II; however, the depth of the Si II λ1260 absorption implies that the covering fraction of Si II must be at least $\sim$30%. Similarly, O I and C II display a covering fraction $\gtrsim$20-25% as well. This consistency among the low-ionization species suggests they likely correspond to a neutral gas covering fraction $f_c \sim$30%.

The two lines of the Si IV doublet have a ratio W_{1393}/W_{1402} = 1.4, suggesting that the doublet is saturated (W_{1393}/W_{1402} = 2 on the linear part of the curve of growth). However, the weaker line has S/N $\sim$ 2, and $\sim$25% of the bootstrap spectra have $W_{1393}/W_{1402} \gtrsim 2$, so the transition may in fact be optically thin. The high ionization potential of Si IV (33.5 eV) requires radiation from hot stars and/or collisional ionization in $T \gtrsim 10^4$K gas, and therefore traces ionized gas in or around the galaxy. The depth of the two absorption lines thus suggests the presence of an ionized medium with an average covering fraction $f_c \sim$ 20% (or greater if the lines are optically thin).

The velocity shift of the Lyα line shows a strong inverse trend with Lyα equivalent width in the collective populations of high-redshift LAEs and LBGs (Erb et al., submitted), but there many mechanisms that could underly this relationship. If a change in outflow velocity is the driver, then we should expect the velocity profile of the metal absorption lines tracing the winds to vary with $W_{\text{Ly}\alpha}$ as well. Unfortunately, the S/N in stacked subsamples is too low to probe this evolution in individual lines. However, we can boost the S/N by combining the line profiles for multiple lines that we expect to trace the same gas. In particular, we can stack the low-ionization lines (corresponding to neutral H I gas) and the high-ionization lines (corresponding to ionized H II gas) and thereby extract enough signal to probe the variation of the gas velocity distribution with $W_{\text{Ly}\alpha}$.

Spectra combined in this way are displayed in Fig. 4.12 for three subsamples in $W_{\text{Ly}\alpha}$. Because these stacks include features at several different redshifts, we subsampled them by a factor of two with respect to the original wavelength scale before stacking in order to maximize the velocity resolution of the stacks. The $W_{\text{Ly}\alpha} \geq$ 60Å sample includes 158 LAEs ($\langle W_{\text{Ly}\alpha}\rangle$ = 135Å), the $20 \leq W_{\text{Ly}\alpha} <$ 60Å sample includes 160 LAEs ($\langle W_{\text{Ly}\alpha}\rangle$ = 38Å), and the $W_{\text{Ly}\alpha} <$ 20Å sample includes 82 objects ($\langle W_{\text{Ly}\alpha}\rangle$ = 10Å) that were selected by our narrowband filter and whose spectra show Lyα in emission but have photometric measurements of $W_{\text{Ly}\alpha}$ too low to fall into our sample of "true" LAEs. Details of these subsamples are in Table 4.5.

Several key features are apparent in the bottom panels of Fig. 4.12. Firstly, there is substantial absorption

Table 4.5. LAE Spectroscopic Subsamples

Subsample	$\langle W_{\mathrm{Ly}\alpha} \rangle$	N_{obj}	N_{spec}[a]	σ_{red} (km s^{-1})[b]	σ_{blue} (km s^{-1})[b]	Δv (km s^{-1})[b]
$W_{\mathrm{Ly}\alpha} \geq 60$Å	135Å	158	211	156±2 (120)	216±6 (191)	451±4
$20 \leq W_{\mathrm{Ly}\alpha} < 60$Å	38Å	160	211	156±2 (120)	292±11 (274)	474±5
$W_{\mathrm{Ly}\alpha} \leq 20$Å	10Å	82	94	159±3 (124)	369±27 (355)	482±7

[a] Because some objects were observed multiple times, and all available spectra were combined in each continuum stack, $N_{\mathrm{spec}} > N_{\mathrm{obj}}$.

[b] The parameters σ_{red}, σ_{blue}, and Δv are the velocity widths of the red peak, blue peak, and peak separation in the fit to the stacked Lyα spectrum (Fig. 4.12). The numbers in parentheses reflect the subtraction (in quadrature) of the LRIS instrumental resolution of ~100 km s^{-1}.

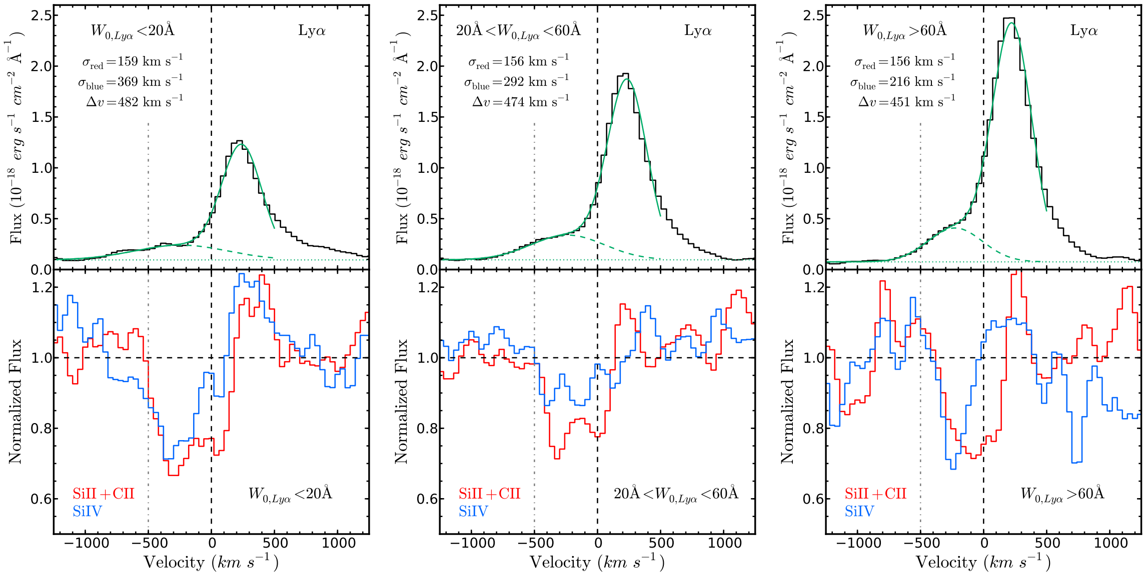

Figure 4.12: Lyα emission and interstellar absorption signatures in stacked subsets of spectra grouped by their photometric Lyα equivalent width, $W_{\mathrm{Ly}\alpha}$. Details of each subsample are given in Table 4.5. *Top panels:* Lyα emission spectra (black), and profile fit (green) for each subsample. The solid green line is the full fit, the dotted green line is the fit continuum level, and the dashed green line is the blue-shifted Gaussian component of the fit. The fits do not extend to $v > +500$ km s^{-1}, as this portion of the spectrum was omitted during fitting. Dashed and dot-dashed vertical lines denote $v = 0$ and $v = -500$ km s^{-1}, respectively. Note that the Å^{-1} in the flux units is measured in the observed frame; the specific flux is ~3.7× higher per unit rest-frame wavelength. *Bottom panels:* Red curves are the average absorption profiles of the low-ionization species Si II λ1260 and C II λ1334, while blue curves are the absorption profiles of the more highly ionized Si IV (λ1393 and λ1402). O I λ1302 and Si II λ1304 are omitted due to blending. As above, dashed and dot-dashed vertical lines denote $v = 0$ and $v = -500$ km s^{-1}, while the dashed horizontal line denotes the local continuum level.

by low-ionization lines in all three panels at the systemic redshift of the galaxy ($v = 0$), but there is little or no corresponding high-ionization absorption at $v = 0$. At the negative edge of the absorption profiles ($v \sim -500$ km s^{-1}), however, the high-ionization and low-ionization absorption are well aligned in each panel. This pattern indicates that both ionized and neutral gas are present in the blueshifted outflow, but the interstellar medium is dominated by neutral H I and low-ionization metals at the systemic redshift. This result holds for all three subsamples in $W_{\mathrm{Ly}\alpha}$.

Secondly, if the lines are assumed to be optically-thick, there is a slight trend in covering fraction as a function of $W_{\mathrm{Ly}\alpha}$: $f_c \sim 30\%$ for the $W_{\mathrm{Ly}\alpha} \sim 10$Å sample, $f_c \sim 20\%$ for the intermediate sample, and $f_c \sim 25\%$ for the lowest-$W_{\mathrm{Ly}\alpha}$ sample. The decline in f_c from $W_{\mathrm{Ly}\alpha} \sim 10$Å to $W_{\mathrm{Ly}\alpha} \sim 38$Å is consistent with expectations for Lyα-emitting galaxies: Steidel et al. (2010) demonstrate that observed Lyα-emission is closely correlated with the covering fraction of the gas through which these photons escape. The increase in f_c from $W_{\mathrm{Ly}\alpha} \sim 38$Å to $W_{\mathrm{Ly}\alpha} \sim 135$Å may not be significant because the continuum emission is extremely faint in the highest-$W_{\mathrm{Ly}\alpha}$ stack; not only is the statistical error large, but small systematics in the spectroscopic background subtraction could be significant in the stack of these faint objects and thus bias the measured continuum level. However, the consistency between the photometric and spectroscopic continuum estimates suggests this effect should be quite small. In any case, it seems that f_c correlates only weakly with $W_{\mathrm{Ly}\alpha}$ for these faintest, highest-$W_{\mathrm{Ly}\alpha}$ galaxies.

Thirdly, there is some evolution in the maximum absorption velocity as a function of $W_{\mathrm{Ly}\alpha}$. While the absorption extends to $v_{\mathrm{abs}} \sim -500$ km s^{-1} in all three panels, the $W_{\mathrm{Ly}\alpha} \sim 10$Å stack shows absorption in Si IV extending to higher velocities at low optical depths. Conversely, the outer edge of absorption in the $W_{\mathrm{Ly}\alpha} \sim 135$Å stack extends no further than $v_{\mathrm{abs}} \sim -400$ km s^{-1}.[5] It is important to note that the systematic velocities used here are derived from a constant correction to the Lyα redshift, and thus the evolution of the Lyα offset with $W_{\mathrm{Ly}\alpha}$ could theoretically mimic an evolution in absorption velocity with $W_{\mathrm{Ly}\alpha}$. However, despite the significantly smaller Lyα offsets among LAEs with respect to LBGs, no trend in $v_{\mathrm{Ly}\alpha}$ vs. $W_{\mathrm{Ly}\alpha}$ is seen in samples consisting solely of LAEs, and no trend is detected among the 35 LAEs with systematic redshifts in this sample. Furthermore, no evolution with $W_{\mathrm{Ly}\alpha}$ is seen in right-most edge of the low-ionization absorption (presumably corresponding to neutral interstellar gas at the systemic redshift) across the three panels of Fig. 4.12; such a shift would be expected from a $W_{\mathrm{Ly}\alpha}$-dependent estimator of the systemic redshift. Lastly, the total velocity width of absorption decreases significantly with increasing $W_{\mathrm{Ly}\alpha}$ across the three panels, suggesting the presence of a real correlation of Lyα equivalent width with outflow velocity among these faint LAEs.

---

[5] Note that the maximum absorption velocity is insensitive to any bias in the continuum level due to systematics in the background subtraction.

4.5.2 Lyα emission signatures

The Lyα emission profiles for each subsample (top panels of Fig. 4.12) show evidence for evolution in wind velocity with $W_{\mathrm{Ly}\alpha}$ as well. Each Lyα profile displays a narrow peak redward of the systemic redshift (by construction, as they are stacked on the basis of their peak Lyα redshifts) as well as an extended blue tail. This blue tail can be seen to broaden across the three panels of Fig. 4.12 with decreasing $W_{\mathrm{Ly}\alpha}$. To quantify this effect, a two-component Gaussian fit was performed to each stacked Lyα profile with the following form:

$$f_\lambda(v) = A_{\mathrm{blue}} e^{-(v+\Delta v/2)/2\sigma_{\mathrm{blue}}} + A_{\mathrm{red}} e^{-(v-\Delta v/2)/2\sigma_{\mathrm{red}}} + f_{0,\mathrm{cont}} \ , \tag{4.5}$$

such that the fit profile consists of two Gaussian peaks of arbitrary height and width, but with equal and opposite shifts with respect to systemic ($\pm\Delta v/2$). The model intentionally evokes an idealized outflow scenario in which the average LAE is surrounded by outflowing gas in both directions along the line of sight. In all three stacks, the red side of the Lyα profile diverges strongly from a Gaussian shape at large velocities, forming a broad red tail similar to that seen at $v \ll 0$. In order to maintain the simplicity of the model, the spectrum at $v > +500$ km s^{-1} was omitted from the fitting.

The resulting fits are displayed in Fig. 4.12, with fit parameters given in Table 4.5. Both the width of the blue component and the separation of the blue and red peaks increases with decreasing $W_{\mathrm{Ly}\alpha}$. While such an effect could partially be driven by a varying H I column density, the correspondence of the extended absorption and emission strongly indicates the role of outflowing gas in populating the wings of the Lyα emission profile.

4.5.3 Comparison to continuum-bright galaxies

While the trend of the outflow properties with $W_{\mathrm{Ly}\alpha}$ is fairly weak among the LAEs in this sample, we can probe a much larger range in galaxy properties by extending the sample to include continuum-bright galaxies. Several such spectroscopic samples have been collected as part of the KBSS and related surveys. In Fig. 4.13, we compare the stacked spectrum of all 316 LAEs in this sample with two stacks of LBGs, one from the KBSS-MOSFIRE (Steidel et al. 2014), and the other from a survey for Lyman-continuum (LyC) emission in $z \sim 3$ galaxies (C. Steidel et al., in prep.). Details of these two samples are given in Table 4.6.

The KBSS-MOSFIRE sample consists of 132 galaxies that each exhibit Lyα emission in their UV spectra and have redshifts measured via nebular emission lines. Most of these rest-UV spectra were observed using Keck/LRIS-B with the 400-line grism, providing a spectral resolution $R \sim 800$, or $\sigma_v \sim 160$ km s^{-1}. There is significantly more metal absorption in each of the spectral lines shown in Fig. 4.11, and the absorption profiles are both broader (extending to $v \approx -1000$ km s^{-1}) and deeper ($\lesssim 0.5\times$ the continuum value) with respect to the LAE stack. The excited fine-structure and nebular emission lines, however, are well-matched to the corresponding LAE features, further validating the redshift offset employed for the KBSS-Lyα stack.

The LyC survey sample consists of 123 galaxies without nebular redshifts; the redshifts for this sample

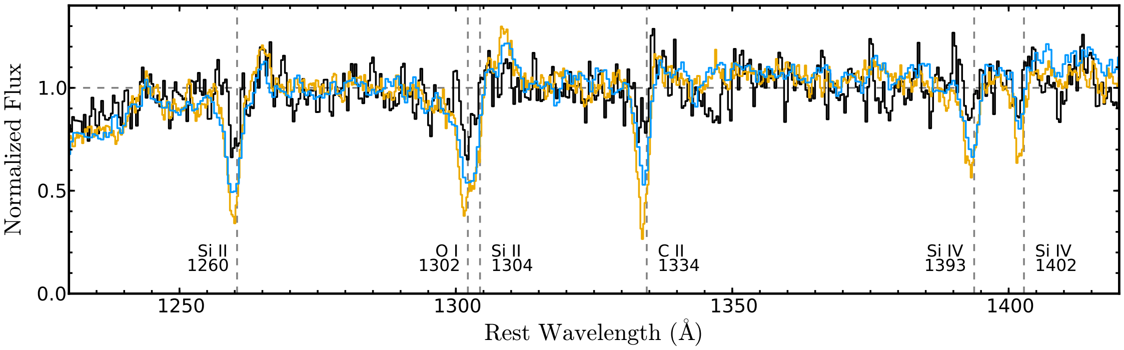

Figure 4.13: Composite UV continuum spectra for stacks of KBSS-Lyα LAEs and two comparison samples of LBGs. Details of the LBG samples are given in Table 4.6. The stacks are in f_ν normalized to the same continuum level. The LAE stack (black) is the same as that given in Fig. 4.11. The KBSS-MOSFIRE stack (blue) has $R \sim 800$, with all redshifts measured via nebular emission lines. The "LyC Survey" stack (orange) has $R \sim 1300$ (equal to that of the KBSS-Lyα spectra) and redshifts measured by a calibrated combination of Lyα emission and metal absorption redshifts. The absorption lines displayed in Fig. 4.11 are here marked by vertical dashed lines. Given the difference in resolution, the two LBG samples are highly consistent with each other and exhibit clear contrasts with the LAE sample, including significantly broader and deeper absorption profiles.

Table 4.6. LAE and LBG Comparison Samples

Sample	$\langle z \rangle$	m_{1450}[a]	M_{1450}[b]	$\langle W_{\mathrm{Ly}\alpha} \rangle$[c]	N_{obj}	$\lambda/d\lambda$	W_{1260}[d]	$f_{c,1260}$[e]	v_{1260} (km s^{-1})[f]
KBSS-Lyα	2.70	27.0	–18.7	42Å	316	1300	0.53Å	0.3	–100
KBSS-MOSFIRE	2.30	24.5	–20.9	16Å	132	800	1.50Å	0.5	–201
LyC Survey	3.05	24.6	–21.3	14Å	123	1300	1.73Å	0.7	–186

[a] m_{1450} is the observed AB magnitude corresponding to the rest-frame $\lambda \sim 1450$Å UV continuum. At $z \sim 2.7$ (KBSS-Lyα and KBSS-MOSFIRE), this correponds to the G band, whereas the $\mathscr{R}$ magnitude is used for the LyC survey sample at $z \sim 3$. For consistency with the other samples, the LAE m_{1540} value is not Lyα-subtracted, though the Lyα emission dominates the broadband flux in many cases.

[a] M_{1450} is the absolute magnitude corresponding to m_{1450} at the typical redshift of the sample $\langle z \rangle$.

[c] Because the LBG samples have no narrowband Lyα images, the values of $W_{\mathrm{Ly}\alpha}$ here were measured spectroscopically. For consistency, the spectroscopic Lyα equivalent width for our LAE stack is given as well; note that the average photometric value for this same sample is $\langle W_{\mathrm{Ly}\alpha} \rangle = 85.6$Å.

[d] W_{1260} is the absorption equivalent width measurement of Si II λ1260, the strongest unblended feature in the UV continuum of these three samples (Table 4.4, Fig. 4.11).

[e] $f_{c,1260}$ is the covering fraction of gas implied by the depth of the Si II λ1260 absorption trough.

[f] v_{1260} is the absorption-weighted velocity of the Si II λ1260 absorption trough.

were estimated via a combination of their Lyα emission and interstellar absorption redshifts with a calibration based on the results of Steidel et al. (2010) and Rakic et al. (2011). Furthermore, the composite spectrum was checked after stacking using stellar photospheric features. 10% of these galaxies have redshifts derived solely from the Lyα line and assume a 300 km s^{-1} offset. The correspondence of the absorption and emission signatures of the stack to those of the KBSS-MOSFIRE stack again demonstrates the efficacy of the calibration based on UV features. Furthermore, these spectra were observed using a 600-line grating that matches the resolution of the KBSS-Lyα sample, thereby allowing us to account for the effect of the lower resolution of the KBSS-MOSFIRE sample. The absorption profiles of the two LBG surveys are quite similar. The velocity extent of the absorption is almost identical in both samples ($v_{\rm max} \approx -1000$ km s^{-1}), though the LyC stack shows deeper absorption across all the lines. This difference is partially a result of the higher spectral resolution of the 600-line grism, but it may also signify a difference in the galaxy properties: at $z \sim 3$, the LyC galaxies have a brighter average rest-frame luminosity than those at $z \sim 2.3$ (which have similar observed magnitudes). The total equivalent width in absorption (represented by the equivalent width in Si II λ1260 in Table 4.6) is insensitive to the spectral resolution and is significantly greater for the LyC stack.

While the blending of Si II λ1304 with O I λ1302 again prevents a measurement of the Si II optical depth, Shapley et al. (2003) demonstrate that the Si II λ1260 transition is typically saturated in bright LBGs. Furthermore, the consistency of the absorption troughs among the low-ionization species in the LBG stacks suggests a gas covering fraction $f_c \sim 0.5-0.7$ in enriched, neutral low-ionization material for the two LBG samples. The line ratio of the Si IV doublet is $W_{1393}/W_{1402} \sim 2$ for both LBG stacks (as in Shapley et al. 2003), suggesting an optically-thin transition and $f_c \gtrsim 0.4$ for the ionized H II gas.

Through comparison of the LAE and LBG stacks, it seems clear that the qualitative links between Lyα emission and and interstellar absorption discussed in Shapley et al. (2003) persist down to far fainter continuum luminosities than those probed by samples of LBGs. The wind velocity (represented by either the absorption-weighted mean or the highest-velocity edge of absorption) decreases with increasing $W_{\rm Ly\alpha}$ across the LBG and LAE subsamples, and the covering fraction of gas drops steadily with increasing $W_{\rm Ly\alpha}$ to at least the intermediate subsample of LAEs ($W_{\rm Ly\alpha}$ ∼38Å). The offset of the Lyα emission likewise decreases from the LBG samples (∼300 km s^{-1}) to the LAE stacks.

However, many of these properties break down or become more complicated at high $W_{\rm Ly\alpha}$. While f_c is significantly lower among the LAEs than either sample of LBGs, there is only weak evolution of f_c with $W_{\rm Ly\alpha}$ among the subsamples of LAEs, particularly at $W_{\rm Ly\alpha} \gtrsim 20-60$Å. The absorption velocity correlates with the breadth of the extended Lyα emission wings in a two-component model, but neither the width of the narrow Lyα peak nor its offset from the systemic redshift seem to depend on either $W_{\rm Ly\alpha}$ or $v_{\rm abs}$. Erb et al. (2014, submitted) likewise find a strong relationship between $W_{\rm Ly\alpha}$ and Lyα offset velocity in a combined sample of LAEs and LBGs, but little or no relation among the Lyα-selected galaxies themselves. A clear determination of the physical origins and limits of these relationships awaits a more a more comprehensive characterization of the physical conditions within these LAEs (including further rest-optical spectra), but some general conclusions can already be drawn.

It seems obvious that the many factors which can drive Lyα production and escape each play a role in this process, and these roles likely vary with galaxy properties. The broad Lyα emission profiles with respect to those of the nebular emission lines Hα and [O III] demonstrate that the observed Lyα photons are significantly scattered before escaping these LAEs. The extent of the wings of the Lyα emission line are likely to be populated by scattering off of outflowing gas, and thus the wings are sensitive to the gas velocity, but the relatively low measured covering fractions of these outflows and the constancy of the Lyα peak offset may suggest that the majority of Lyα scatterings in LAEs occur without incurring a large wind-driven velocity offset. Such an effect would be likely in a scenario where galaxy-scale winds are highly anisotropic and thus create an orientation-dependent model for Lyα scattering and escape. The anisotropy of galaxy-scale winds is highly favored by simulations (e.g. Hopkins et al. 2012) and lower-redshift observations (e.g. Kornei et al. 2012), both of which suggest that outflows dominate along the axis perpindicular to galactic disks, but it is not clear whether the anisotropy of winds and that of Lyα emissivity coincide. Verhamme et al. (2012) suggest that the the Lyα flux and equivalent width are also maximized when a galaxy is observed face-on, but this would naively predict a positive correlation between Lyα velocity offset and equivalent width (rather than the negative or no correlation observed).

However, Law et al. (2009) find that galaxies at $z \sim 2-3$ are generally not rotationally-supported, and thus are less likely than low-redshift galaxies to generate coherent, collimated outflows. The young, faint populations of LAEs considered here are even less likely to maintain such structural coherence. Therefore, the KBSS-Lyα LAEs may be best modeled by irregular morphologies in which Lyα photons escape through a patchy ISM with minimal planar symmetry. Such a model, in which Lyα photons escape through "holes" in the neutral gas distribution, would similarly explain the strong association between Lyα and LyC emissivity (e.g. Mostardi et al. 2013). LBGs and other bright star-forming galaxies can have extremely low Lyα and LyC escape fractions even when low-resolution spectroscopy suggest that the gas covering fractions are < 1; in many cases, there may be extremely narrow, unresolved absorption components covering the line of sight that are still capable of absorbing all of the incident LyC flux (e.g. the galaxy Q0000-D6, as discussed by Shapley et al. 2003 and Giallongo et al. 2002). Only in the smaller galaxies with lower gas surface densities is it likely for a truly transparent window to penetrate the neutral ISM.

Furthermore, while the scattering of Lyα photons is driven by H I, the eventual absorption and destruction of these photons is dominated by dust. The apparent breakdown of the correlations of galaxy properties with $W_{\mathrm{Ly}\alpha}$ may indicate the transition to a regime where dust formation and mixing into the ISM has not fully progressed. The faintest LAEs at $z \sim 2-3$ may be most analogous to those observed at $z \sim 6$, where the extremely blue UV slopes suggest that escaping photons encounter very little dust while exiting the galaxy. More robust fitting of the LAE spectral energy distributions, including deep NIR images from MOSFIRE, could strongly constrain the dust content of these young galaxies. Similarly, deep NIR spectra may constrain the metallicity (and thus the chemistry) of their ISM.

Finally, the decoupling between Lyα emission and galaxy properties in this sample at the highest values of $W_{\rm Ly\alpha}$ may be the result of the QSO contribution to their Lyα flux. For fluorescently-illuminated systems, the total Lyα flux is proportional to the surface area of optically-thick H I and the strength of the local QSO-generated ionizing field Cantalupo et al. (2005); Kollmeier et al. (2010), with minimal dependence on the kinematic or chemical properties of the galaxies. Our forthcoming analysis of the *HST* NIR and optical images of these fields will shed more light on the physical sizes, morphologies, and stellar components of the Lyα-emitting regions of these galaxies.

4.6 Conclusions

This chapter has presented a comprehensive account of the properties of Lyα-emitters in the fields around hyperluminous QSOs at $z \sim 2.7$, taken from the KBSS-Lyα. This unique spectroscopic and photometric survey provides new insight into several diverse aspects of galaxy and black hole evolution at high redshift, which may be divided into several categories: the environments of the most luminous QSOs, the effect of these QSOs on their surrounding galaxies and gas, and the properties of faint, nascent galaxies.

Firstly, it is clear that the galaxy overdensities seen in LBGs by Trainor & Steidel (2012) extend to the continuum-faint population of LAEs. The luminosity function of LAEs is significantly boosted at all luminosities in the neighborhoods of HLQSOs compared to blank fields at similar redshifts. The redshift distribution of these objects also shows a strong association with the QSO redshift, with a distribution of velocities/redshifts comparable to that of LBGs (i.e. $\sigma_v \approx 500$ km s^{-1}). However, there is substantial diversity among the eight HLQSO fields considered here; both the luminosity function and redshift distributions show a range of properties, including some fields with little apparent association between the location of the QSO and that of the surrounding galaxies. Because LAE surveys are much more effective at selecting objects in a specific redshift window than LBG surveys, the galaxies included here may provide a much higher-fidelity probe of the HLQSO bias than the measurements of Trainor & Steidel (2012), given a suitably deep comparison sample of blank-field LAEs such as those collected by ongoing and forthcoming surveys.

Secondly, some properties of the LAEs appear to be strongly affected by the presence of the nearby QSO. Specifically, there are several characteristics of the LAEs that indicate a fluorescent contribution to their Lyα emission: the faint-end slope of the luminosity distribution is brighter than that seen in blank fields (and consistent with that seen in observations and simulations of bright QSO fields), while the distribution of Lyα equivalent widths, $W_{\rm Ly\alpha}$, shows an excess of sources with high values of $W_{\rm Ly\alpha}$ with respect to an exponential distribution. As discussed in Trainor & Steidel 2013, these high-$W_{\rm Ly\alpha}$ sources are preferentially associated with the foreground of the QSO, a natural prediction of fluorescent emission in the presence of a QSO with a lifetime of ~ 10 Myr. In addition, near-IR (rest-frame optical) spectra of these LAEs reveal that several of them have Lyα lines that are blueshifted with respect to their systemic redshifts, a property that is extremely rare in star-forming galaxies and may be associated with inflowing (rather than outflowing) gas. In order to avoid being dominated by outflows, such objects would likely have minimal star formation ("dark galaxies") and thus be uniquely observable under external, fluorescent illumination. These systemic redshift measurements further the conclusions of Trainor & Steidel (2013; Chapter 3) in suggesting that these QSO-associated LAE samples contain some of these "dark galaxies" that may provide new insight into the pre-stellar evolution of galaxies.

Lastly, despite the faint continuum luminosities and fluorescent illumination of these LAEs, they display many properties in line with expectations from their continuum-bright analogues. Like LBGs, faint LAEs show significant evidence for enriched, outflowing winds, though at significantly lower velocities and smaller covering fractions. Furthermore, the outflow velocity of these winds is inversely correlated with Lyα emission equivalent width even within the LAE sample. As the highest-$W_{\mathrm{Ly}\alpha}$ LAEs are associated with very little continuum emission, this correlation may indicate that the wind velocity is primarily dependent on the net star-formation rate, which is the dominant contributor to the UV continuum flux. In either case, these observations demonstrate that stellar feedback is an essential ingredient in realistic simulations of even the youngest, least massive galaxies at high redshift. Further work is necessary to analyze the apparent breakdown the relationships between $W_{\mathrm{Ly}\alpha}$ and covering fraction of ISM absorption at the highest equivalent widths. This effect may be the result of a qualitative transition in the properties of galaxies to those with minimal enrichment and dust, and could also point to the effect of the QSO in picking out galaxies independently of their star-formation rates.

In each of these topics, further progress will be driven by the continued near-IR observations of faint galaxy populations. Rest-frame optical spectra are the only way to effectively constrain the star-formation rates and metal enrichment of these newborn galaxies, thereby establishing a relationship between their stellar and gaseous properties and making a complete case for the presence of truly "dark" galaxies made visible by the reprocessed QSO light.

Acknowledgments

We are indebted to the staff of the W.M. Keck Observatory who keep the instruments and telescopes running effectively. We also wish to extend thanks to those of Hawaiian ancestry on whose sacred mountain we are privileged to be guests. This work has been supported in part by the US National Science Foundation through grants AST-0908805 and AST-1313472. RFT also acknowledges support from Dennis and Carol Troesh.

Chapter 5

Summary and Future Directions

This thesis has attempted to encompass a diverse set of astrophysical phenomena using an equally expansive range of observational tools. Using narrowband and broadband imaging from ground-based and space-based observatories, spectroscopy across the visible and near-infrared spectrum, and a variety of statistical tools, we have worked to characterize the complex interplay of black holes, galaxies, dark matter, and gas at high redshift. The unifying feature of the studies included herein is the laboratory in which they were conducted: the unique and rare regions around some of the brightest QSOs in the universe. Like any good laboratory, the QSO environments provide specialized tools unavailable in a typical corner of the universe: a high density of galaxy-QSO pairs, a bright background light for absorption studies, an illuminating source of ionizing radiation, and means of selecting large numbers of Lyα-emitting galaxies and gas with high efficiency.

Using these tools, we have demonstrated that the most luminous QSOs do not inhabit particularly unique or massive dark matter halos, but live in small group-like environments suitable for efficient merging and galaxy growth. We find that the local relationships between galaxy and black hole mass do not seem to apply to objects at these mass scales at high redshift, suggesting that the most massive black holes at $z \sim 3$ grow very little between that time and $z \sim 0$, despite residing in halos that must grow by orders of magnitude if they eventually fall onto these low-redshift relationships. Such an imbalanced QSO/galaxy growth history both before and after $z \sim 3$ is challenging for theories of black hole and galaxy accretion. These results are discussed at length in Chapter 2 (Trainor & Steidel 2012) and rely primarily on the distribution of continuum-bright galaxies (LBGs) near the QSO redshifts and optical photometry of the QSOs themselves, data that is taken from the Keck Baryonic Structure Survey (KBSS; Rudie et al. 2012).

In Chapters 3 & 4, we have used a new survey (KBSS-Lyα), conducted in large part for this thesis, to find and characterize hundreds of Lyα-emitters (LAEs) in these same QSO fields. Chapter 3 focuses on the utility of selecting individual LAEs with high values of the Lyα equivalent width, denoted by W_0, and using them as tracers of the QSO-generated ionizing emission field. While the small number of high-W_0 sources yield a relatively coarse measurement of the shape and scale of this field, they are suffient to constrain both the lifetime of the QSO ionizing phases and their isotropy. We find that the QSO lifetimes must be within a factor of ~ 2 of 10 Myr and that the ionizing emission must extend to large angles from the line of sight

($\gtrsim 30°$). These results provide further constraints on the accretion history of the supermassive black holes, demonstrating that they cannot (or at least, do not at $z \sim 3$) sustain Eddington-level accretion for the very long timescales required for exponential black hole growth.

Chapter 4 uses the KBSS-Lyα data to describe the properties of faint galaxies and the role the nearby QSO may play in both their detection and evolution. We find that the luminosity function and equivalent-width distribution are substantially different from non-QSO-associated LAE populations. This discrepancy is posited to be driven by a combination of the cosmologically biased environments of QSOs and the effect of the ionizing QSO flux that bathes the surrounding galaxies and gas. This ionizing radiation may likewise cause the detection of several sources in which the peak and flux-weighted average of the Lyα flux is blueshifted with respect to the systemic LAE redshift, an effect rarely seen in galaxy spectra, but theoretically associated with the emission from inflowing H I gas. When the total sample of LAE spectra are stacked, however, they reveal (on average) the presence of metal-enriched outflowing gas qualitatively similar to that seen ubiquitously around the brighter galaxies at similar redshifts. Whatever unique, gaseous objects are revealed by the QSO light in these samples, the bulk of the detected LAEs represent typical star-forming galaxies and therefore extend our knowledge of star formation and the concommitant stellar feedback to fainter, younger, and smaller galaxies than ever before at these redshifts.

Despite this progress, there is much work still to be done. Many related theoretical and observational efforts are already coming to fruition through advances in technique and technology. On the theoretical side, numerical hydrodynamical simulations of stellar and black-hole driven feedback are coming ever closer to reproducing the signatures of feedback seen in high-redshift galaxy spectra and the local galaxy mass function. Stellar feedback, in particular, is experiencing a transformative renaissance through simulations at scales ranging from stellar atmospheres to cosmological volumes. While a detailed understanding of black hole accretion and the coupling of the related energetics to galaxy formation is still forthcoming, substantial brain- and CPU-power is being devoted to a physically-motivated, observationally-consistent model for AGN and stellar feedback , and progress must soon be forthcoming. The author[1] of this thesis is fortunate to be moving from one institution[2] working to tackle these theoretical isses to another[3] equally involved. A synthesis of simulation-derived insight and observational data will be necessary to unlock the puzzles of galaxy and black hole evolution, and the author looks forward to continued collaboration to these ends.

Of course, much of our understanding of galaxy and black hole growth must come from observations at high redshift, and new technology is driving substantial progress in this realm as well. New observatories spanning sub-mm wavelengths (the Atacama Large Millimeter Array; ALMA) to high-energy x-rays (the Nuclear Spectroscopic Telescope Array; NuSTAR) are providing new insights into the growth of stars and black holes at low- and high-redshifts, while the future Thirty-Meter Telescope and James Webb Space Telescope will push galaxy evolution into yet younger, fainter, and more distant galaxy populations. However,

---

[1] Ryan Trainor

[2] Caltech

[3] UC Berkeley, as a Miller Fellow

some of the most exciting technological advancements are occuring at the increasingly-venerable W. M. Keck Observatory and Palomar Observatory. Near-IR spectra from Keck/MOSFIRE are included in this thesis, and future observations will make systemic redshift determinations feasible for the first time among large samples of faint, high-redshift galaxies. As demonstrated in Chapter 4, these precise redshift measurements are crucial for understanding the kinematic properties of forming galaxies, including the inflows and outflows by which they feed star-formation and enrich their surrounding intergalactic and circumgalactic media.

Furthermore, the extension of the KBSS into the KBSS-MOSFIRE (Steidel et al. 2014) has already demonstrated the complexity of the chemical and physical properties of interstellar gas in high-redshift galaxies. Indeed, $z \sim 2-3$ LBGs occupy an almost completely disjoint region of the phase space defined by strong emission lines with respect to local galaxies, suggesting substantial evolution in the temperature, ionization state, and metallicity of H II regions since $z \sim 3$. The establishment of the high-redshift mass-metallicity relation (MZR), an essential tool for matching hydrodynamical simulations to the real universe, depends critically on a thorough understanding of the correspondence of these measurements to the physical properties of the gas. New models for stellar properties, including rapidly rotating massive stars that may dominate the ionizing radiation field of high-redshift galaxies (Eldridge & Stanway 2009; de Mink et al. 2013), are likely to play a role, but hydrodynamical simulations and larger samples of galaxies encompassing a broader range of physical properties, such as LAEs, will be necessary to understand the evolution of galaxy properties with age, mass, metallicity, and redshift.

Another ongoing technical revolution involves the development of wide-area integral-field spectrometers for large telescopes. While effective at identifying line emission at specific, predefined wavelengths in the observed frame, narrowband photometry is inefficient for identifying LAEs surrounding targets that span broad ranges of redshift. Wide-area integral-field spectrographs such as the Cosmic Web Imager (CWI) at Palomar Observatory and the upcoming Keck Cosmic Web Imager (KCWI) provide a much more flexible mechanism for such a survey by simultaneously measuring the redshift and position of LAEs over a relatively broad range of redshift in a single exposure. For instance, the blue grating of CWI can measure a 150–450Å spectral slice anywhere between 4500Å and 5400Å in rest-frame wavelength, allowing it to detect Lyα emission for $2.70 < z < 3.44$ with a redshift resolution ∼100x finer than narrowband surveys.

IFU observations produce a datacube with two spatial dimensions and one of wavelength; the spaxels can then be integrated over small slices of the wavelength dimension to produce narrowband images with effective band-passes far smaller than those achievable through physical filter fabrication. Similarly, spaxels may be combined in the spatial direction in order to increase the signal-to-noise ratio in the spectra of extended objects, such as those often seen in Lyα surveys (Steidel et al. 2000; Matsuda et al. 2011). In particular, QSOs have long been known to be associated with extended nebulosities visible in emission lines (e.g. Balick & Heckman 1979; McCarthy et al. 1987), and such extended emission is clearly visible in many of our narrowband Lyα images of the HLQSO fields. One of the HLQSO fields in our LAE survey (HS1549+1919) has already been observed with CWI (Martin et al. 2014, submitted), and the results reveal filamentary Lyα

emission with a complex velocity structure extending beyond the 130 kpc virial radius of the $M_h \sim 10^{12.5}$ $M_\odot$ dark matter halo. This extended emission is likely to be a combination of QSO-induced fluorescence and/or gravitational cooling radiation from the infalling gaseous filaments predicted by simulations of gas accretion onto halos (e.g. Rosdahl & Blaizot 2012). In either case, the gas flows that presumably feed star-formation and black hole growth are revealed in these data in the context of the extreme ionizing field of the QSO (more than 10^4 times the metagalactic UV background on virial scales). The effect of QSO emission on infalling gas has direct consequences for the effectiveness of AGN feedback in modulating galaxy and black-hole growth, and the physics affecting these uniquely energetic HLQSO systems is likely to be relevant at a scaled-down level in the hosts of lower-luminosity QSOs. Several other HLQSOs in our KBSS sample lie at suitable redshifts for CWI observations, including one with no previous Lyα imaging, and observations in these fields would build upon the existing HS1549+1919 data in quantifying the potentially diverse demographics of gaseous QSO environments.

In addition to targeting optically-bright HLQSOs, an exciting possibility exists in the detection of Lyα emission around obscured QSOs at high redshift. The largely-successful unified model of AGN suggests that obscuration is primarily a function of QSO inclination, but there are hints that many obscured and reddened QSOs may represent a younger, more massive, and/or more actively star-forming population (e.g. Glikman et al. 2012; Hickox et al. 2011; Sanders et al. 1988, respectively). Comparing the gaseous environments of these systems to unobscured QSOs could constrain the lifecycle of black hole feeding, obscuration, and feedback. Furthermore, the detection of fluorescent emission around obscured QSOs would provide a means of measuring their ionizing field perpendicular to our line of sight, thus providing a direct test of anisotropic AGN unification models. The selection of QSOs independently of obscuration is now possible with mid-IR photometry from the Wide-field Infrared Survey Explorer (WISE; Wright et al. 2010). For instance, Bridge et al. (2013) find a population optically-faint, MIR-red sources at $1.6 < z < 4.6$ that show strong evidence of luminous, obscured AGN activity and extended Lyα emission. The gaseous environments and ionizing fields of such high-redshift obscured systems are completely unexplored, and the new capabilities of CWI and KCWI can provide the first glimpses of their physics and geometries.

All together, the future is bright (as bright as an HLQSO, figuratively speaking?) for the study of faint galaxies, luminous black holes, and a cohesive picture of the astrophysical processes that drive their co-evolution. With so many computational and observational tools, as well as experienced minds, at our disposal, it is tempting to think that there will be little left to discover by the time the next generation of astrophysicists (perhaps including the author himself) reaches maturity. History, of course, tells a different story. The results of Schmidt (1963) and Steidel et al. (2014), to name but two, must lead us to conclude that each mystery solved brings as many questions as answers, providing material for many more telescopes, theses, and curious minds to come. We look forward to the challenge.

Appendix A

MOSFIRE

A.1 Instrument Summary

Some of the most interesting results and future plans of Chapters 4 and 5 rely on data from the new Multi-Object Spectrometer For Infra-Red Exploration (MOSFIRE), so it seems prudent to describe some of the unique and powerful capabilities of that instrument here. Furthermore, the MOSFIRE project comprised an intermittent, but significant, component of the author's work for the first few years of his PhD, so this appendix will provide a written record of his contributions to the project. Detailed information on the design, technical specifications, and as-built performance of MOSFIRE are given in McLean et al. (2010) and McLean et al. (2012), but a summary will follow here.

MOSFIRE is a wide-field ($6.1' \times 6.1'$) near-infrared (NIR) spectrometer and imager that covers the Y, J, H, and K (or K_s) bands for a total observed wavelength range $0.97\mu\mathrm{m} < \lambda < 2.41\mu\mathrm{m}$. It sits at the Cassegrain focus of the Keck 1 telescope at the W. M. Keck Observatory on Mauna Kea, Hawaii. The concept and specifications of the instrument were designed to be an ideal complement to the optical wavelength ($0.3-1\mu$m) Low Resolution Imaging Spectrometer (LRIS; Oke et al. 1995; Steidel et al. 2004), also at the Cassegrain focus of Keck 1. The two instruments share similar field sizes and multi-object capabilities, enabling combined imaging and spectroscopic surveys (such as those of this thesis) covering nearly an order of magnitude in wavelength space.

Understanding the profound scientific advancements enabled by the MOSFIRE instrument requires a description of several key technological improvements over previous NIR spectrometers. Firstly, MOSFIRE detector consists of a state-of-the-art Teledyne Hawaii 2RG 2K$\times$2K HgCdTe array, which provides an unprecedentedly low dark current ($<$0.008 e$^-$/s/pix over a typical 1800 s exposure) and low read noise (4.9 e$^-$ rms for 16 Fowler-sampled read pairs). The low noise characteristics of the detector allow background-limited observations even in short exposures, significantly improving the sky-subtraction capabilities of the instrument. Secondly, the spectral resolution ($R \sim 3500$) is optimized to resolve the night-sky lines (OH) that blanket the NIR bands, particularly in H. This high resolution produces an extremely faint sky background between the lines, estimated to be $\sim$2.7 magnitudes fainter than the broadband integrated sky background in

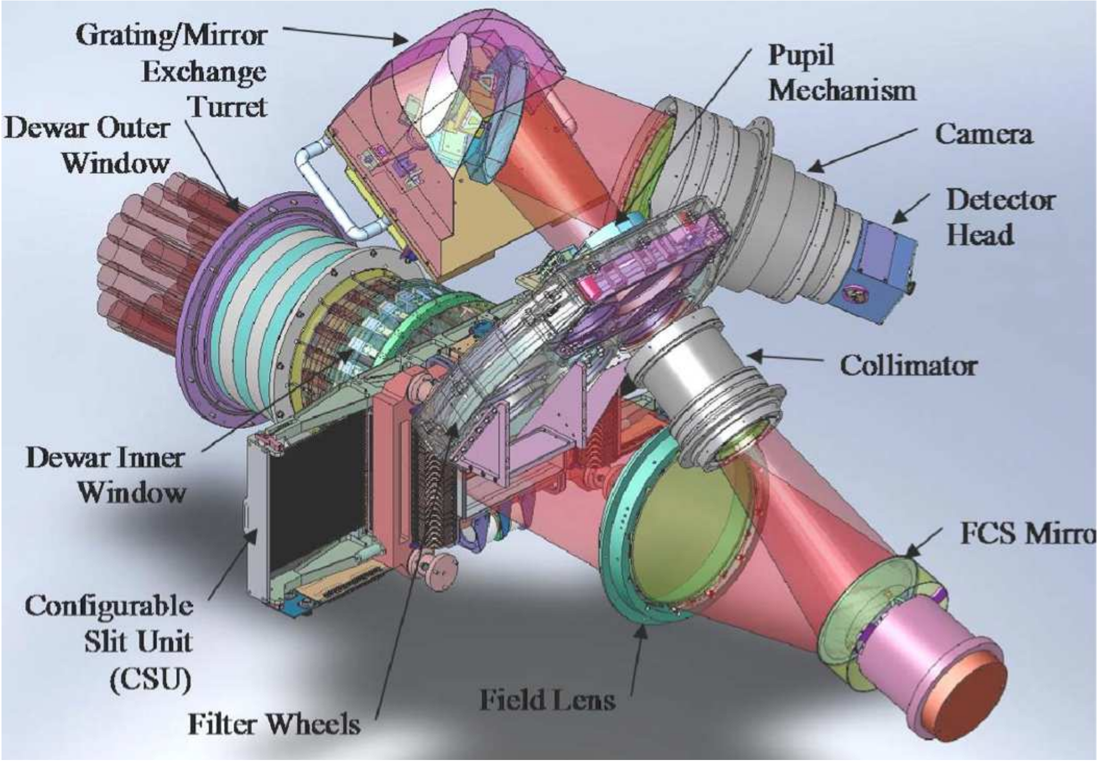

Figure A.1: The internal optical layout of MOSFIRE (reproduced from McLean et al. 2010). Physical components are labeled, including the flexure compensation system (FCS) mirror and the unique configurable slit unit (CSU).

H. These two capabilities give MOSFIRE an efficiency that is $\sim 5-10\times$ that of the previous generation of NIR spectrometers for individual objects.

Perhaps the most significant improvement of MOSFIRE over previous NIR spectrometers is its multiplexing capability: MOSFIRE can observe up to 46 objects simultaneously on individual slits. This capacity is due to a unique configurable, cryogenic slit unit (CSU) developed by the Swiss Centre for Micro-Electronics (CSEM). The CSU covers the field of view with 92 roboticized bars, paired to produce up to 46 slits of arbitrary width and location along the dispersion axis, or withdrawn completely in the imaging mode.[1] Each bar subtends $7''$ perpindicular to the dispersion axis, and adjacent bars may be combined to form longer slits up to the entire length of the field. The primary utility of this unit is to enable the configuration of masks without temperture-cycling the instrument, which is embeded in a 120 K cryostat. Typical observations of extragalactic fields include $\sim 25-30$ object per mask. Combined with the increased sensitivity for individual object spectra, the multiplexing capabilities of MOSFIRE produce an overall increase in survey efficiency of $\sim 150-300\times$ over previous NIR spectrometers, a transformative advantage for accumulating large numbers of faint object spectra and enabling ambitious surveys such as the KBSS-MOSFIRE (Steidel et al. 2014).

As described above, the ability to take short exposures (typically $\sim$120 s in the H band) is crucial for optimal sky subtraction because of the short timescale of variation in the OH line background. This means that faint objects require many ($\gtrsim$30) exposures that must be stacked without reference to the detection of flux from the science targets, which typically are undetected in individual exposures. Because of this requirement, the pixel position of objects on the detector must be highly repeatable among many exposures. Furthermore, the location of an object on the detector must be highly predictable in order for flat-field calibrations obtained during the afternoon or morning to be appropriately applied to observations taken during the night. MOSFIRE is attached to the moving Keck 1 mirror assembly at the Cassegrain focus, and it suffers significant internal flexure as a result of the varying gravity vector over the course of extended observations. In order to predict and maintain the position of a science object on the detector, a tip-tilt flexure compensation system (FCS) was designed and calibrated to correct for this flexure at nearly all potential telescope and instrument orientations. The modeling of this flexure and calibration of the FCS was the principle contribution of the author of this thesis to the MOSFIRE project, and this process is described below.

A.2 Flexure Modeling and Correction

The FCS consists of a round flat mirror backed by piezo transducers that lies along the optical path (Fig. A.1). By flexing one or more of the piezo transducers, the mirror provides tip/tilt control over the optical beam in order to compensate for deflections caused by the the shifting of optical components under gravity. As the gravity vector is uniquely determined by the elevation angle of the telescope (EL) and rotator angle of the instrument (ROT), the FCS operates via an open loop in which the tip/tilt correction necessary at any

---

[1] In the imaging mode, the grating turret is also rotated so that the optical path includes a flat mirror rather than a dispersion grating.

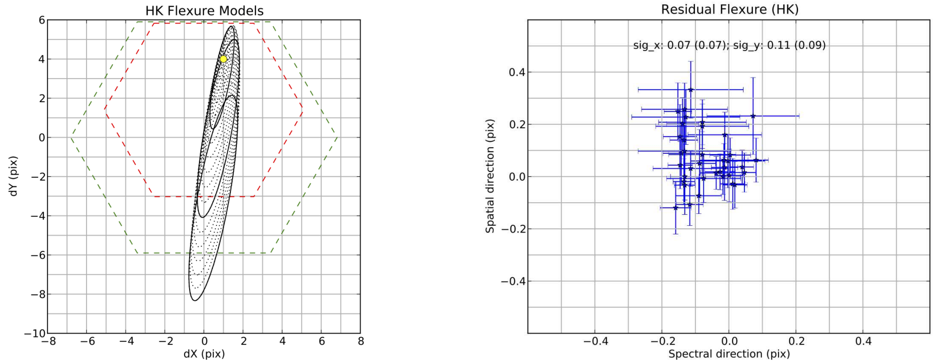

Figure A.2: *Left:* The modeled flexure in the HK spectroscopic grating mode as calibrated during MOSFIRE commissioning in March 2012. The yellow dot is the fiducial location of a slit image on the detector with the telescope pointed at zenith (EL = 90°). The black curves show the deflected (uncorrected) position of a slit on the detector with respect to its fiducial zenith location; each curve corresponds to a 360° rotation of the instrument in ROT at a fixed EL value. Dashed curved show 5° increments in EL, while solid curves are given for 30° increments. The green hexagon shows the correctable range of flexure due to the three-piezo FCS mirror. All black curves for EL $>$ 22° fall within the correctable range. The red hexagon shows the potential effect of a reduced piezo range, in which case the ability to corre at lower EL angles would be compromised. *Right:* Residuals to the corrected flexure deflections with the FCS turned on, again in HK spectroscopic mode. Black stars denote the mean deflection of an image determined by averaging the deflections of slits across the entire field; error bars show the rms dispersion among these slit deflections. The mean residuals have an rms dispersion of 0.07 pixels in the dispersion (X) direction and 0.11 pixels in the spatial (Y) dimension, of order the slit-to-slit variations in deflection (0.07 pixels and 0.09 pixels, respectively).

instrument orientation is computed from the modeled two-dimensional flexure function, parameterized by (EL, ROT).

In order to model the instrument flexure, a slit mask was designed to create small illuminated slits across the entire detector. Images were then taken of this slit mask in a grid of values in (EL, ROT) space. A python script was used to automatically measure the position of each illuminated slit on the mask and compare these positions to a fiducial reference image. The field-averaged movements of the slit images as a function of instrument orientation thus define the two dimensional deflection of the optical axis between the CSU and the detector planes.

The measured flexure at the detector plane was found to vary among the imaging and spectroscopic modes in a complex manner. This effect was not wholly unexpected, given that flexure can occur both before and after the dispersion grating, and the apparent flexure that occurs prior to the grating along the optical axis is affected by an anamorphic stretch/compression factor in the dispersion direction in the pixel coordinates of the detector. Because of these effects, the flexure was calibrated independently in the imaging mode and in both spectroscopic grating positions.[2]

After initial lab measurements of these deflections, it was determined that the internal instrument flexure exhibited very little hysteresis; that is, the measured deflection was solely a function of instrument orientation

---

[2] MOSFIRE uses a single dispersion grating with two positions for spectroscopy, one of which is used for Y and J band spectroscopy while the other is used for H and K spectroscopy. For a given grating configuration, a band is chosen via an order-sorting filter.

Figure A.3: The author (green jacket, determined face) working on MOSFIRE (blue, large) during commissioning at the summit of Mauna Kea. He has since lost the jacket, which had previously been one of his favorites. In the background is the assembly for attaching MOSFIRE to the Cassegrain focus of Keck 1.

with minimal dependence on the direction of rotation or the previous instrument orientation. Furthermore, the flexure exhibited highly elastic behavior (i.e. a linear stress-strain curve) such that the measured flexure in the x-y plane of the detector traced an ellipse when either EL or ROT was turned through an entire 360° rotation with the other angle held constant (Fig. A.2). Because of this ideal flexure behavior, the flexure model was able to be parameterized as a simple analytic function of (EL, ROT). The total uncorrected flexure in the detector plane was found to be ~ 14 pixels peak-to-peak for values of EL > 0, slightly exceeding the 11.8 pixel range of the piezo mirror. However, the flexure is correctable for any instrument orientation with EL $>$ 22°, corresponding to all possible science observations with airmass less than 2.67. While the flexure is not fully correctable within a $\sim 80°$ range of ROT at EL = 0, the judicious choice of a horizon stow orientation (with EL = 0 and the CSU bars horizontal) ensures that calibration images made in the stow position may be obtained with full flexure compensation.

After initial lab testing and modeling, the final parameters of the flexure function were calibrated prior to instrument commisioning on site at Keck 1 over a three-day period (21-23 March 2012; Fig. A.3). The final, FCS-corrected flexure residuals were found to be $\sim$0.1 pixel rms (Fig. A.2, right panel), in line with the instrument design specifications.

Bibliography

Adelberger, K. L. 2005, ApJ, 621, 574

Adelberger, K. L., Shapley, A. E., Steidel, C. C., Pettini, M., Erb, D. K., & Reddy, N. A. 2005a, ApJ, 629, 636

Adelberger, K. L. & Steidel, C. C. 2005a, ApJ, 630, 50

—. 2005b, ApJ, 627, L1

Adelberger, K. L., Steidel, C. C., Kollmeier, J. A., & Reddy, N. A. 2006, ApJ, 637, 74

Adelberger, K. L., Steidel, C. C., Pettini, M., Shapley, A. E., Reddy, N. A., & Erb, D. K. 2005b, ApJ, 619, 697

Adelberger, K. L., Steidel, C. C., Shapley, A. E., Hunt, M. P., Erb, D. K., Reddy, N. A., & Pettini, M. 2004, ApJ, 607, 226

Adelberger, K. L., Steidel, C. C., Shapley, A. E., & Pettini, M. 2003, ApJ, 584, 45

Anderson, T. W. & Darling, D. A. 1954, Journal of the American Statistical Association, 49, 765

Balick, B. & Heckman, T. 1979, AJ, 84, 302

Behroozi, P. S., Wechsler, R. H., & Conroy, C. 2013, ApJ, 770, 57

Berlind, A. A. & Weinberg, D. H. 2002, ApJ, 575, 587

Best, P. N., Kauffmann, G., Heckman, T. M., Brinchmann, J., Charlot, S., Ivezić, Ž., & White, S. D. M. 2005, MNRAS, 362, 25

Booth, C. M. & Schaye, J. 2010, MNRAS, 405, L1

—. 2011, MNRAS, 413, 1158

Bridge, C. R., Blain, A., Borys, C. J. K., Petty, S., Benford, D., Eisenhardt, P., Farrah, D., Griffith, R. L., Jarrett, T., Lonsdale, C., Stanford, S. A., Stern, D., Tsai, C.-W., Wright, E. L., & Wu, J. 2013, ApJ, 769, 91

Bullock, J. S., Kolatt, T. S., Sigad, Y., Somerville, R. S., Kravtsov, A. V., Klypin, A. A., Primack, J. R., & Dekel, A. 2001, MNRAS, 321, 559

Burbidge, G. 1967, Quasi-stellar objects (San Francisco: W.H.Freeman)

Cantalupo, S., Lilly, S. J., & Haehnelt, M. G. 2012, MNRAS, 425, 1992

Cantalupo, S., Lilly, S. J., & Porciani, C. 2007, ApJ, 657, 135

Cantalupo, S., Porciani, C., Lilly, S. J., & Miniati, F. 2005, ApJ, 628, 61

Chonis, T. S., Blanc, G. A., Hill, G. J., Adams, J. J., Finkelstein, S. L., Gebhardt, K., Kollmeier, J. A., Ciardullo, R., Drory, N., Gronwall, C., Hagen, A., Overzier, R. A., Song, M., & Zeimann, G. R. 2013, ApJ, 775, 99

Ciardullo, R., Gronwall, C., Wolf, C., McCathran, E., Bond, N. A., Gawiser, E., Guaita, L., Feldmeier, J. J., Treister, E., Padilla, N., Francke, H., Matković, A., Altmann, M., & Herrera, D. 2012, ApJ, 744, 110

Coil, A. L., Hennawi, J. F., Newman, J. A., Cooper, M. C., & Davis, M. 2007, ApJ, 654, 115

Condon, J. J., Cotton, W. D., Greisen, E. W., Yin, Q. F., Perley, R. A., Taylor, G. B., & Broderick, J. J. 1998, AJ, 115, 1693

Conroy, C. & White, M. 2013, ApJ, 762, 70

Cowie, L. L. & Hu, E. M. 1998, AJ, 115, 1319

Croom, S. M., Boyle, B. J., Shanks, T., Smith, R. J., Miller, L., Outram, P. J., Loaring, N. S., Hoyle, F., & da Ângela, J. 2005, MNRAS, 356, 415

Croom, S. M., Richards, G. T., Shanks, T., Boyle, B. J., Strauss, M. A., Myers, A. D., Nichol, R. C., Pimbblet, K. A., Ross, N. P., Schneider, D. P., Sharp, R. G., & Wake, D. A. 2009, MNRAS, 399, 1755

Croom, S. M., Smith, R. J., Boyle, B. J., Shanks, T., Miller, L., Outram, P. J., & Loaring, N. S. 2004, MNRAS, 349, 1397

Croton, D. J., Springel, V., White, S. D. M., De Lucia, G., Frenk, C. S., Gao, L., Jenkins, A., Kauffmann, G., Navarro, J. F., & Yoshida, N. 2006, MNRAS, 365, 11

da Ângela, J., Shanks, T., Croom, S. M., Weilbacher, P., Brunner, R. J., Couch, W. J., Miller, L., Myers, A. D., Nichol, R. C., Pimbblet, K. A., de Propris, R., Richards, G. T., Ross, N. P., Schneider, D. P., & Wake, D. 2008, MNRAS, 383, 565

Davis, M., Faber, S. M., Newman, J., Phillips, A. C., Ellis, R. S., Steidel, C. C., Conselice, C., Coil, A. L., Finkbeiner, D. P., Koo, D. C., Guhathakurta, P., Weiner, B., Schiavon, R., Willmer, C., Kaiser, N., Luppino,

G. A., Wirth, G., Connolly, A., Eisenhardt, P., Cooper, M., & Gerke, B. 2003, in Society of Photo-Optical Instrumentation Engineers (SPIE) Conference Series, Vol. 4834, Society of Photo-Optical Instrumentation Engineers (SPIE) Conference Series, ed. P. Guhathakurta, 161–172

de Mink, S. E., Langer, N., Izzard, R. G., Sana, H., & de Koter, A. 2013, ApJ, 764, 166

Decarli, R., Falomo, R., Treves, A., Labita, M., Kotilainen, J. K., & Scarpa, R. 2010, MNRAS, 402, 2453

Donoso, E., Yan, L., Stern, D., & Assef, R. J. 2013, ArXiv e-prints

Dunlop, J. S., McLure, R. J., Kukula, M. J., Baum, S. A., O'Dea, C. P., & Hughes, D. H. 2003, MNRAS, 340, 1095

Eisenstein, D. J., Weinberg, D. H., Agol, E., Aihara, H., Allende Prieto, C., Anderson, S. F., Arns, J. A., Aubourg, É., Bailey, S., Balbinot, E., & et al. 2011, AJ, 142, 72

Eldridge, J. J. & Stanway, E. R. 2009, MNRAS, 400, 1019

Erb, D. K., Steidel, C. C., Shapley, A. E., Pettini, M., Reddy, N. A., & Adelberger, K. L. 2006, ApJ, 646, 107

Ferrarese, L. 2002, ApJ, 578, 90

Ferrarese, L. & Merritt, D. 2000, ApJ, 539, L9

Gebhardt, K., Bender, R., Bower, G., Dressler, A., Faber, S. M., Filippenko, A. V., Green, R., Grillmair, C., Ho, L. C., Kormendy, J., Lauer, T. R., Magorrian, J., Pinkney, J., Richstone, D., & Tremaine, S. 2000, ApJ, 539, L13

Giallongo, E., Cristiani, S., D'Odorico, S., & Fontana, A. 2002, ApJ, 568, L9

Giavalisco, M., Koratkar, A., & Calzetti, D. 1996, ApJ, 466, 831

Glikman, E., Urrutia, T., Lacy, M., Djorgovski, S. G., Mahabal, A., Myers, A. D., Ross, N. P., Petitjean, P., Ge, J., Schneider, D. P., & York, D. G. 2012, ApJ, 757, 51

Gonçalves, T. S., Steidel, C. C., & Pettini, M. 2008, ApJ, 676, 816

Gould, A. & Weinberg, D. H. 1996, ApJ, 468, 462

Greene, J. E., Peng, C. Y., & Ludwig, R. R. 2010, ApJ, 709, 937

Gronwall, C., Ciardullo, R., Hickey, T., Gawiser, E., Feldmeier, J. J., van Dokkum, P. G., Urry, C. M., Herrera, D., Lehmer, B. D., Infante, L., Orsi, A., Marchesini, D., Blanc, G. A., Francke, H., Lira, P., & Treister, E. 2007, ApJ, 667, 79

Guaita, L., Gawiser, E., Padilla, N., Francke, H., Bond, N. A., Gronwall, C., Ciardullo, R., Feldmeier, J. J., Sinawa, S., Blanc, G. A., & Virani, S. 2010, ApJ, 714, 255

Hashimoto, T., Ouchi, M., Shimasaku, K., Ono, Y., Nakajima, K., Rauch, M., Lee, J., & Okamura, S. 2013, ApJ, 765, 70

Hayes, M., Östlin, G., Schaerer, D., Mas-Hesse, J. M., Leitherer, C., Atek, H., Kunth, D., Verhamme, A., de Barros, S., & Melinder, J. 2010, Nature, 464, 562

Hennawi, J. F. & Prochaska, J. X. 2013, ApJ, 766, 58

Hennawi, J. F., Strauss, M. A., Oguri, M., Inada, N., Richards, G. T., Pindor, B., Schneider, D. P., Becker, R. H., Gregg, M. D., Hall, P. B., Johnston, D. E., Fan, X., Burles, S., Schlegel, D. J., Gunn, J. E., Lupton, R. H., Bahcall, N. A., Brunner, R. J., & Brinkmann, J. 2006, AJ, 131, 1

Hickox, R. C., Myers, A. D., Brodwin, M., Alexander, D. M., Forman, W. R., Jones, C., Murray, S. S., Brown, M. J. I., Cool, R. J., Kochanek, C. S., Dey, A., Jannuzi, B. T., Eisenstein, D., Assef, R. J., Eisenhardt, P. R., Gorjian, V., Stern, D., Le Floc'h, E., Caldwell, N., Goulding, A. D., & Mullaney, J. R. 2011, ApJ, 731, 117

Hogan, C. J. & Weymann, R. J. 1987, MNRAS, 225, 1P

Hopkins, P. F., Hernquist, L., Cox, T. J., & Kereš, D. 2008, ApJS, 175, 356

Hopkins, P. F., Quataert, E., & Murray, N. 2012, MNRAS, 421, 3522

Jakobsen, P., Jansen, R. A., Wagner, S., & Reimers, D. 2003, A&A, 397, 891

Kelly, B. C., Vestergaard, M., Fan, X., Hopkins, P., Hernquist, L., & Siemiginowska, A. 2010, ApJ, 719, 1315

Kennicutt, Jr., R. C. 1998, ARA&A, 36, 189

Kereš, D., Katz, N., Weinberg, D. H., & Davé, R. 2005, MNRAS, 363, 2

Kollmeier, J. A., Zheng, Z., Davé, R., Gould, A., Katz, N., Miralda-Escudé, J., & Weinberg, D. H. 2010, ApJ, 708, 1048

Kormendy, J. & Bender, R. 2011, Nature, 469, 377

Kornei, K. A., Shapley, A. E., Erb, D. K., Steidel, C. C., Reddy, N. A., Pettini, M., & Bogosavljević, M. 2010, ApJ, 711, 693

Kornei, K. A., Shapley, A. E., Martin, C. L., Coil, A. L., Lotz, J. M., Schiminovich, D., Bundy, K., & Noeske, K. G. 2012, ApJ, 758, 135

Krumpe, M., Miyaji, T., & Coil, A. L. 2010, ApJ, 713, 558

Kulas, K. R., McLean, I. S., Shapley, A. E., Steidel, C. C., Konidaris, N. P., Matthews, K., Mace, G. N., Rudie, G. C., Trainor, R. F., & Reddy, N. A. 2013, ApJ, 774, 130

Kulas, K. R., Shapley, A. E., Kollmeier, J. A., Zheng, Z., Steidel, C. C., & Hainline, K. N. 2012, ApJ, 745, 33

Landy, S. D. & Szalay, A. S. 1993, ApJ, 412, 64

Langston, G. I., Heflin, M. B., Conner, S. R., Lehar, J., Carilli, C. L., & Burke, B. F. 1990, ApJS, 72, 621

Larson, D., Dunkley, J., Hinshaw, G., Komatsu, E., Nolta, M. R., Bennett, C. L., Gold, B., Halpern, M., Hill, R. S., Jarosik, N., Kogut, A., Limon, M., Meyer, S. S., Odegard, N., Page, L., Smith, K. M., Spergel, D. N., Tucker, G. S., Weiland, J. L., Wollack, E., & Wright, E. L. 2011, ApJS, 192, 16

Law, D. R., Steidel, C. C., Erb, D. K., Larkin, J. E., Pettini, M., Shapley, A. E., & Wright, S. A. 2009, ApJ, 697, 2057

Law, D. R., Steidel, C. C., Shapley, A. E., Nagy, S. R., Reddy, N. A., & Erb, D. K. 2012, ApJ, 745, 85

Lidz, A., Hopkins, P. F., Cox, T. J., Hernquist, L., & Robertson, B. 2006, ApJ, 641, 41

Lowenthal, J. D., Hogan, C. J., Green, R. F., Caulet, A., Woodgate, B. E., Brown, L., & Foltz, C. B. 1991, ApJ, 377, L73

Lynden-Bell, D. 1969, Nature, 223, 690

Magorrian, J., Tremaine, S., Richstone, D., Bender, R., Bower, G., Dressler, A., Faber, S. M., Gebhardt, K., Green, R., Grillmair, C., Kormendy, J., & Lauer, T. 1998, AJ, 115, 2285

Martini, P. 2004, Coevolution of Black Holes and Galaxies, 169

Massey, P., Strobel, K., Barnes, J. V., & Anderson, E. 1988, ApJ, 328, 315

Matsuda, Y., Yamada, T., Hayashino, T., Yamauchi, R., Nakamura, Y., Morimoto, N., Ouchi, M., Ono, Y., Kousai, K., Nakamura, E., Horie, M., Fujii, T., Umemura, M., & Mori, M. 2011, MNRAS, 410, L13

Matthews, T. A., Morgan, W. W., & Schmidt, M. 1964, ApJ, 140, 35

McCarthy, P. J., Spinrad, H., Djorgovski, S., Strauss, M. A., van Breugel, W., & Liebert, J. 1987, ApJ, 319, L39

McIntosh, D. H., Rix, H.-W., Rieke, M. J., & Foltz, C. B. 1999, ApJ, 517, L73

McLean, I. S., Steidel, C. C., Epps, H., Matthews, K., Adkins, S., Konidaris, N., Weber, B., Aliado, T., Brims, G., Canfield, J., Cromer, J., Fucik, J., Kulas, K., Mace, G., Magnone, K., Rodriguez, H., Wang, E., & Weiss, J. 2010, in Society of Photo-Optical Instrumentation Engineers (SPIE) Conference Series, Vol. 7735, Society of Photo-Optical Instrumentation Engineers (SPIE) Conference Series

McLean, I. S., Steidel, C. C., Epps, H. W., Konidaris, N., Matthews, K. Y., Adkins, S., Aliado, T., Brims, G., Canfield, J. M., Cromer, J. L., Fucik, J., Kulas, K., Mace, G., Magnone, K., Rodriguez, H., Rudie, G., Trainor, R., Wang, E., Weber, B., & Weiss, J. 2012, in Society of Photo-Optical Instrumentation Engineers (SPIE) Conference Series, Vol. 8446, Society of Photo-Optical Instrumentation Engineers (SPIE) Conference Series

McLinden, E. M., Finkelstein, S. L., Rhoads, J. E., Malhotra, S., Hibon, P., Richardson, M. L. A., Cresci, G., Quirrenbach, A., Pasquali, A., Bian, F., Fan, X., & Woodward, C. E. 2011, ApJ, 730, 136

Merloni, A., Bongiorno, A., Bolzonella, M., Brusa, M., Civano, F., Comastri, A., Elvis, M., Fiore, F., Gilli, R., Hao, H., Jahnke, K., Koekemoer, A. M., Lusso, E., Mainieri, V., Mignoli, M., Miyaji, T., Renzini, A., Salvato, M., Silverman, J., Trump, J., Vignali, C., Zamorani, G., Capak, P., Lilly, S. J., Sanders, D., Taniguchi, Y., Bardelli, S., Carollo, C. M., Caputi, K., Contini, T., Coppa, G., Cucciati, O., de la Torre, S., de Ravel, L., Franzetti, P., Garilli, B., Hasinger, G., Impey, C., Iovino, A., Iwasawa, K., Kampczyk, P., Kneib, J.-P., Knobel, C., Kovač, K., Lamareille, F., Le Borgne, J.-F., Le Brun, V., Le Fèvre, O., Maier, C., Pello, R., Peng, Y., Perez Montero, E., Ricciardelli, E., Scodeggio, M., Tanaka, M., Tasca, L. A. M., Tresse, L., Vergani, D., & Zucca, E. 2010, ApJ, 708, 137

Meusinger, H. & Brunzendorf, J. 2001, A&A, 374, 878

Mostardi, R. E., Shapley, A. E., Nestor, D. B., Steidel, C. C., Reddy, N. A., & Trainor, R. F. 2013, ApJ, 779, 65

Moster, B. P., Somerville, R. S., Maulbetsch, C., van den Bosch, F. C., Macciò, A. V., Naab, T., & Oser, L. 2010, ApJ, 710, 903

Myers, A. D., Brunner, R. J., Nichol, R. C., Richards, G. T., Schneider, D. P., & Bahcall, N. A. 2007, ApJ, 658, 85

Myers, A. D., Brunner, R. J., Richards, G. T., Nichol, R. C., Schneider, D. P., Vanden Berk, D. E., Scranton, R., Gray, A. G., & Brinkmann, J. 2006, ApJ, 638, 622

Nemmen, R. S. & Brotherton, M. S. 2010, MNRAS, 408, 1598

Netzer, H., Lira, P., Trakhtenbrot, B., Shemmer, O., & Cury, I. 2007, ApJ, 671, 1256

Netzer, H. & Trakhtenbrot, B. 2007, ApJ, 654, 754

Oke, J. B. 1990, AJ, 99, 1621

Oke, J. B., Cohen, J. G., Carr, M., Cromer, J., Dingizian, A., Harris, F. H., Labrecque, S., Lucinio, R., Schaal, W., Epps, H., & Miller, J. 1995, PASP, 107, 375

Padmanabhan, N., White, M., Norberg, P., & Porciani, C. 2009, MNRAS, 397, 1862

Panter, B., Jimenez, R., Heavens, A. F., & Charlot, S. 2007, MNRAS, 378, 1550

Partridge, R. B. & Peebles, P. J. E. 1967, ApJ, 147, 868

Peng, C. Y., Impey, C. D., Rix, H.-W., Kochanek, C. S., Keeton, C. R., Falco, E. E., Lehár, J., & McLeod, B. A. 2006, ApJ, 649, 616

Pettini, M., Rix, S. A., Steidel, C. C., Adelberger, K. L., Hunt, M. P., & Shapley, A. E. 2002, ApJ, 569, 742

Pettini, M., Shapley, A. E., Steidel, C. C., Cuby, J.-G., Dickinson, M., Moorwood, A. F. M., Adelberger, K. L., & Giavalisco, M. 2001, ApJ, 554, 981

Pettini, M., Steidel, C. C., Adelberger, K. L., Dickinson, M., & Giavalisco, M. 2000, ApJ, 528, 96

Porciani, C., Magliocchetti, M., & Norberg, P. 2004, MNRAS, 355, 1010

Porciani, C. & Norberg, P. 2006, MNRAS, 371, 1824

Prada, F., Klypin, A. A., Cuesta, A. J., Betancort-Rijo, J. E., & Primack, J. 2011, ArXiv e-prints

Press, W. H. & Schechter, P. 1974, ApJ, 187, 425

Rakic, O., Schaye, J., Steidel, C. C., & Rudie, G. C. 2011, MNRAS, 414, 3265

Reddy, N. A., Steidel, C. C., Pettini, M., Adelberger, K. L., Shapley, A. E., Erb, D. K., & Dickinson, M. 2008, ApJS, 175, 48

Rees, M. J. 1984, ARA&A, 22, 471

Richards, G. T., Vanden Berk, D. E., Reichard, T. A., Hall, P. B., Schneider, D. P., SubbaRao, M., Thakar, A. R., & York, D. G. 2002, AJ, 124, 1

Riebe, K., Partl, A. M., Enke, H., Forero-Romero, J., Gottloeber, S., Klypin, A., Lemson, G., Prada, F., Primack, J. R., Steinmetz, M., & Turchaninov, V. 2011, ArXiv e-prints

Robertson, B. E., Furlanetto, S. R., Schneider, E., Charlot, S., Ellis, R. S., Stark, D. P., McLure, R. J., Dunlop, J. S., Koekemoer, A., Schenker, M. A., Ouchi, M., Ono, Y., Curtis-Lake, E., Rogers, A. B., Bowler, R. A. A., & Cirasuolo, M. 2013, ApJ, 768, 71

Rosdahl, J. & Blaizot, J. 2012, MNRAS, 423, 344

Ross, N. P., Shen, Y., Strauss, M. A., Vanden Berk, D. E., Connolly, A. J., Richards, G. T., Schneider, D. P., Weinberg, D. H., Hall, P. B., Bahcall, N. A., & Brunner, R. J. 2009, ApJ, 697, 1634

Rudie, G. C., Steidel, C. C., Trainor, R. F., Rakic, O., Bogosavljević, M., Pettini, M., Reddy, N., Shapley, A. E., Erb, D. K., & Law, D. R. 2012, ApJ, 750, 67

Salpeter, E. E. 1964, ApJ, 140, 796

Sandage, A. 1965, ApJ, 141, 1560

Sanders, D. B., Soifer, B. T., Elias, J. H., Madore, B. F., Matthews, K., Neugebauer, G., & Scoville, N. Z. 1988, ApJ, 325, 74

Schaerer, D. 2002, A&A, 382, 28

Schechter, P. 1976, ApJ, 203, 297

Schenker, M. A., Ellis, R. S., Konidaris, N. P., & Stark, D. P. 2013, ApJ, 777, 67

Schmidt, M. 1959, ApJ, 129, 243

—. 1963, Nature, 197, 1040

—. 1965, ApJ, 141, 1295

Seljak, U. 2000, MNRAS, 318, 203

—. 2002, MNRAS, 334, 797

Shapley, A. E., Steidel, C. C., Pettini, M., & Adelberger, K. L. 2003, ApJ, 588, 65

Shen, Y., Hennawi, J. F., Shankar, F., Myers, A. D., Strauss, M. A., Djorgovski, S. G., Fan, X., Giocoli, C., Mahabal, A., Schneider, D. P., & Weinberg, D. H. 2010, ApJ, 719, 1693

Shen, Y., Strauss, M. A., Oguri, M., Hennawi, J. F., Fan, X., Richards, G. T., Hall, P. B., Gunn, J. E., Schneider, D. P., Szalay, A. S., Thakar, A. R., Vanden Berk, D. E., Anderson, S. F., Bahcall, N. A., Connolly, A. J., & Knapp, G. R. 2007, AJ, 133, 2222

Shibuya, T., Ouchi, M., Nakajima, K., Hashimoto, T., Ono, Y., Rauch, M., Gauthier, J.-R., Shimasaku, K., Goto, R., Mori, M., & Umemura., M. 2014, ApJ, 788, 74

Shields, G. A. 1999, PASP, 111, 661

Springel, V., White, S. D. M., Jenkins, A., Frenk, C. S., Yoshida, N., Gao, L., Navarro, J., Thacker, R., Croton, D., Helly, J., Peacock, J. A., Cole, S., Thomas, P., Couchman, H., Evrard, A., Colberg, J., & Pearce, F. 2005, Nature, 435, 629

Stark, D. P., Ellis, R. S., & Ouchi, M. 2011, ApJ, 728, L2

Steidel, C. C., Adelberger, K. L., Shapley, A. E., Erb, D. K., Reddy, N. A., & Pettini, M. 2005, ApJ, 626, 44

Steidel, C. C., Adelberger, K. L., Shapley, A. E., Pettini, M., Dickinson, M., & Giavalisco, M. 2000, ApJ, 532, 170

—. 2003, ApJ, 592, 728

Steidel, C. C., Bogosavljević, M., Shapley, A. E., Kollmeier, J. A., Reddy, N. A., Erb, D. K., & Pettini, M. 2011, ApJ, 736, 160

Steidel, C. C., Erb, D. K., Shapley, A. E., Pettini, M., Reddy, N., Bogosavljević, M., Rudie, G. C., & Rakic, O. 2010, ApJ, 717, 289

Steidel, C. C., Giavalisco, M., Pettini, M., Dickinson, M., & Adelberger, K. L. 1996, ApJ, 462, L17

Steidel, C. C., Rudie, G. C., Strom, A. L., Pettini, M., Reddy, N. A., Shapley, A. E., Trainor, R. F., Erb, D. K., Turner, M. L., Konidaris, N. P., Kulas, K. R., Mace, G., Matthews, K., & McLean, I. S. 2014, ArXiv e-prints

Steidel, C. C., Shapley, A. E., Pettini, M., Adelberger, K. L., Erb, D. K., Reddy, N. A., & Hunt, M. P. 2004, ApJ, 604, 534

Surdej, J., Magain, P., Swings, J.-P., Borgeest, U., Courvoisier, T. J.-L., Kayser, R., Kellermann, K. I., Kuhr, H., & Refsdal, S. 1987, Nature, 329, 695

Trainor, R. & Steidel, C. C. 2013, ApJ, 775, L3

Trainor, R. F. & Steidel, C. C. 2012, ApJ, 752, 39

van de Voort, F., Schaye, J., Booth, C. M., Haas, M. R., & Dalla Vecchia, C. 2011, MNRAS, 414, 2458

Venemans, B. P., Röttgering, H. J. A., Miley, G. K., van Breugel, W. J. M., de Breuck, C., Kurk, J. D., Pentericci, L., Stanford, S. A., Overzier, R. A., Croft, S., & Ford, H. 2007, A&A, 461, 823

Verhamme, A., Dubois, Y., Blaizot, J., Garel, T., Bacon, R., Devriendt, J., Guiderdoni, B., & Slyz, A. 2012, A&A, 546, A111

Verhamme, A., Schaerer, D., & Maselli, A. 2006, A&A, 460, 397

Wolfe, A. M., Lanzetta, K. M., Turnshek, D. A., & Oke, J. B. 1992, ApJ, 385, 151

Worseck, G., Fechner, C., Wisotzki, L., & Dall'Aglio, A. 2007, A&A, 473, 805

Wright, E. L., Eisenhardt, P. R. M., Mainzer, A. K., Ressler, M. E., Cutri, R. M., Jarrett, T., Kirkpatrick, J. D., Padgett, D., McMillan, R. S., Skrutskie, M., Stanford, S. A., Cohen, M., Walker, R. G., Mather, J. C., Leisawitz, D., Gautier, III, T. N., McLean, I., Benford, D., Lonsdale, C. J., Blain, A., Mendez, B., Irace, W. R., Duval, V., Liu, F., Royer, D., Heinrichsen, I., Howard, J., Shannon, M., Kendall, M., Walsh, A. L., Larsen, M., Cardon, J. G., Schick, S., Schwalm, M., Abid, M., Fabinsky, B., Naes, L., & Tsai, C.-W. 2010, AJ, 140, 1868

York, D. G., Adelman, J., Anderson, Jr., J. E., Anderson, S. F., Annis, J., Bahcall, N. A., Bakken, J. A., Barkhouser, R., Bastian, S., Berman, E., Boroski, W. N., Bracker, S., Briegel, C., Briggs, J. W., Brinkmann, J., Brunner, R., Burles, S., Carey, L., Carr, M. A., Castander, F. J., Chen, B., Colestock, P. L., Connolly, A. J., Crocker, J. H., Csabai, I., Czarapata, P. C., Davis, J. E., Doi, M., Dombeck, T., Eisenstein, D., Ellman, N., Elms, B. R., Evans, M. L., Fan, X., Federwitz, G. R., Fiscelli, L., Friedman, S., Frieman, J. A., Fukugita, M., Gillespie, B., Gunn, J. E., Gurbani, V. K., de Haas, E., Haldeman, M., Harris, F. H., Hayes, J., Heckman, T. M., Hennessy, G. S., Hindsley, R. B., Holm, S., Holmgren, D. J., Huang, C.-h., Hull, C., Husby, D., Ichikawa, S.-I., Ichikawa, T., Ivezić, Ž., Kent, S., Kim, R. S. J., Kinney, E., Klaene, M., Kleinman, A. N., Kleinman, S., Knapp, G. R., Korienek, J., Kron, R. G., Kunszt, P. Z., Lamb, D. Q., Lee, B., Leger, R. F., Limmongkol, S., Lindenmeyer, C., Long, D. C., Loomis, C., Loveday, J., Lucinio, R., Lupton, R. H., MacKinnon, B., Mannery, E. J., Mantsch, P. M., Margon, B., McGehee, P., McKay, T. A., Meiksin, A., Merelli, A., Monet, D. G., Munn, J. A., Narayanan, V. K., Nash, T., Neilsen, E., Neswold, R., Newberg, H. J., Nichol, R. C., Nicinski, T., Nonino, M., Okada, N., Okamura, S., Ostriker, J. P., Owen, R., Pauls, A. G., Peoples, J., Peterson, R. L., Petravick, D., Pier, J. R., Pope, A., Pordes, R., Prosapio, A., Rechenmacher, R., Quinn, T. R., Richards, G. T., Richmond, M. W., Rivetta, C. H., Rockosi, C. M., Ruthmansdorfer, K., Sandford, D., Schlegel, D. J., Schneider, D. P., Sekiguchi, M., Sergey, G., Shimasaku, K., Siegmund, W. A., Smee, S., Smith, J. A., Snedden, S., Stone, R., Stoughton, C., Strauss, M. A., Stubbs, C., SubbaRao, M., Szalay, A. S., Szapudi, I., Szokoly, G. P., Thakar, A. R., Tremonti, C., Tucker, D. L., Uomoto, A., Vanden Berk, D., Vogeley, M. S., Waddell, P., Wang, S.-i., Watanabe, M., Weinberg, D. H., Yanny, B., & Yasuda, N. 2000, AJ, 120, 1579

Zehavi, I., Weinberg, D. H., Zheng, Z., Berlind, A. A., Frieman, J. A., Scoccimarro, R., Sheth, R. K., Blanton, M. R., Tegmark, M., Mo, H. J., Bahcall, N. A., Brinkmann, J., Burles, S., Csabai, I., Fukugita, M., Gunn, J. E., Lamb, D. Q., Loveday, J., Lupton, R. H., Meiksin, A., Munn, J. A., Nichol, R. C., Schlegel, D., Schneider, D. P., SubbaRao, M., Szalay, A. S., Uomoto, A., & York, D. G. 2004, ApJ, 608, 16

Zehavi, I., Zheng, Z., Weinberg, D. H., Blanton, M. R., Bahcall, N. A., Berlind, A. A., Brinkmann, J., Frieman, J. A., Gunn, J. E., Lupton, R. H., Nichol, R. C., Percival, W. J., Schneider, D. P., Skibba, R. A., Strauss, M. A., Tegmark, M., & York, D. G. 2011, ApJ, 736, 59

Zheng, Z. & Wallace, J. 2013, ArXiv e-prints